NON-OXIDATIVE DEHYDROGENATION OF PROPANE TO PROPENE OVER PRECIOUS-METAL FREE ANATASE TITANIA

A THESIS SUBMITTED TO
THE GRADUATE SCHOOL OF NATURAL AND APPLIED SCIENCES
OF
MIDDLE EAST TECHNICAL UNIVERSITY

BY

IQTIDAR ALI KHAN

IN PARTIAL FULFILLMENT OF THE REQUIREMENTS
FOR
THE DEGREE OF MASTER OF SCIENCE
IN
CHEMICAL ENGINEERING

AUGUST 2022

Approval of the thesis:

NON-OXIDATIVE DEHYDROGENATION OF PROPANE TO PROPENE OVER PRECIOUS METAL-FREE ANATASE TITANIA

submitted by **IQTIDAR ALI KHAN** in partial fulfillment of the requirements for the degree of **Master of Science** i**n Chemical Engineering, Middle East Technical University** by,

Prof. Dr. Halil Kalıpçılar
Dean, Graduate School of **Natural and Applied Sciences** _____

Prof. Dr. Pınar Çalık
Head of the Department, **Chemical Engineering** _____

Assist. Prof. Dr. Gökhan Çelik
Supervisor, **Chemical Engineering, METU** _____

Examining Committee Members:

Prof. Dr. Gürkan Karakaş
Chemical Engineering, METU _____

Assist. Prof. Dr. Gökhan Çelik
Chemical Engineering, METU _____

Prof. Dr. Naime Aslı Sezgi
Chemical Engineering, METU _____

Assoc. Prof. Dr. Bahar İpek Torun
Chemical Engineering, METU _____

Assoc. Prof. Dr. Hüseyin Arbağ
Chemical Engineering, Gazi University _____

Date: 23.08.2022

I hereby declare that all information in this document has been obtained and presented in accordance with academic rules and ethical conduct. I also declare that, as required by these rules and conduct, I have fully cited and referenced all material and results that are not original to this work.

Name Last name : Iqtidar Ali Khan

Signature :

ABSTRACT

NON-OXIDATIVE DEHYDROGENATION OF PROPANE TO PROPENE OVER PRECIOUS METAL-FREE ANATASE TITANIA

Khan, Iqtidar Ali
Master of Science, Chemical Engineering
Supervisor: Assist. Prof. Dr. Gökhan Çelik

August 2022, 139 pages

Propylene is a versatile compound in the petrochemical industry. Albeit, it is merely used as a final product, propylene serves as a building block for the production of a wide variety of chemicals such as polypropylene, cumene, isopropanol, propylene oxide, and acetone, to name a few. Conventionally, propylene is produced as a by-product during fluid catalytic cracking (FCC) and steam cracking (SC) of oil fractions. However, the supply-demand gap of propene produced from these processes and their economic/environmental limitations have led to alternative greener propene production routes such as non-oxidative propane dehydrogenation (PDH). The PDH technology has been commercialized and applied on a wide scale where alumina-supported chromia or platinum catalysts are used. However, the toxicity of chromia and the high cost of platinum has surged interest in the use of low-cost and environmentally benign catalysts. Bulk metal oxides such as zirconia, titania, and alumina are the quintessence of such materials and have shown promising results for non-oxidative propane dehydrogenation. Over these materials, coordinatively unsaturated cations located near oxygen vacancies(defects) are demonstrated to be the active sites for C-H activation. With the aforementioned fact, we aimed to synthesize non-toxic, non-noble, and dopant-free titania for non-

oxidative propane dehydrogenation. Synthesized catalysts were characterized by Nitrogen physisorption, Raman spectroscopy, Thermal Gravimetric Analysis(TGA), Temperature programmed reduction (TPR), X-ray diffraction, UV-visible spectroscopy, X-ray Photoelectron spectroscopy(XPS) and in-situ pyridine DRIFT. In our study, we have demonstrated that the oxygen vacancies(defects) and surface properties of titania can be tuned during the in-situ synthesis of titania by varying the volume (0,2,6,8 and 10mL) of 1M HCl. The propane conversion and the yield of propene showed the volcano-shaped curve with respect to the volume of HCl added during the sol-gel synthesis of titania. Titania synthesized with 6mL addition of HCl showed the best catalytic performance in comparison with other synthesized titania samples. Over 99% selectivity was achieved for our best-performing catalyst tested in a differential regime. Our best-performing catalyst also revealed industrial relevance by showing a high initial propane conversion(~25%) with high propene selectivity(~96%).

Keywords: Propane dehydrogenation, Propene, Titanium dioxide, Oxygen vacancies, Coordinatively unsaturated Ti cations

ÖZ

DEĞERLİ METAL İÇERMEYEN ANATAZ TİTANYA ÜZERİNDE PROPANIN PROPENE OKSİDATİF OLMAYAN DEHİDROJENASYONU

Khan, Iqtidar Ali
Yüksek Lisans, Kimya Mühendisliği
Tez Yöneticisi: Öğr. Üyesi Dr. Gökhan Çelik

Ağustos 2022, 139 sayfa

Propilen petrokimya endüstrisinde kullanılan çok amaçlı bir bileşiktir. Her ne kadar propilen sadece nihai ürün olarak kullanılsa da polipropilen, kümen, izopropanol, propilen oksit ve aseton gibi çok çeşitli kimyasalların üretimi için bir yapı taşı görevi görür. Geleneksel olarak, propilen, yağ fraksiyonlarının akışkan katalitik parçalama (FCC) ve buharla parçalama (SC) esnasında bir yan ürün olarak üretilir. Ancak, bu proseslerden üretilen propenin arz-talep açığı ve bunların ekonomik/çevresel sınırlamaları, oksidatif olmayan propan dehidrojenasyonu (PDH) gibi alternatif daha yeşil propen üretim yollarına yol açmıştır. PDH teknolojisi ticarileştirildi ve alümina destekli krom veya platin katalizörlerin kullanıldığı geniş bir ölçekte uygulandı. Bununla birlikte, kromyanın toksisitesi ve platinin yüksek maliyeti, düşük maliyetli ve çevreye zarar vermeyen katalizörlerin kullanımına yönelik ilgiyi artırmıştır. Zirkonya, titanya ve alümina gibi dökme metal oksitler, bu tür malzemelerin özüdür ve oksidatif olmayan propan dehidrojenasyonu için umut verici sonuçlar göstermiştir. Bu materyaller üzerinde, oksijen boşluklarının yakınında bulunan koordineli olarak doymamış katyonların, C-H aktivasyonu için aktif alanlar olduğu gösterilmiştir. Bahsi geçen durum ile, oksidatif olmayan propan dehidrojenasyonu için toksik olmayan, asil olmayan ve katkı maddesi içermeyen titanya sentezlemeyi

amaçladık. Sentezlenen katalizörler Nitrojen fizisorpsiyonu, Raman spektroskopisi, Termogravimetrik Analiz (TGA), Sıcaklık programlı indirgeme (TPR), X-ışını kırınımı, UV-görünür spektroskopisi, X-ışını Fotoelektron spektroskopisi (XPS) ve in-situ piridin DRIFT ile karakterize edildi. Çalışmamızda, 1M HCl'nin hacmini (0,2,6,8 ve 10mL) değiştirerek titanyanın in-situ sentezi sırasında oksijen boşluklarının ve yüzey özelliklerinin ayarlanabileceğini gösterdik. Propan dönüşümü ve propen verimi, titanyanın sol-jel sentezi sırasında eklenen HCl'nin hacmine göre volkan şekilli eğriyi göstermiştir. 6 mL HCl ilavesi ile sentezlenen titanya, diğer sentezlenen titanya örneklerine kıyasla en iyi katalitik performansı göstermiştir. Diferansiyel rejimde test edilen en iyi performans gösteren katalizörümüz için %99'un üzerinde seçicilik elde edildi. En iyi performans gösteren katalizörümüz, yüksek propen seçiciliği (~%96) ile yüksek bir ilk propan dönüşümü (~%25) göstererek endüstriyel uygunluk düzeyini de ortaya koydu.

Anahtar Kelimeler: Propan dehidrojenasyonu, Propen, Titanyum dioksit, Oksijen boşlukları, Koordinatlı doymamış Ti katyonları

To my precious family,

ACKNOWLEDGMENTS

I would like to express my immense veneration to my supervisor Assist. Prof. Dr. Gökhan Çelik for guiding and supporting me throughout my graduate studies. I admire his benevolent personality and his fastidious and stupendous attitude towards research also motivated me to develop conscientious behavior in conducting research. He has always welcomed walk-in to his office whenever I experienced any bewilderment during my studies.

I would also like to express reverence to my jury members, Prof. Dr. Gürkan Karakaş, Prof. Dr. Naime Aslı Sezgi, Assoc. Prof. Dr. Bahar İpek Torun and Assoc. Prof. Dr. Hüseyin Arbağ for examining my thesis and providing their valuable feedbacks.

I extend my sincere appreciation to all faculty members of the METU Department of Chemical Engineering for enlightening me with their chemical engineering knowledge. My gratitude extends further to Prof. Dr. Deniz Üner for supporting me during my initial stages of graduate studies. Not only her deep scientific knowledge but also her wisdom and perspective about life have always inspired me to think out of the box.

I am very grateful to the scientific and technological research council of Türkiye (TUBITAK) for financially supporting this study with the 118C260 project.

I express my sincere thanks to all the the administrative and technical staff of METU Department of Chemical Engineering including Kemal Yıldırım, Mihrican Açıkgöz, Cemil Araçlı, İsa Çağlar, Ramazan Küçükdanışman, Mahmut Akdağ and Sedat Taşbaşı. I offer my heartfelt thanks to Doğan Akkuş for not only carrying out N_2 physisorption experiments but always showing immense hospitality.

I sincerely thank all the research assistants of the METU Department of Chemical Engineering especially Merve Sarıyer and Öznur Kavak for making a pleasant environment in the department.

I warmly thank the postdoctoral researchers of our lab, Dr. Asmae Bouziani and Dr. Ece Hamdiye for their guidance throughout my graduate studies. I also express gratitude to my lab mates Enes Akyıldız, Candan Karaeyvaz, Almira Çaldıklıoğlu, Uğur Sökmen, Cansu Erdil and İrem Özen for their freindship and offering a joyful experience during my studies. My sincere thanks to Candan Karaeyvaz for SEM/EDX analysis. I am really grateful to my brother Enes Akyıldız for his help whenever I needed it. I offer my heartfelt appreciation to Selin Karahan, Arzum Ceren Aydoğdu and Almira Çaldıklıoğlu for their valuable friendship. Special tea by Selin and Arzum's saccharine attitude was more than what I always needed to kick-start my day in the lab. I further extend my gratitude to Arzum Ceren Aydoğdu for translating the abstract of this thesis into Turkish. I am forever indebted to Almira Çaldıklıoğlu for her endless support and frequently bestowing me with her mom's (Neslihan Çaldıklıoğlu) delicacy.

I would also like to thank Beste Avcı for always making spontaneous plans. I learned a lot from our deep philosophical conversations. During my graduate studies, I have never met anyone as diligent as her and I admire her heretical and perplexing perspective towards life.

I am also grateful to the visiting faculty Dr. Balal Yousaf and Dr. Khurram Shehzad, Marie Sklodowska-Curie postdoctoral researcher Dr. Yaqoob Khan, Ph.D. scholars Zubair Rahim and Ahmed Javed for always making me feel at home and supporting me whenever I needed their help. I can never forget the supreme delicacy of Dr. Balal during our endless card games.

I am extremely delighted to thank all my friends including Abdullah Athar, Shahzaib Abid, Asif Saeed, Ansab Alvi, Zoya Nayyer, Ilsa Aleem, Maryam Ghias, Nofal Siddiqui, Daniyal Shoukat, Bilal Rizwan, Hamza Arif, Daniyal Basharat, Haşim Kuran, Atakan Ayuz, Gizem Avcı, Beril Üstünkaya, Aziz Mohammed, Cezar Agha, Rameez ul Haq, Areeba Khan, Zikrullah Bölükkaya, Zaid Hafeez, Salman Mustafa Husain, Maria Asif, Amen Chugtai, Abdul Ahad Khan, Ammar Ashraf, Ali Ahmed,

Sifatullah, Ahmed Gulzar, Mohammed Mufleh, Ali Akman, Cem Aktekin, Ekin Murt, Samet Kocaman and Faizan Malik who always believed in me and always brought a positive change to my personality and vision.

I owe special thanks to Middle East Technical University (METU) for providing me with an opportunity to study here. Coming to Türkiye at the age of 20, I have spent the best 7 years of my life. I feel extremely blessed to have exposure to the deep Turkish traditions which not every international gets a chance to experience. All the ups and downs I have experienced here, helped me to develop an independent personality with a resilient character. Wherever I go in the future, part of my soul will always be in Türkiye.

Finally, I would like to express my deepest appreciation to my grandparents(late), parents, and all my cousins for their unconditional love, support, and honest prayers for me. My deepest thanks to my sister, Mahrukh Khan, and my brother, Hammad Ali Khan for making my childhood memorable and providing emotional support during my graduate studies. Words are not enough to express my gratitude to my parents, Zulfiqar Ali Khan and Malahat Zulfiqar who always encouraged me to gain a better quality education. I wish all my family would have been here to witness my accomplishment. My parents tried their best to hide their sacrifices from us during our childhood but I was smart enough to discern that numerous times they skipped their meals and lived a very simple life in order to provide me and my siblings with a better quality of life. My dearest mom, I did not know that fulfilling the promises I made with you in my early childhood would take decades. But I assure you that our zenith is very near and every dot would be connected...

TABLE OF CONTENTS

LIST OF TABLES

TABLES

LIST OF FIGURES

FIGURES

LIST OF ABBREVIATIONS

BET	Brunauer-Emmett-Teller
BJH	Barrett-Joyner-Halenda
DRIFTS	Diffuse Reflectance Infrared Fourier Transform Spectroscopy
DRS	Diffused Reflectance Spectroscopy
DTA	Differential Thermal Analysis
EDX	Energy Dispersive X-ray
FCC	Fluid Catalytic Cracking
FID	Flame Ionization Detector
FTIR	Fourier Transform Infrared Spectroscopy
FWHM	Full Width at Half Maximum
GC	Gas Chromatograph
IUPAC	International Union of Pure and Applied Chemistry
MTO	Methanol to Olefin
OCT	Olefin Conversion Technology
PDH	Propane DeHydrogenation
SC	Steam Cracking
SEM	Scanning Electron Microscopy
TCD	Thermal Conductivity Detector
TGA	Thermogravimetric Analysis
TPR	Temperature Programmed Reduction
TPSR	Temperature Programmed Surface Reaction
WHSV	Weight Hourly Space Velocity
XPS	X-ray Photoelectron Spectroscopy
XRD	X-Ray Diffraction

CHAPTER 1

INTRODUCTION

In this chapter, the importance of propene in the petrochemical industry is briefly highlighted followed by its conventional production routes. Then, the objectives of this study are presented.

1.1 Propene as a feed stock

Belonging to the alkene class of hydrocarbons, propylene is a versatile compound in the petrochemical industry. Albeit it is merely used as a final product, propylene serves as a building block for the production of a wide variety of chemicals.

Polypropylene constitutes a major fraction of propylene outlets. Owing to its flexibility, heat resistance, and recyclability, polypropylene is used in the production of packaging materials, drainage pipes, luggage, car bodies, kitchen appliances and not to mention, and the much-needed surgical masks in COVID-19 outbreak[1]. Propylene oxide is another major derivative of propylene which serves mainly as a raw material for the production of propylene glycols and polyurethanes. Due to its chemical inertness, propylene glycol is best used as a solvent in the pharmaceutical and cosmetics industry, as a preservative in the food industry, and anti-freezing agent in the automotive industry. Polyurethanes on the other hand hold their importance in the foam and insulation industry due to their resilience and lightweight. They are used as a foam material for mattresses, sports shoes, automotive seats, and insulation material for buildings and refrigerators, to name a few. Cumene is yet another important derivative of propene which is used mainly for the production of phenol and acetone. Phenol has a diverse array of applications. It is used as a raw material for the production of Bisphenol A and due to its good thermal stability and

adhesiveness, it is best used in the manufacturing of nylon, epoxy-based furniture, and polycarbonate plastics. Due to its antiseptic properties, phenol is used in the production of anesthetics, mouthwashes, and topical medicines. In addition to medicinal products, phenol is also used to produce detergents[2]. In fact, during the COVID-19 outbreak, phenolic detergents served as an affordable option for the mass population to curb the spread of coronavirus[3]. Acetone, on the other hand, is an essential solvent and finds its use mainly in the cosmetics and paints industry where it is used to remove nail polishes and thinning paints respectively[4]. Similarly, acrylic acid and isopropanol are other essential derivatives of propene holding their importance in the plastics and cosmetics industry respectively.

1.2 Propene production routes

As seen in section 1.1, propene undoubtedly holds immense importance in a diverse array of chemical products. As of 2019, the annual worldwide production capacity of propylene reached a total of approximately 130 million metric tons, making it the second most organic chemical produced across the globe after ethylene[5].

Propene can be produced from three different energy sources, viz, oil, coal, and natural gas.

As seen in Figure 1.1, the majority of propylene is produced as a byproduct during fluid catalytic cracking (FCC) and steam cracking (SC) of oil fractions.

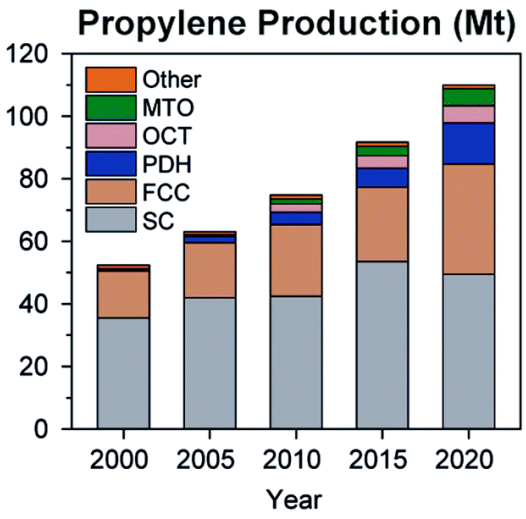

Figure 1.1. Propylene production by different technologies (MTO: Methanol to Olefins, OCT: Olefin Conversion Technology, PDH: Propane DeHydrogenation, FCC: Fluid Catalytic Cracking, SC: Steam Cracking) [6]

Steam cracking is a well-known industrial process for the production of light olefins. In a typical SC process, feed consisting of light alkane or naphtha is mixed with steam and held in a reactor for a very short residence time at a temperature around

800°C. Thereafter, the reaction is quenched and the products are separated[7]. Currently, steam cracking produces approximately 50% of the total propene produced[8]. However, producing propene from the SC process has several shortcomings. The yield of propene from SC is very low (up to 5-20%), thus making it an economically unfeasible process for propene production. This process is also environmentally unfavorable. Steam cracking is a highly endothermic process and is usually carried out at a high temperature, this high energy input requirement is typically fulfilled by burning a large amount of fossil fuels leading to the exorbitant amount of carbon dioxide emissions[9].

Fluid catalytic cracking (FCC) is yet another important technology for the production of light olefins. Put simply, in the FCC process higher fractions of crude oil are converted into gasoline and other high-market value products with the application of a catalyst. In FCC, the catalyst bed is fluidized and the feed is made in contact with the bed, yielding cracking products which are separated in fractionating column[10]. FCC also has several shortcomings in the production of propene. Since the FCC process was originally developed for the production of gasoline, propene is merely formed as a byproduct[8]. Thus, it is difficult to control the already low selectivity to propene, making the FCC process economically unfeasible for propene production. Nevertheless, it is not the selectivity per se that makes the production of propene from FCC unfeasible, but this process is responsible for high carbon dioxide emissions. Even though the energy input required for FCC is significantly lower than that of SC, the regeneration step in FCC contributes to nearly one-fourth of the carbon dioxide emission from refineries [11]

Propylene can also be produced by utilizing coal and natural gas sources. Technologies based on these feedstocks can be further divided into direct and indirect routes.

For the indirect route, methane present in natural gas could be first converted into syngas ($CO+H_2$) by the steam reforming reaction (Equation 1.1):

$$CH_4 + H_2O \leftrightharpoons CO + 3H_2 \quad \Delta H^{\circ}_{298} = 206.0 kJ/mol \qquad \textbf{1.1}$$

This reforming reaction usually takes place at 815°C over a bed of nickel catalyst inside a tubular reactor[12].

On the other hand, coal could also be utilized to generate syngas via a coal-gasification reaction (Equation 1.2) whereby, coal reacts with steam or carbon dioxide to yield syngas [13].

$$C + H_2O \leftrightharpoons CO + H_2 \quad \Delta H^{\circ}_{298} = +131.46 kJ/mol \qquad \textbf{1.2}$$

The syngas generated from coal-gasification or steam reforming of methane can then be converted to propene via Fischer Tropsch synthesis (FTS). FTS is a mature commercial technology comprising a fixed bed, slurry, or fixed bed reactor. The reaction usually takes place at temperatures over 200°C and 300°C for low-temperature and high-temperature Fischer Tropsch synthesis respectively. Nickel, iron, and cobalt materials are commonly used as catalysts, and the pressure used ranges from 10-40bar. FTS is a well-known technology and has plants across several parts of the world however suffers from low efficiency and selectivity.

Production of syngas from either steam reforming of methane or coal-gasification is a highly endothermic process (Equation **1.1** & **1.2**), requiring high input energy. The heat requirement for syngas generation from coal gasification is compensated by the following combustion reaction in the gasifier resulting in carbon dioxide emissions[13]:

$$C + O_2 \leftrightharpoons CO_2 \quad \Delta H^{\circ}_{298} = -393.98\ kJ/mol \qquad \textbf{1.3}$$

Similarly, the syngas generation from steam reforming of methane also requires high energy input and produces one mole of carbon dioxide for each mole of steam reformed. Thus, generating syngas from the coal gasification and steam reforming process is not environmentally feasible owing to their exorbitant amount of carbon dioxide emissions[14].

Controlling the selectivity towards propene from FTS is not facile as this reaction can yield a variety of hydrocarbons as evident in Equation **1.4** which represents the general reaction for FTS. Here, n and m represents the number of carbon atoms in hydrocarbon and number of hydrogen atoms in hydrocarbon molecule respectively :

$$nCO + \left(n + \frac{m}{2}\right) H_2 \rightarrow C_nH_m + nH_2O \qquad \textbf{1.4}$$

The main product from FTS is 'Syncrude' which contains C_{5+} hydrocarbons in liquid-solid form and C_1-C_4 products are merely formed as byproducts[15]. Thus, synthesizing propene from FTS is economically and environmentally unfeasible, and alternative routes for propene production are better sought.

To overcome the low selectivity to propene via FTS, syngas can be first converted to methanol, and then methanol can be further converted to propene via methanol to olefin (MTO) or methanol to propene (MTP) technologies. MTO is a mature technology commercialized by UOP, DICP, and Sinopec for the synthesis of dimethyl ether (DME) and light olefins from methanol over zeolite catalysts. The unique geometry and microporosity of zeolite materials hinder the diffusion of long chain hydrocarbons and enhanced selectivity of light olefins is achieved[16,17]. Similarly, high selectivity to propene can be achieved from the methanol to propene (MTP) process. This technology was commercialized by Lurgi wherein specifically, zeolite tailored catalysts are utilized to obtain a significant yield of propene[18]. MTO/MTP technologies undoubtedly offer a significant advantage over propene production with high selectivity however the process relies on the availability of methanol. This raw material is conventionally produced from syngas and as discussed earlier in this section, the production of syngas is an economically and environmentally inefficient process.

With the rising concerns of the global greenhouse gas emission from various processes and propene production from FCC/SC and syngas-based routes exacerbating the situation, an alternative and greener way of propene production is sought. Additionally, as evident from Figure 1.2, propene production from conventional routes cannot fulfill the increasing demand for propene and alternative production routes could fill the gap between the supply and demand of propene.

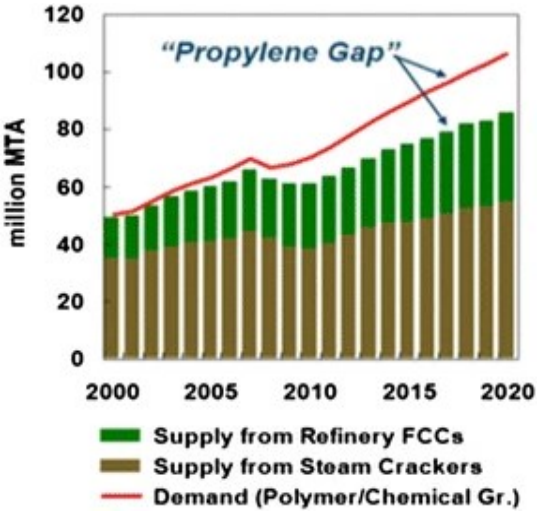

Figure 1.2. Supply and demand of propene[19]

1.3 Aim of the study

As evident from the succinct discussion in the above sections, alternative greener propene production routes are indispensable to impede the reverberating economic and environmental impacts caused by conventional propene production routes.

The on-purpose dehydrogenation of propane present in shale gas can serve as an unorthodox commodity for propene production and at the same time mitigate economic and environmental damage caused by conventional propene production methods

Figure 1.3 discerns that shale gas reserves are ubiquitous across the globe with China and United States as major players[20,21]. Propane is present in considerable amounts in shale gas and can be easily separated to serve as a source of propane for Propane dehydrogenation thus our reliance on waning oil sources could be minimized[22].

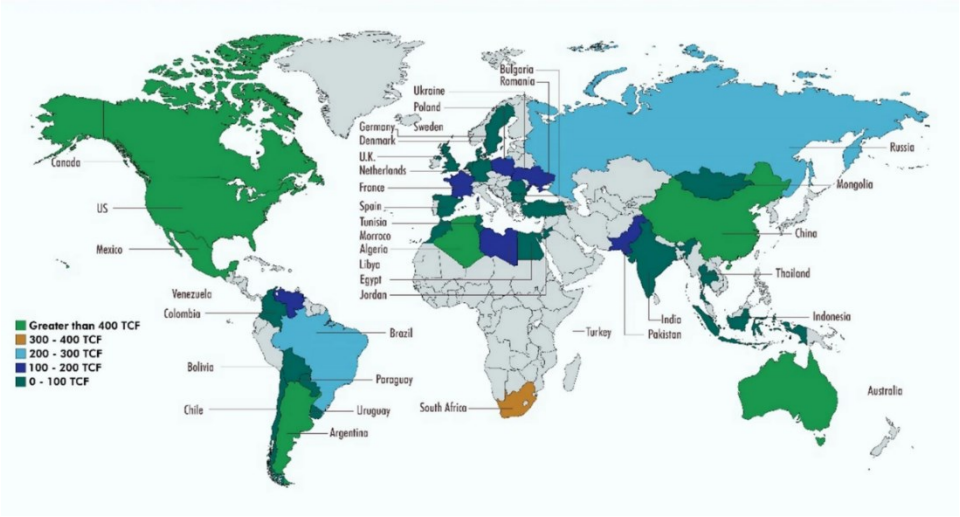

Figure 1.3. Global reserves of shale gas [21]

The following section gives a brief overview of on-purpose propane dehydrogenation technologies and their bottleneck problems. Then, a synopsis of alternatives to commercial catalysts used for propane dehydrogenation in the literature is presented along with their shortcomings. In the light of those problems, synthesizing non-noble and non-toxic catalyst was the aim of this study, and its activity against non-oxidative propane dehydrogenation while supporting the results with multiple characterization techniques are presented.

CHAPTER 2

LITERATURE REVIEW

In this chapter, a brief overview of oxidative propane dehydrogenation is presented while emphasis is given to non-oxidative propane dehydrogenation.

The dehydrogenation of propane can take place via two different routes:

i. Oxidative Dehydrogenation
    a) Oxygen-air assisted dehydrogenation
    b) Carbon dioxide-assisted dehydrogenation
ii. Non-oxidative Dehydrogenation

2.1 Oxidative Propane Dehydrogenation(ODH)

In the oxidative dehydrogenation route, propane can be dehydrogenated with air-oxygen or carbon dioxide as an oxidant.

2.1.1 Air-oxygen-assisted oxidative Propane Dehydrogenation

Oxygen-assisted propane dehydrogenation(O_2-PDH) reaction is represented by Equation **2.1**:

$$C_3H_8 + \frac{1}{2}O_2 \leftrightharpoons C_3H_6 + H_2O \quad \Delta H^{\circ}_{298} = -117.4\ \text{kJ/mol} \qquad \textbf{2.1}$$

As seen in the above equation, oxygen-mediated propane dehydrogenation is an exothermic reaction and is carried out in the temperature range of 400-650°C. Figure

2.1 depicts that this reaction has no thermodynamic limitation as evident from the relatively large equilibrium constant in the reaction temperature range[23].

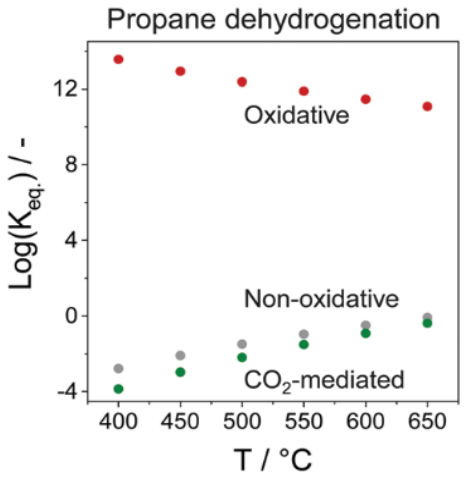

Figure 2.1. Equilibrium constants vs temperature plot for propane dehydrogenation[23]

Despite the minimum heat input requirements and no thermodynamic limitations, oxygen-assisted propane dehydrogenation technology has not been commercialized yet due to its inherent drawbacks. Firstly, the O_2-PDH suffers from low selectivity to propene. Figure 2.2 illustrates the possible reaction products during O_2-assisted propane dehydrogenation. Minor side reactions include cracking of propane to yield methane and ethene. However, a substantial amount of propane is combusted and the dehydrogenation products also undergo overoxidation to carbon dioxide and carbon monoxide. Secondly, the reaction is highly exothermic (Equation **2.1**), thus specialized equipment to extract the excess heat generated is vital for achieving a desirable yield of propene. Thirdly, in the case where the air is used as an oxidant, the separation of nitrogen would add considerable cost to the energy consumption[24].

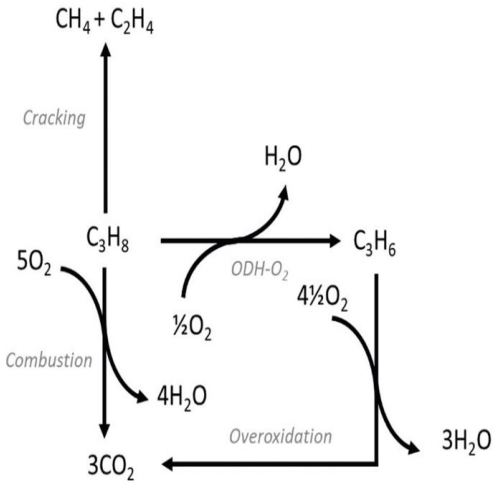

Figure 2.2. O_2-assisted propane dehydrogenation reaction pathway [24]

2.1.2 CO_2-mediated oxidative propane dehydrogenation

Oxidative propane dehydrogenation with carbon dioxide as a mild oxidant is yet another way for on-purpose propene production. Like non-oxidative propane dehydrogenation, CO_2-assisted propane dehydrogenation is thermodynamically limited which is reflected by the very low equilibrium constant in the reaction temperature range (Figure 2.1). Main CO_2 assisted propane dehydrogenation reaction could be represented by the following equation (Equation **2.2**):

$$C_3H_8 + CO_2 \leftrightharpoons C_3H_6 + H_2O + CO \quad \Delta H^{\circ}_{298} = +164\ \text{kJ/mol} \qquad \textbf{2.2}$$

Despite the high endothermicity, this reaction could be carried out at low temperatures (450-600°C) due to the reverse water gas shift (RWGS) reaction (Equation **2.3**). This slightly endothermic reaction shifts the equilibrium of the main reaction (Equation **2.2**) towards high propylene yield by consuming the hydrogen produced during the reaction, yielding carbon monoxide and water[25]. However,

due to the formation of carbon monoxide, CO_2-assisted propane dehydrogenation demands an efficient technology to segregate carbon monoxide[23].

$$H_2 + CO_2 \leftrightharpoons H_2O + CO \quad \Delta H^{\circ}_{298} = +40.6\ \text{kJ/mol} \qquad \textbf{2.3}$$

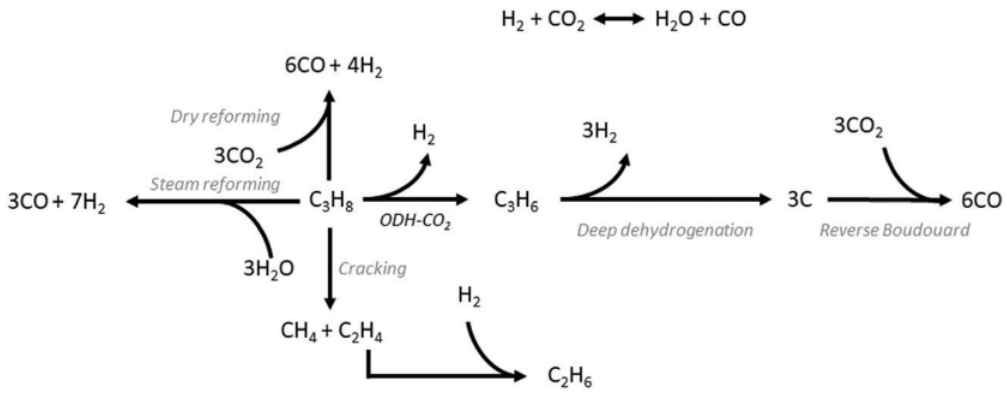

Figure 2.3. CO_2-assisted propane dehydrogenation reaction pathway[24]

CO_2-assisted propane dehydrogenation reaction can follow several reaction pathways as illustrated in Figure 2.3. Dry reforming of propane is a competing side reaction at the reaction conditions. Other undesired reactions include steam reforming of propane and deep dehydrogenation to coke which can further react with carbon dioxide to yield carbon monoxide[24].

Despite the side reactions and the thermodynamic limitation involved in carbon dioxide-assisted propane dehydrogenation reaction, researchers have been trying to develop an optimum catalyst that could inhibit the undesired side reactions and increase the propene yield. The motivation stems from the fact that if this technology is commercialized, the large-scale consumption of carbon dioxide from the environment or other chemical processes will lead to a circular carbon economy and combat global climate change [26–28].

2.2 Non-oxidative propane dehydrogenation(PDH)

Non-oxidative propane dehydrogenation is yet another technology for on-purpose propene production. This reaction is highly endothermic as demonstrated by Equation **2.4**. Also, the non-oxidative propane dehydrogenation reaction is thermodynamically limited as depicted in Figure 2.1 whereby the equilibrium constant is relatively low in the reaction temperature range.

$$C_3H_8 \leftrightharpoons C_3H_6 + H_2 \quad \Delta H^{\circ}_{298} = +125\ \text{kJ/mol} \qquad \textbf{2.4}$$

$$C_3H_8 \leftrightharpoons CH_4 + C_2H_4 \quad \Delta H^{\circ}_{298} = +98.9\ \text{kJ/mol} \qquad \textbf{2.5}$$

$$C_3H_8 \leftrightharpoons 3C + 4H_2 \quad \Delta H^{\circ}_{298} = +119.5\ \text{kJ/mol} \qquad \textbf{2.6}$$

$$C_3H_8 + H_2 \leftrightharpoons C_2H_6 + CH_4 \quad \Delta H^{\circ}_{298} = -37.7\ \text{kJ/mol} \qquad \textbf{2.7}$$

$$C_2H_4 + H_2 \leftrightharpoons C_2H_6 \quad \Delta H^{\circ}_{298} = -136.6\ \text{kJ/mol} \qquad \textbf{2.8}$$

The possible reactions during PDH are given in Equation **2.4**-**2.8** and also illustrated in Figure 2.4. The main reaction is the dehydrogenation of propane with the evolution of hydrogen as a by-product. Thermal/catalytic cracking of propane is a major side reaction whereby propane is converted to methane and ethene. The ethane

formed can be hydrogenated to yield ethane. Propane also undergoes hydrogenolysis during PDH reaction yielding methane and ethane. A crucial aspect of non-oxidative propane dehydrogenation is the coke formation due to deep dehydrogenation.

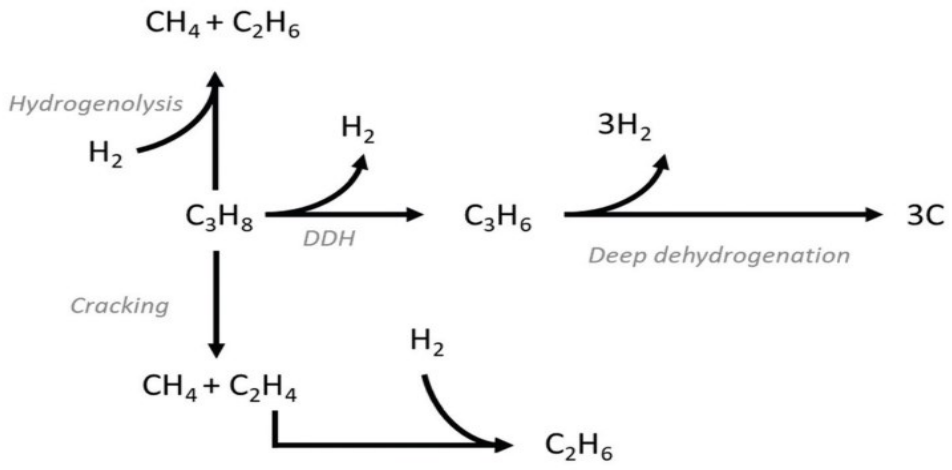

Figure 2.4. Non-oxidative propane dehydrogenation reaction pathway[24]

Non-oxidative propane dehydrogenation reaction (Equation **2.4**) is favored at high temperatures and low partial pressures of propane according to Lechatlier's principle. Figure 2.5a. discerns the aforementioned reasoning with the fact that as the reaction temperature increases, the equilibrium conversion increases at a given pressure. Similarly, at a constant temperature, equilibrium conversion increases as the partial pressure of propane decreases[29]. Figure 2.5b is a plot of free energy vs temperature for non-oxidative propane dehydrogenation and associated side reactions at 1bar. At this pressure, PDH reaction is typically favored at high temperatures (above 550°C) since the Gibbs free energy gets more negative. Under these conditions, the side endothermic reactions of propane cracking (Equation **2.5**) and deep dehydrogenation (Equation **2.6**) are also favored. However, the exothermic reactions, propane hydrogenolysis (Equation **2.7**) and ethene hydrogenation (Equation **2.8**) remain relatively unaffected[29]. Thus, to achieve a better yield of propene via non-oxidative propane dehydrogenation it is of utmost importance to

control the reaction via kinetics. Thus, an appropriate choice of catalyst for PDH is essential which can suppress the side reactions and enhance the propene selectivity.

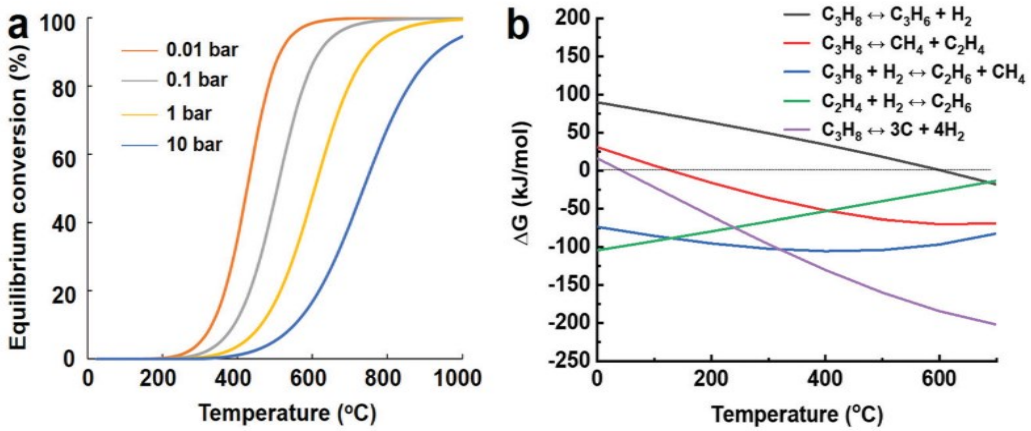

Figure 2.5. Thermodynamic analysis of PDH [29]

2.3 Commercial propane dehydrogenation processes

From the preceding discussion, non-oxidative propane dehydrogenation can serve as a greener alternative for on-purpose propene production. As yet, all the commercial technologies are based on non-oxidative propane dehydrogenation. The following discussion will highlight the operation of propane dehydrogenation commercial technologies and the catalysts involved.

2.3.1 Catofin Process

Catofin was the first technology developed for the dehydrogenation of light alkanes. Apparently, this process was initially used for isobutane dehydrogenation. The isobutene produced from isobutane dehydrogenation was then used for the synthesis of Methyl tertiary butyl ether (MTBE). This chemical was introduced as an anti-knocking agent for gasoline in the 1970s. However, it was banned after a couple of decades since it was causing ground water contamination upon spillage[30]. Thereafter, the use of Catofin technology was then shifted towards propane dehydrogenation. Figure 2.6 shows the schematic of the Catofin process.

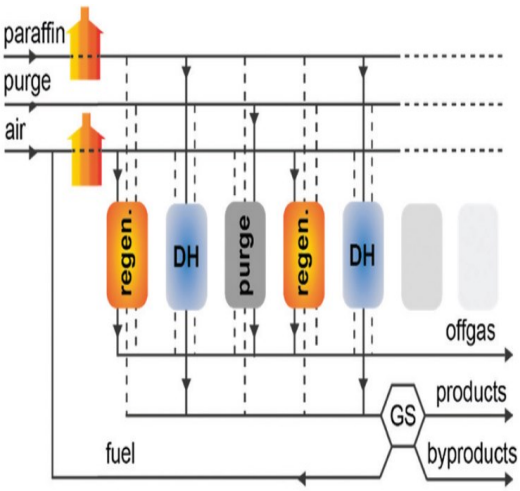

Figure 2.6. Catofin process [6]

Catofin technology operates in cyclic mode, where dehydrogenation (DH), purging, and regeneration(regen.) are carried out in adiabatic-fixed bed reactors. There are typically 5-8 reactors connected in parallel. Each reactor undergoes DH, purge, and regen. cycle with each cycle lasting for about 15-30 minutes. Thus, in this arrangement, a continuous operation is achieved. The reaction is carried out at 575°C and low pressure (0.2-0.5bar). The catalyst used in this process is alumina-supported chromia with alkali promotors. Chromia content is typically 18% which can achieve over 87% selectivity of propene. Very recently (2019) a new formulation (Catofin-311) was devised to obtain even better selectivity and yield of propene, however, the formulation is undisclosed as yet. The high endothermicity (Equation **2.2**) of DH is partly fulfilled by the heat generated from the adjacent reactors which are regenerating the catalyst by burning off the coke. In addition to that, the reaction feed is also preheated before it enters the reactor. Since the reaction acts as a heat sink, inert material is often added to the reactor. The inert material acts as a heat-generating material by undergoing a redox cycle during the reaction, thus ensuring a stable temperature profile of the catalyst bed. On average, the catofin catalyst lasts for almost 3 years. The gradual loss in its activity is compensated by increasing the operating temperature.

2.3.2 Oleflex Process

Oleflex is yet another major technology for propane dehydrogenation. This technology was first commercialized in 1990 in Thailand by Honeywell UOP. Schematic of oleflex process is given in Figure 2.7:

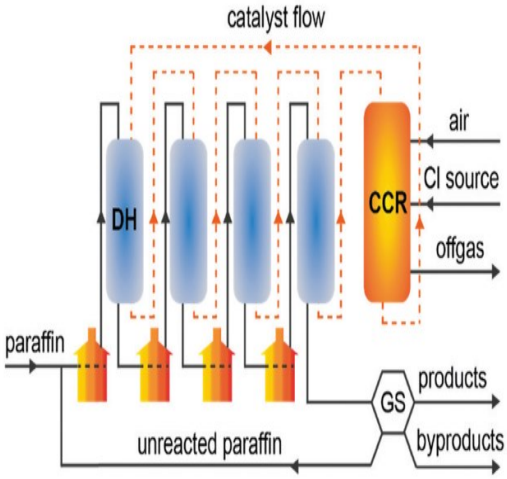

Figure 2.7. Oleflex Process [6]

Oleflex process operates in continuous mode where adiabatic flow reactors are connected in series. The catalyst bed comprises of alumina supported Platinum catalyst with tin as promoter. Dehydrogenation reaction is carried out at 525-705°C and 1-3 bar. The feed is preheated before entering the reactor by preheater. The catalyst bed is fluidized and allowed to flow through the adjacent reactors to the continuous catalyst regeneration unit (CCR). In CCR, the used catalyst is regenerated by burning off the coke deposited on the catalyst using an air-chlorine mixture at ~ 700°C. The heat generated from the highly exothermic regeneration step is utilized to heat the feed. While air oxidizes the coke, chlorine redisperses the platinum particles which are sintered during the reaction. The regenerated catalyst is then fed back to the first reactor and this whole cycle takes 5-10days.

2.3.3 Steam Active Reforming (STAR) process

STAR technology is another technology for propane dehydrogenation. This technology was pioneered by Phillips petroleum in 1992 for the production of isobutene. However, STAR technology was later acquired by ThyssenKrupp Uhde in 1999. Currently, this technology is in operation at three different locations and more licenses are being granted [31]. A schematic of the STAR process is given in Figure 2.8:

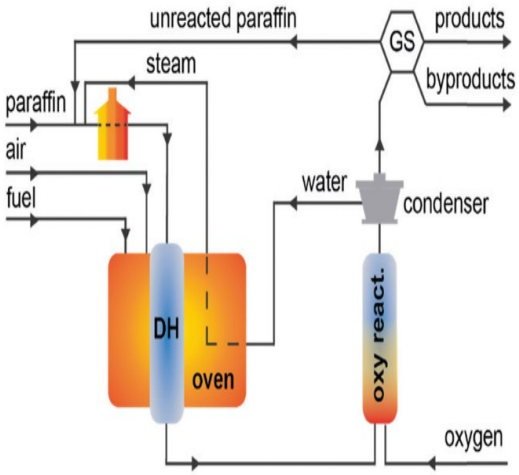

Figure 2.8. STAR/ Linde-BASF process process [6]

STAR technology operates in a cyclic mode where two fixed bed reactors are connected in series. The first reactor is enclosed in an oven which is heated by burning off the fuel gas. This reactor acts as a propane reformer where propane is cofed with steam. Propane dehydrogenation takes place at 500-600°C over a bed of Platinum catalysts supported by calcium and zinc aluminates. Cofed steam assists in burning off any coke deposited on the catalyst; thus, a long operation time(~7hrs) is achieved. Effluent from the first reactor is cooled and then fed with oxygen and steam mixture to the second reactor where hydrogen produced from dehydrogenation is selectively combusted. This shifts the chemical equilibrium towards a higher

conversion of propane. Additionally, the heat generated from the selective combustion of hydrogen is utilized to fulfill the endothermicity of propane dehydrogenation (Equation **2.2**). Thereafter, the products are separated in a gas separation unit (GS).

2.3.4 Fluidized-Bed Dehydrogenation(FBD) process

FBD technology developed by Yarsintez-Snamprogetti is another continuous operation-based technology for alkane dehydrogenation. The aim of this technology was first to produce synthetic rubbers in the 1960s. Later in 1994, this technology was set up in Saudi Arabia for butane dehydrogenation (FBD-4). The same technology can be used for propane dehydrogenation (FBD-3). A schematic of the FBD process is given in Figure 2.9:

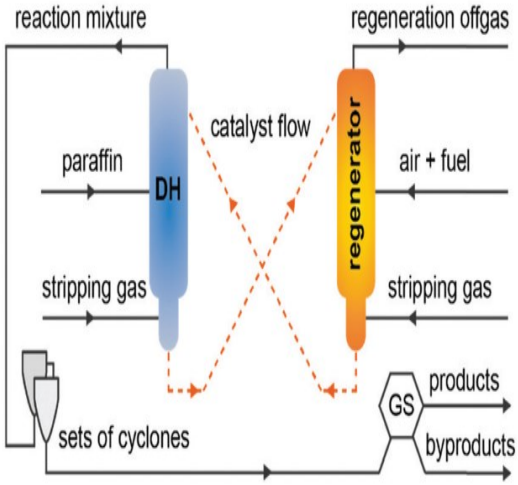

Figure 2.9. FBD Process [6]

The setup comprises dehydrogenation and regeneration reactors. The dehydrogenation reactor is loaded with an alumina-supported chromia catalyst with lower chromium loading than in Catofin technology. The catalyst bed is fluidized using the feed-air mixture. Dehydrogenation reaction takes place at 550-600°C and

1.1-1.5bar. Coke deposition during the dehydrogenation causes the catalyst to deactivate. Thus, the catalyst is transferred to the regeneration unit. In the regenerator, the coke deposited on the catalyst is burnt off at 700°C and the catalyst is regenerated which is later fed back to the dehydrogenation unit. In addition to the heat supplied by burning fuel gas, the heat generated during the regeneration step is utilized for the dehydrogenation reaction. The fluidization offers good heat and mass transfer in the catalyst, however severe attrition shortens the mechanical life of the catalyst. However, the lost catalyst can be compensated by adding a fresh catalyst to the regenerator. Thus, the continuous operation remains uninterrupted.

2.3.5 Linde-BASF process

Similar to STAR technology, the Linde-BASF process is yet another commercial propane dehydrogenation technology developed in 1992. Thus far, this technology has been set up in Germany and Norway. The working principle of this technology is conceptually similar to STAR technology (Figure 2.8). There are three reformer-type reactors in this process. Two of those are used for dehydrogenation reactions. The dehydrogenation reactors are externally heated. Like the STAR process, paraffin feed is mixed with steam, and a dehydrogenation reaction is carried out at 550-650°C over a fixed-bed catalyst. Originally, the catalyst used for the Linde-BASF process was chromia-alumina with Cesium and Zirconium promoters. However, later the catalyst for this technology was changed to hydrotalcite-supported platinum which was claimed to achieve 50% propane conversion and 91% propene selectivity. On the other hand, the third reactor operates under regeneration mode where the deactivated catalyst is regenerated with an air-steam mixture, ensuring a continuous operation.

2.4 Need for alternative catalysts for non-oxidative propane dehydrogenation

From the preceding discussion, non-oxidative propane dehydrogenation presents a promising alternative way of propene production. As yet, all the commercial technologies are based on non-oxidative propane dehydrogenation. The catalysts applied constitutes mainly Chromia or Platinum supported on alumina. However, there are several shortcomings of these materials. Exposure to toxic Cr (VI) species poses several health risks to the workers. Upon inhalation, chromium dust can cause asthma, bronchitis, and nasal ulcer. Some other serious risks upon exposure to hexavalent chromium species include respiratory cancer, DNA damage, and reproductive problems [32–34].

On the other hand, the use of noble platinum is associated with the high upstream cost of propane dehydrogenation. Platinum is a rare metal with a natural abundance of 0.0001% in the earth's crust[35]. Very few countries are privileged to have platinum reserves with South Africa as the major player[36]. The natural minute reserves of platinum and their presence in very few countries make the price of platinum expensive and very volatile[37]. The platinum price skyrocketed in February 2008, when its price reached over 2000 USD per troy ounce due to the electricity shortage in South Africa [38]. With its use in commercial propane dehydrogenation, platinum undergoes agglomeration. To redisperse platinum particles, an air-chlorine mixture is typically used[39]. The use of chlorine gas has its own environmental and health impact. Upon exposure, chlorine can severely irritate the eyes and damage the respiratory system. The high oxidizing ability of chlorine gas makes it very reactive with most of the elements. The formation of chlorinated organic chemicals such as dioxins pollutes marine life which thereafter enters the whole food chain[40–43].

Nevertheless, researchers around the globe have been trying to tailor the Pt-based catalyst by tuning the support and adding promotors to achieve desirable acid/base properties for propane dehydrogenation. Their objective is to come up with a catalyst

with a minimum amount of platinum that can maintain high propylene selectivity with stable catalytic activity[39].

An alternative way to cope with the limitations of commercial propane dehydrogenation catalysts is to utilize non-toxic and non-noble materials. Bulk catalysts such as zirconia, titania, and alumina are the quintessence of such materials and have shown promising results for non-oxidative propane dehydrogenation[23].

2.5 Titania

The discovery of titania dates back to the end of the 18th century when Clergyman and William Gregor discovered the evolution of white metal oxide upon treating menachanite at high temperatures[44]. Titania is a transition metal oxide of titanium. Titanium has a relative atomic mass and an atomic number of 47.88 and 22 respectively. It is the ninth most abundant element in the earth's crust. Due to its strong affinity with oxygen, titanium naturally exists in the oxide form (titania). Owing to its natural abundance, titania is cheaply available. Its characteristics include high chemical and mechanical stability, nontoxicity, UV absorption, and biocompatibility. Due to these properties, titania is used in a wide variety of applications such as dental implants, paint industry, food industry, self-care products, glass coatings, and in particular photocatalysis[45,46].

2.5.1 Properties of titania

Naturally, titania (TiO_2) exists in three phases, viz. anatase, rutile, and brookite phase. The Brookite phase is rare in comparison with the other two phases. In terms of stability, the rutile phase has more stability than anatase and brookite. The later phases transform to rutile upon high-temperature treatment. The schematic of the three phases of titania is given in Figure 2.10 and its chemical properties are tabulated in Table 2.1.

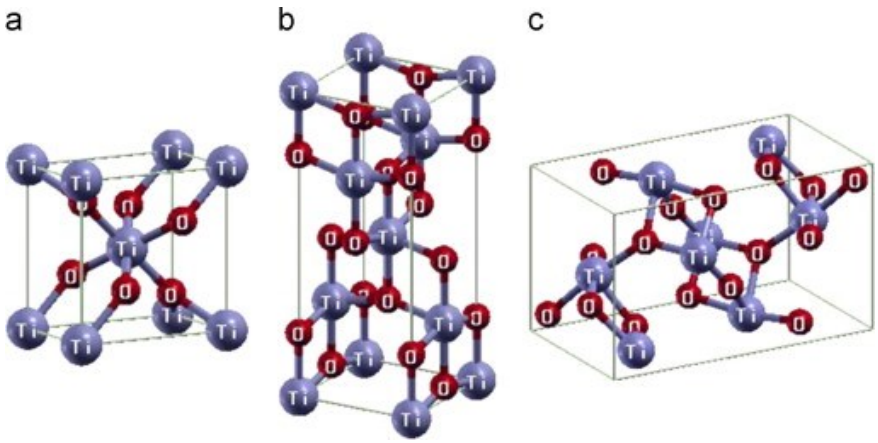

Figure 2.10. TiO_2 crystal phases: (a) Rutile, (b) Anatase and (c) Brookite [47]

Table 2.1 Properties of pure titania phases

	Anatase	**Rutile**	**Brookite**
Structure	Tetragonal	Tetragonal	Orthorhombic
Density(g/cm^3) [48]	3.84	4.26	4.12
Lattice Parameter[49]	a=b=3.79 c=9.44	a=b=4.60 c=2.96	a=9.17 b=5.44 c=5.14
Band gap[50]	3.20(Indirect) 3.53(Direct)	3.01(Indirect) 3.37(Direct)	3.13(Indirect) 3.56(Direct)

It can be seen in Figure 2.10. that all three phases of titania have octahedral geometry. In all phases, one titanium atom is bonded to six oxygen atoms. However, the different bond orientation leads to different crystal structure. The rutile phase exhibits nearly hexagonal close packing with titanium atoms filling half of the octahedron. The edge-sharing of rutile octahedrons results in the formation of linear chains. Anatase and brookite phases have cubic packing. Anatase exhibits a tetragonal crystal structure in which octahedrons are connected through corner sharing. Unlike Rutile, anatase does not exhibit edge sharing. On the other hand, the brookite phase has an orthorhombic structure due to the edge and corner-sharing. A

typical sol-gel synthesis to prepare titania results in the anatase phase, which could be transformed to pure rutile upon high-temperature treatment. A mixture of anatase and rutile phases of titania could be synthesized with low-temperature hydrothermal synthesis[51].

Titania has been widely used in the literature as a photocatalyst. Pure anatase titania has shown better performance for solar cell applications and photocatalytic activity. The rutile phase, on the other hand, exhibits low performance in its photocatalytic application. However, a mixture of these phases is reported to have better performance than the pure phases alone[52].

2.5.2 Oxygen vacancy defects in titania

The physical and chemical properties of titania are greatly influenced by the presence of defects such as line, bulk, interstitial, surface, and point defects. One of the point defects in titania is oxygen vacancy which can exist in bulk and/or surface and is widely utilized in applications such as solar cell, photocatalysis, and propane dehydrogenation. As seen in Figure 2.11, in this type of defect, the oxygen atom which is normally present in the lattice is missing [53]. When lattice oxygen leaves the lattice, it leaves behind the two free electrons which could be identified with electron paramagnetic resonance(EPR) [54]. These vacancies are the active centers in alkane dehydrogenation as discussed in later sections.

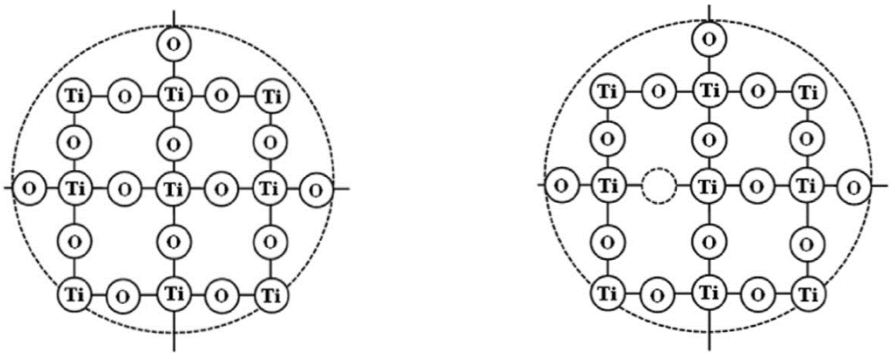

Figure 2.11. TiO_2 with (a) Perfect lattice and (b) Oxygen vacancy

2.5.3 Tailoring oxygen vacancies

As evident from the succinct discussion in the previous section, oxygen vacancies on metal oxides play a crucial role in a wide variety of chemical reactions. The evolution of oxygen vacancies not only changes the local electronic environment but also affects the inherent physicochemical properties. In general, oxygen vacancies could be incorporated by post-treatment reduction or could be induced during in situ synthesis of the titania[55–57]. The following discussion will highlight several possible ways to tune the concentration of oxygen vacancies in metal oxides.

2.5.3.1 Post-treatment in reducing atmosphere

Once the metal oxide is synthesized, oxygen vacancies could be generated by thermal treatment in reducing the gas atmosphere. Typically, H_2 and CO are used as reducing gases. The evolution of oxygen vacancies over titania could be written according to Kröger-Vink notation (Equation **2.9**):

$$O_O \overset{TiO_2}{\longleftrightarrow} V_O + \frac{1}{2}O_{2(g)} + 2e^- \qquad \textbf{2.9}$$

The equilibrium constant for the above Kröger-Vink equation is represented by the following equation (Equation **2.10**):

$$K = [\mathrm{V_O}]\mathrm{n}^2 p(\mathrm{O_2})^{1/2} \qquad \textbf{2.10}$$

The above equation could be rearranged in terms of oxygen vacancy concentration (Equation **2.11**):

$$[\mathrm{V_O}] = K\mathrm{n}^{-2} p(\mathrm{O_2})^{-1/2} \qquad \textbf{2.11}$$

Thus, it could be deduced from the above equation that the concentration of oxygen vacancies could be enhanced upon reducing the oxygen partial pressure[58].

Upon the generation of oxygen vacancy, the oxygen atom that leaves the surface also leaves behind two electrons on the vacant sites. These electrons could either reduce Ti^{4+} cations to Ti^{3+} or remain at the oxygen vacancy sites which depends on several factors such as reducing the temperature, concentration, and partial pressure of the reducing gas[57,59].

H. Liu et al.[60] elucidated the effect of treatment temperature on the formation of Ti^{3+} and oxygen vacancies with trapped electrons. With EPR characterization (Figure 2.12), it was found that the H_2 treatment under 450°C caused the formation of oxygen vacancies with trapped electrons only. However, as the H_2 treatment temperature was increased above 450°C, both Ti^{3+} and oxygen vacancy signals with trapped electrons were detected[60].

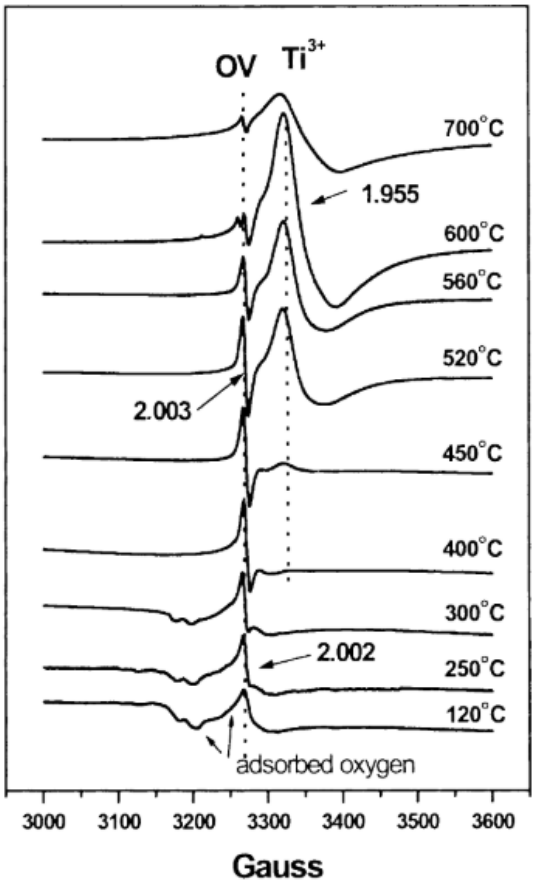

Figure 2.12. EPR spectra of TiO_2 at different H_2 treatment temperatures [60]

A similar pattern was observed by Li et al. [61]. The authors elucidated the effect of different H_2 pretreatment temperatures on propane dehydrogenation activity (Discussed in detail in section 2.6.2.1). It was found that upon increasing the H_2 treatment temperature, the signal associated with the oxygen vacancies with trapped electrons decreased in intensity. On the other hand, the signal associated with the Ti^{3+} increased in intensity with an increase in reduction in treatment temperature.

2.5.3.2 Incorporating oxygen vacancies during *in situ* synthesis of titania

Unlike the post-treatment method to generate oxygen vacancies in titania, there are several ways to incorporate oxygen vacancies in titania such as metal or non-metal doping, reduction with hydrides, and reduction with organic/inorganic reagents to name a few.

Doping of low valence metal during the synthesis of metal oxides is a widely used method to include oxygen vacancies in titania. Yunxuan and coworkers [62] investigated the effect of copper doping on the concentration of oxygen vacancies. The increase in oxygen vacancy concentration upon increasing copper doping was reflected in the UV-Vis spectroscopy. Copper-doped titania showed an enhanced photocatalytic reduction of N_2 to NH_3 in an aqueous medium. The absorption edge shifted from 400nm to 700nm after copper doping. The underlying phenomena behind the formation of oxygen vacancies upon doping low valence metals are the compensation of positive and negative charges [62]. Similarly, other metals such as zinc and aluminum could also be used to incorporate oxygen vacancies in titania [63,64].

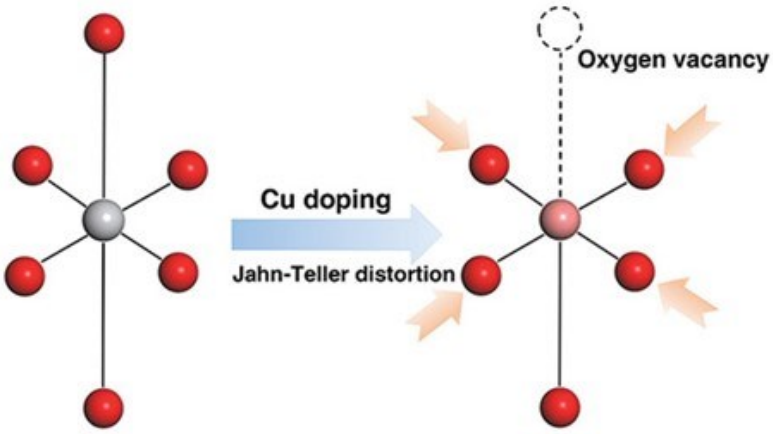

Figure 2.13. Representation of oxygen vacancy generation in titania due to copper doping[62]

Metal doping to induce oxygen vacancies in titania is not only limited to transition metals but other classes of metals such as alkaline earth metals, noble metals, and lanthanides metals could also be used to incorporate oxygen vacancies in titania. Jiale and coworkers investigated the effect of doping lanthanide metals on the oxygen vacancies in $Na_2Ti_3O_7$. When lanthanide metal was doped in $Na_2Ti_3O_7$, the lattice structure was slightly distorted which resulted in oxygen vacancies. The positive effect of induced oxygen vacancies with lanthanide metals was reflected in the improved performance of sodium-ion batteries[65].

Unlike metal doping, doping of nonmetal elements such as sulfur, nitrogen, carbon, and halogens is yet another way to prepare oxygen vacancy-rich titania. Li et al. [66] prepared oxygen vacancies rich titania by fluorine(F) doping. Spray pyrolysis of H_2TiF_6 precursor at different temperatures was carried out to control the oxygen vacancies in titania. UV-Visible spectroscopy results revealed that the absorption edge of titania remained unchanged. This indicates that F-doping does not alter the electronic structure of titania. However, the photoluminescence spectroscopy confirmed the evolution of oxygen vacancies upon fluorine doping. The samples were tested for acetaldehyde and trichloroethylene decomposition. Samples with a high amount of oxygen vacancies exhibited higher decomposition activity in comparison with P25[66].

Chlorine could also be doped in titania to induce oxygen vacancies. Cao et al. doped titania with chlorine using a chloroprene binder. Chloride-doped titania samples exhibited oxygen vacancies as revealed by EPR and XPS characterizations. Photoluminescence spectroscopy of Cl-doped and pristine titania revealed that chlorine doping resulted in lower photoluminescence intensity in comparison with pristine titania. This phenomenon is associated with a lower probability of electron-hole recombination due to oxygen vacancies. The authors suggested that doped chlorine atoms replaced oxygen atoms in titania lattice which induced Ti^{3+} and oxygen vacancy defects. Cl-doped and pristine titania were tested for photocatalytic degradation of dyes. Cl-doped titania exhibited enhanced photocatalytic activity for degradation of dyes in comparison with undoped titania samples[67].

Other nonmetals such as carbon, nitrogen, and boron have also been reported in the literature to tune the defects in titania. Similar to the above discussion, doping these nonmetals induces oxygen vacancies on titania. This increases the light absorption in the visible range and the modified catalysts exhibit higher photocatalytic performance[68–71].

Reduction by hydrides is yet another post-treatment method to incorporate oxygen vacancies in titania. Common hydrides include $NaBH_4$, N_2H_4, and CaH_2. The procedure involves mixing titania powder with the hydride and calcining under an inert atmosphere. Different temperatures and calcination times can result in different amounts of oxygen vacancies. Tan et al. [72] utilized $NaBH_4$ to tailor the oxygen vacancies in titania(P25). $NaBH_4$ mixed with titania was calcined under argon flow at different reaction temperatures and times. The control of calcination time and temperature resulted in the change of titania color from white to blue and finally to black. The diffused reflectance spectroscopy revealed that the light absorption in the visible range increased as the color of titania became more intense which is associated with the increased oxygen vacancies. Unlike the Hydrogen treatment method, using reducing agents such as $NaBH_4$ can greatly reduce and minimize the reaction time and temperature to incorporate oxygen vacancies in titania. When $NaBH_4$ is used as a reducing agent, it can undergo decomposition at a lower temperature to yield active hydrogen(H) species which are more effective in inducing oxygen vacancies in comparison with H_2 [72].

Metals such as magnesium, aluminum, and zinc can also be used as reducing agents to control the oxygen vacancies on titania. Apurba and coworkers [73] studied the effect of magnesium powder on the oxygen vacancies in titania. Briefly, magnesium powder was mixed with titania and heated under a hydrogen atmosphere at 650°C for 5h. Thereafter, the sample was treated with HCl to remove magnesium powder. The final titania powder exhibited light absorption in the visible light region due to the generation of oxygen vacancies. 1% platinum was incorporated on the final titania samples obtained after reduction which were later tested for hydrogen production from a methanol-water system. Hydrogen production was increased

when the molar ratio of magnesium to titania was increased up to 0.5. Thereafter, the hydrogen production rate was reduced. This finding revealed the synergistic role of magnesium and hydrogen to incorporate oxygen vacancies on titania[73].

Incorporating oxygen vacancies in titania is not only limited to metal, nonmetal doping, or hydrogen treatment. Reduction by organic and inorganic chemicals is yet another way to tailor oxygen vacancies in titania. Zuo et al. utilized the combustion method with 2-ethylimidazole. The combustion at 500°C in air resulted in reducing gases like NO and CO which greatly assisted the reduction of titania. Here also, UV-visible spectroscopy was used to qualitatively characterize the oxygen vacancies. Titania samples prepared with the combustion of 2-ethylimidazole showed light absorption in the visible range in comparison with pristine titania. The light absorption in the visible range was associated with the induced oxygen vacancies [74].

Similarly, other organic reagents such as ethylene glycol and ascorbic acid could be used to prepare oxygen vacancy-rich titania materials. Babu et al. hydrothermally synthesized oxygen vacancy-rich titania catalyst using ascorbic acid. The concentration of ascorbic acid was varied to control the oxygen vacancies. Increasing ascorbic acid concentration resulted in the change of titania color from white to brown associated with the increasing oxygen vacancies. The induced oxygen vacancies also resulted in light absorption in the visible range and the narrowing of the band gap from 3.2eV to 2.0eV. These samples were tested for hydrogen evolution reaction in deionized water and glycerol mixture. The rate of hydrogen production was maximum when 0.5M ascorbic acid was used to tune the oxygen vacancies in titania. Thereafter, increasing the concentration of ascorbic acid resulted in a decrease in hydrogen production[74].

Unlike metal/nonmetal doping, oxygen vacancies could be induced on titania by hydroxylation. Fan et al. prepared oxygen vacancies rich titania by incorporating hydroxyl groups. These groups were introduced by ultrasonication using titanium sulfate and aqueous ammonia as precursors. The duration of the ultrasonication

varied from 30 minutes to 8h which resulted in the change of titania color from white to black. Hydroxylation resulted in the band gap narrowing of modified titania samples which showed enhanced light absorption in comparison with untreated titania[75].

2.5.4 Synthesis of titania particles via sol-gel method

In heterogeneous catalysis, the sol-gel process is one of the fundamental routes of catalyst synthesis. This technique offers good control over the size and growth of particles. At relatively low temperatures, the sol-gel process can yield pure particles with good uniformity. This process is a bottom-up wet chemical method and is mainly used for the synthesis of metal oxides. Typically, the sol-gel synthesis takes place under an acidic or basic medium and the reagents for the synthesis include alcohol, metal alkoxide or inorganic metal precursor, and water[76,77]

The underlying reactions during the sol-gel process include hydrolysis and condensation. Firstly, the metal precursor undergoes hydrolysis yielding a colloidal suspension(sol). Then, upon aging, the polycondensation of hydrolyzed products(gelation) results in the polymeric network of metal oxide. Here gelation means the formation of viscous material containing both the liquid and solid phases. Once the sol-gel process is complete, the gel is dried and calcined to remove the solvent and other residues. The crystallinity of the final solid material is affected by the thermal treatment conditions. Sol-gel synthesis carried out at low-temperature results in poor crystallinity. Depending on the calcination temperature, heating rate, and time, the crystal phase composition of metal oxide particles could be controlled. Sol-gel technique also offers control over the textural properties of the final material. Parameters affecting the textural properties include pH, synthesis temperature, precursor concentration, solvent concentration, and presence of template. [78–80].

2.5.5 Sol-gel chemistry for titania

Sol-gel synthesis of titania particles involves hydrolysis and condensation steps. Titanium (IV) isopropoxide or Titanium (IV) butoxide are typically used as titanium precursors. These organic precursors react immediately with water and are thus ideal precursors for sol-gel synthesis[81]. The schematic of the sol-gel synthesis is given in Figure 2.14.

Hydrolysis

In the first hydrolysis step, the organic precursor ($Ti(OR)_4$, where R represents the alkyl group) reacts with water whereby one alkyl group is detached from the precursor to yield ROH and HO-$Ti(OR)_3$ (Equation **2.12**)

$$Ti(OR)_4 + H_2O \rightarrow HO - Ti(OR)_3 + R - OH \qquad \textbf{2.12}$$

The precursor may be partially or totally hydrolyzed, depending on the catalyst and water content. The successive steps in the hydrolysis process are listed below:

$$HO - Ti(OR)_3 + H_2O \rightarrow (HO)_2 - Ti(OR)_2 + R - OH \qquad \textbf{2.13}$$

$$(HO)_2 - Ti(OR)_2 + H_2O \rightarrow (HO)_3 - Ti(OR) + R - OH \qquad \textbf{2.14}$$

$$(HO)_3 - Ti(OR) + H_2O \rightarrow Ti(OH)_4 + R - OH \qquad \textbf{2.15}$$

Condensation

The condensation could either result in the liberation of alcohol or water molecule. In the case where a water molecule is released, two partially hydrolyzed molecules can bond together to form -**Ti-O-Ti**- network as seen in (Equation. **2.16**):

$$(OR)_3 - Ti(OH) + HO - Ti(OR)_3 \leftrightharpoons (OR)_3 - \mathbf{Ti} - \mathbf{O} - \mathbf{Ti}(OR)_3 + H_2O \qquad \textbf{2.16}$$

The condensation could also occur with the release of alcohol molecules as seen in Equation **2.17**:

$$(OR)_3 - Ti - OR + HO - Ti(OR)_3 \leftrightharpoons (OR)_3 - \mathbf{Ti} - \mathbf{O} - \mathbf{Ti}(OR)_3 + R - OH \qquad \textbf{2.17}$$

Thus, these condensation reactions can continue to yield a polymeric network of Ti-O-Ti. When sufficient condensation has occurred, water and other organic residues are trapped inside the gel which is removed upon thermal treatment[82–85].

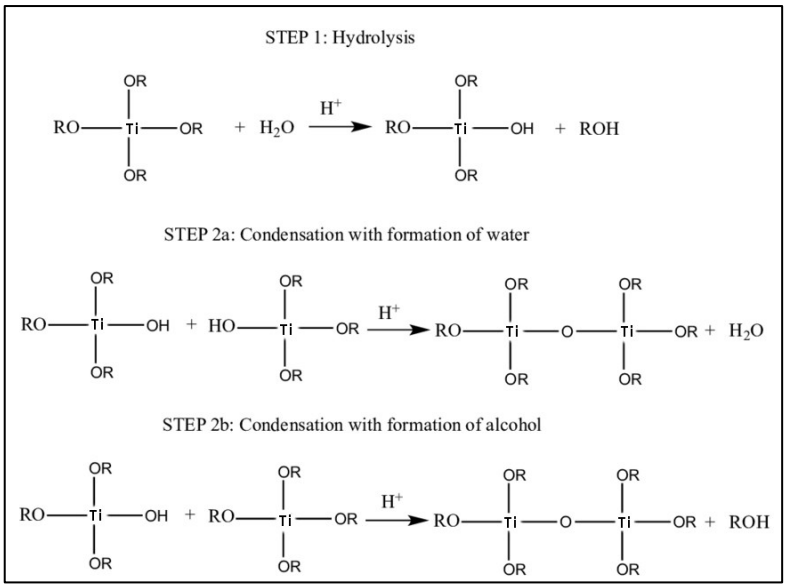

Figure 2.14. Sol-gel chemistry of titania particles

2.6 Literature study of alternative bulk metal oxide catalysts for non-oxidative propane dehydrogenation

The following discussion will highlight the recent studies where the bulk non-noble and non-toxic metal oxides are used for non-oxidative propane dehydrogenation. Before describing active sites involved in non-oxidative propane dehydrogenation, it is essential to understand the general concept of active sites in heterogeneous catalysis.

2.6.1 Active sites

The fundamental understanding of active sites in heterogeneous catalysis was first laid by Hugg Stott Taylor. The author postulated that the active sites on a catalyst involve a fragment of the surface. This could include atoms, a combination of atoms, or the material defects such as vacancies, edges, or other discontinuities[86]. Based on Taylor's concept of active sites, Boudart[87] categorized the heterogeneous chemical reactions as surface sensitive and surface insensitive. A *surface insensitive* reaction would show a negligible change in the rate of reaction with respect to particle size or the exposed crystallographic planes. Ethylene hydrogenation over platinum is a typical surface insensitive reaction. For this reaction, the rate of ethane formation is not affected by the crystal structure of platinum or varying the dispersion of platinum particles[88].

On the other hand, the rate of a *surface-sensitive* reaction would change significantly with respect to particle size or exposed crystal planes. Many industrially important reactions such as ammonia synthesis over iron catalyst[89], alkane aromatization over platinum catalyst[90], and non-oxidative propane dehydrogenation over zirconia[91] or titania catalyst[92] are structure-sensitive reactions.

2.6.1.1 Active sites in propane dehydrogenation

In conventional non-oxidative propane dehydrogenation catalysts, active sites are the supported metal (Pt) or metal oxides (CrO_x). Factors determining their activity and selectivity are typically the metal or metal oxide-support interaction and their fine structure. However, during the harsh reaction conditions, the fine structure is damaged and the catalyst undergoes rapid deactivation.

On the other hand, the active sites of alternative bulk metal oxides catalysts comprise surface defects (Figure 2.15). Such defects are oxygen vacancies that are created upon reductive treatment at high temperatures. The reductive treatment leads to the formation of coordinatively unsaturated metal cation and oxygen vacancy which serve as active sites for non-oxidative propane dehydrogenation. In the literature, the active sites for bulk metal oxides such as TiO_2, ZrO_2, and Al_2O_3 are all related to coordinatively unsaturated cations and oxygen vacancies. However, the nature of active sites and their characterization have been reported differently.

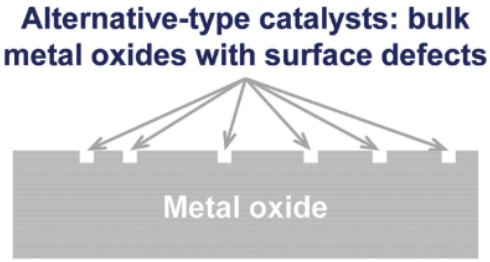

Figure 2.15. The active site for alternative bulk oxide[23]

In the case of ZrO_2, the active site for non-oxidative propane dehydrogenation was first proposed as Zr_{cus} and lattice oxygen pair which is responsible for the activation of the C-H bond[93,94]. However, later with the aid of density functional theory (DFT) and experimental studies, it was found that active sites were different from defective (ZrO_x) and non-defective zirconia (ZrO_2). For defective zirconia, the active site comprises two neighboring Zr_{cus}^{4+} sites responsible for C-H bond activation. On

the other hand, non-defective zirconia has a pair of Zr^{4+} and neighboring lattice oxygen as an active site[95]. Since the coordinatively unsaturated Zr_{cus} sites and oxygen vacancies are generated upon reductive treatment[96], *in-situ UV-Visible spectroscopy* can be used to monitor their formation. During the reductive treatment, the color of the zirconia catalyst changes from white (ZrO_2) to grey (ZrO_x). The underlying phenomena behind this change are that the energy levels above the valence band undergo several transitions during the creation of oxygen vacancies by reductive treatment. The transitions subsequently cause absorption in the visible range[97]. In line with these fundamentals, Otroshchenko et al.[94] observed for zirconia-based catalysts that the maxima at 420nm increased in intensity with increasing time. With the increase in temperature, the rate of formation of maxima at 420nm also increased. Thus, it was confirmed that oxygen vacancies are formed under H_2 reductive treatment and their concentration increases with increasing temperature.

Titania (TiO_2) is another bulk oxide that was first introduced in 2020 as an alternative catalyst for non-oxidative propane dehydrogenation. Similar to zirconia, the active sites for propane dehydrogenation over titania are related to oxygen vacancies. Studies based on density functional theory (DFT) revealed that over non-defective titania, the active sites are twofold coordinated oxygen atoms. On the other hand, the active sites over defective titania are fourfold coordinated titanium atoms with neighboring oxygen vacancies[98]. Like zirconia, the oxygen vacancies and coordinatively unsaturated titanium cations are generated upon reductive treatment [58], and *electron spin resonance (ESR) spectroscopy* can be used to monitor the generation of these sites. The generation of oxygen vacancies leads to the formation of unpaired electrons or Ti^{3+} cations which can be monitored with ESR[99]. In a typical ESR, a fixed frequency microwave is incident on the sample and a variable magnetic field is applied. The magnetic field causes the spin of the unpaired electron to align parallel (low energy) and antiparallel (high energy) to the applied magnetic field. By varying the magnetic field, the energy difference between the two energy states of electron spin is adjusted to match the energy of the applied microwave.

Thereafter, the unpaired electrons can move from the lower energy state to the higher upon absorbance of energy of applied microwave and the absorbance signal is recorded [100]. The signal due to oxygen vacancy is typically observed at a magnetic moment(g) of 2.003 [101]. For propane dehydrogenation, Li et al.[98] found that oxygen vacancies (active sites) could be generated by hydrogen reductive treatment or in situ during propane dehydrogenation by electron paramagnetic resonance (EPR). The strong EPR signal was found to be related to the high propane conversion which supports the claim that active sites are related to oxygen vacancies. Xie et. al[92] also monitored the generation of active sites over TiO_2 with ESR. The oxygen vacancy signal (g=2.003) increased in intensity with time on-stream propane dehydrogenation reaction, thus authors confirmed that oxygen vacancies and coordinatively unsaturated Ti cations are generated in situ during non-oxidative propane dehydrogenation reaction. The authors contended that oxygen vacancies are formed due to Ostwald ripening of TiO_2 nanoparticles at a high temperature which causes the mobility of lattice oxygen atoms[92].

Alumina (Al_2O_3) is yet another alternative bulk oxide catalyst for non-oxidative propane dehydrogenation. The active sites for bulk alumina are also reserved to surface defects (coordinatively unsaturated Al^{3+} cations). DFT calculations revealed that C-H activation over alumina depends on the coordination of Al^{3+} species. The most active site for propane dehydrogenation was found to be the tri-coordinated Al-O pair[102]. For the characterization of these active sites, *Pyridine-Fourier Transform Infrared Spectroscopy (FTIR)* can also be used. When used as a basic probe molecule, Pyridine adsorbs on specific Bronsted and Lewis acidic sites which are identified by FTIR signal at specific wave numbers[103,104]. Wang et al. [105] utilized the Py-FTIR technique to determine the active sites(Lewis sites) for propane dehydrogenation over bulk alumina with the finding of a linear relation between the amount of Lewis acidic sites and propane conversion.

2.6.2 Factors affecting the non-oxidative propane dehydrogenation activity over bulk oxides

2.6.2.1 Effect of pretreatment conditions

As discussed in section 2.6.1, the active sites over bulk oxides are coordinatively unsaturated cations with neighboring oxygen vacancies. These sites could be generated upon the reductive pretreatment and their concentrations could be adjusted with different treatment conditions [23].

The effect of pretreatment conditions over bare zirconia for non-oxidative propane dehydrogenation has been well studied. The findings of Otroshchenko et al. [106] revealed that the rate of propene formation over air-treated(oxidized) zirconia is significantly lower than over H_2-treated(reduced) zirconia at a specific temperature. The higher rate of propene formation over reduced samples is due to higher concentrations of coordinatively unsaturated zirconium sites which are generated upon the removal of lattice oxygen by H_2 pretreatment. Reduction temperature can also affect the rate of propene formation over zirconia. For bare zirconia, the rate of propene formation increased linearly when the H_2-reduction temperature increased from 550 to 650°C indicating that more oxygen vacancies are formed at higher temperatures. Thus, reduction at high temperature facilitates the removal of lattice oxygen and more active sites could be generated. Utilizing a stronger reducing agent is yet another way of controlling the active sites over bulk oxides. Zhang et al. [95] demonstrated that treating zirconia with H_2 takes approximately 6h to get twice the rate of propene formation in contrast with untreated zirconia. However, when pre-treating zirconia with CO the rate of propene formation increased to seven-fold in approximately 30mins in comparison with untreated zirconia. CO has a stronger reducing ability to remove the lattice oxygen from zirconia in comparison with H_2. Thus, more oxygen vacancies and associated actives sites are created over zirconia after CO treatment in comparison with H_2 treatment which results in a higher propene formation rate.

Similarly, the activity of titania could be adjusted with different pretreatment conditions. A similar pattern is observed over bare titania for non-oxidative propane dehydrogenation. Li et al. [98] demonstrated that treating bare TiO_2 under air resulted in significantly lower propane dehydrogenation activity in comparison with H_2-treated TiO_2 at 600°C. Since the active sites are coordinatively unsaturated Ti^{4+} cations with neighboring oxygen vacancies, air treatment reduces their concentrations. However, H_2 treatment facilitates the removal of lattice oxygen, thus more active sites are available for propane dehydrogenation. Similar to zirconia, the active sites(oxygen vacancies) over bare titania could be controlled by hydrogen treatment at different temperatures[60]. Li et al. [98] treated bare TiO_2 under H_2 at different temperatures before the propane dehydrogenation activity. Unlike ZrO_2, TiO_2 exhibited a negative trend with increasing temperature for propane dehydrogenation activity. EPR characterization revealed that the oxygen vacancy signal reduced in intensity with increasing temperature and the signal associated with Ti^{3+} increased with increasing temperature. Thus, at a higher temperature, TiO_2 undergoes over reduction resulting in Ti^{3+} species which are inactive for propane dehydrogenation.

2.6.2.2 Effect of crystalline phase and crystallite size

Non-oxidative propane dehydrogenation activity over bulk oxides can also be controlled by adjusting the phase composition. Over bare zirconia, Zhang et al. [107] demonstrated that different phase of zirconia exhibits different propane dehydrogenation activity. The monoclinic phase of zirconia exhibits higher propane dehydrogenation activity in comparison with the tetragonal phase. In order to understand the underlying phenomena behind this difference, the authors performed DFT calculations over defective monoclinic and tetragonal zirconia. Their findings revealed that propane dehydrogenation steps over both monoclinic and defective zirconia follow the same pattern with the same active sites. However, over monoclinic zirconia, the propene formation occurs easily in comparison with the tetragonal phase because of the lower energy requirement for C-H activation. The authors also demonstrated that regardless of the phase composition, the propane dehydrogenation activity and selectivity to propene increases with the decrease of the crystallite size. The small crystallite size increases the ease of lattice oxygen removal (reducibility) and thus more active sites are available for propane dehydrogenation. The ease of reducibility was confirmed by the CO-TPR experiment where a higher CO consumption rate was observed for smaller crystallite sizes, thus smaller crystallite size zirconia facilitates the removal of lattice oxygen and more active sites are generated over smaller crystallite sizes. On the other hand, the increased selectivity to propene over small zirconia crystallites is due to the difference in the active sites for coke and propene formation. The active sites for coke formation and propene formation are regular Zr and Zr_{cus} respectively. As the crystallite size decreases, Zr_{cus} sites increase while regular Zr sites decrease. Thus, with smaller crystallites fewer active sites for coke formation are available and higher selectivity to propene is achieved.

Similarly, titania also exhibits different propane dehydrogenation activity with different titania phases. Li et al. [98] demonstrated that anatase titania exhibits significantly higher propane dehydrogenation activity and propene selectivity in

comparison with rutile titania. Since the active sites over titania are related to oxygen vacancies, the authors investigated the rutile and anatase titania with EPR. While anatase titania exhibited oxygen vacancy EPR signal, no signal for oxygen vacancy was detected for rutile titania. This implies that the generation of active sites (Ti_{cus} with neighboring oxygen vacancies) over anatase titania occurs easily in comparison with rutile titania, thus propane dehydrogenation activity and selectivity to propene are higher over anatase titania. Whether the reaction pathway and the active sites for propane dehydrogenation over anatase and rutile TiO_2 are the same needs further investigation. Xie et al. [92] investigated the effect of crystallite size on propane dehydrogenation activity. Similar to zirconia, the rate of propene formation increased with the decrease of the TiO_2 crystallite size. As discussed earlier, the generation of active sites is related to the Ostwald ripening of TiO_2 particles. Over small TiO_2 crystallites, Ostwald ripening occurs easily and thus more active sites are available for propane dehydrogenation in comparison with larger crystallites.

CHAPTER 3

EXPERIMENTAL

This chapter focuses on the description of the catalyst synthesis procedure followed by in-situ and ex-situ characterization techniques of the synthesized catalyst. In the end, the working of the gas phase activity system for non-oxidative propane dehydrogenation activity is discussed.

3.1 Sol-gel synthesis of TiO_2 particles

3.1.1 Chemicals

The following chemicals are used to synthesize titania.

(i) Absolute Ethanol (Sigma-Aldrich 64-17-5)
(ii) Ultra-Pure (UP) water (Chemical Engineering Department, Middle East Technical University)
(iii) Acetic Acid (Sigma-Aldrich 64-19-7)
(iv) Hydrochloric acid (Sigma-Aldrich 7647-01-0)
(v) Titanium (IV) isopropoxide (Sigma-Aldrich 546-68-9)

3.1.2 Synthesis procedure

Titania particles were synthesized by a sol-gel method by Bouziani et al. [108] recipe. The schematic of the synthesis procedure is given in Figure 3.1 below:

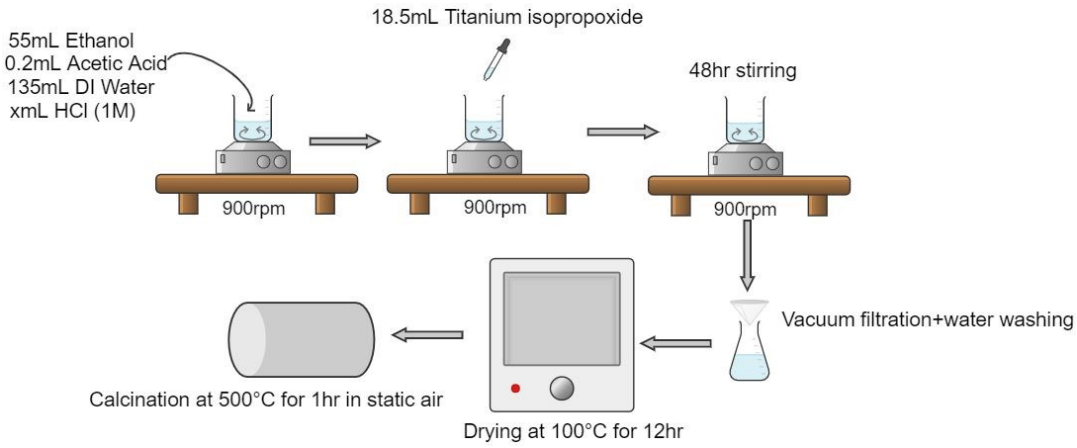

Figure 3.1. Sol-gel synthesis procedure for titania particles

For the synthesis of pristine titania, 55mL of absolute ethanol, 135mL UP water, and 0.2mL acetic acid was added to a beaker. Then, 18.5mL titanium (IV) isopropoxide was added dropwise to the mixture. The mixture was left under continuous magnetic stirring for 48h at room temperature. Thereafter, the titania powder was obtained by vacuum filtration and water washing. The obtained titania powder was dried for 12hr at 100°C and calcined at 500°C for 2h to ensure the removal of adsorbed water and any organic residues. Synthesized samples were abbreviated as ST where **S**: Sol-gel and **T**: Titania.

For HCl treatment, the synthesis procedure is the same as that for pristine titania, however certain amount(abbreviated as x) of 1M HCl is added before introducing titanium precursor during the sol-gel synthesis. Samples were abbreviated as xSCT, where x: volume(mL) of HCl added, **S**: Sol-gel, **C**: Indicates that the sample synthesized with H**C**l addition, and **T**: Titania.

3.2 Catalyst Characterization

3.2.1 Textural Properties

Nitrogen physisorption analysis was carried out to determine the surface area and pore size distribution of the synthesized catalysts using Brunauer–Emmett–Teller (BET) and Barret-Joyner-Halenda (BJH) theories respectively. The device used for the analysis was Micromeritics TriStar II 3020 in the METU Department of Chemical Engineering. Before the analysis, catalysts were degassed at 350°C for 4h.

3.2.2 Thermal Gravimetric Analysis(TGA)

The thermal stability of synthesized catalyst samples was analyzed using the Shimadzu DTG-60 device in the METU Department of Chemical Engineering. For a typical analysis, approximately 20mg of catalyst sample was heated from room temperature to 900°C at a ramp rate of 10°C/min under 60mL/min air flow. TGA (mg) and DTA (uV) signals with respect to time and temperature were obtained.

3.2.3 X-ray Diffraction (XRD)

The phase composition and crystal structure of the synthesized catalysts were analyzed using a Rigaku Ultima-IV diffractometer in the METU Department of Metallurgy and Materials Engineering. The device is equipped with a monochromatic Cu-Kα irradiation source of 1.54056 Å operating at 40kV and 30mA. Scans were performed in the range from 10-65° at 0.02°/s.

Average crystallite sizes were calculated using Scherrer Equation[109] given below:

$$d = \frac{k\lambda}{\beta \mathrm{Cos}\theta}$$

where,

k: Shape factor constant

λ: X-ray wave length

β: Full width at half maximum (FWHM)

θ: Bragg angle

A sample calculation showing the crystallite size calculation using the Scherrer equation is given in Appendix A.

3.2.4 Raman Spectroscopy

Synthesized samples were characterized by Raman spectroscopy to elucidate the crystallinity and formation of oxygen vacancies. The scans were performed on Ramanscope II in METU Central Laboratory. This device is equipped with a 532nm laser beam.

3.2.5 Surface Morphology and Elemental Analysis

Scanning electron microscopy (SEM) analysis was performed in order to determine the morphology of synthesized catalysts using the VEGA3 TESCAN instrument in the METU Department of Chemical Engineering. Before the analysis, 2mg of catalyst samples were dispersed in 2mL of ultrapure water and sonicated for 20mins. Thereafter, a drop of sonicated solution was dried on a glass substrate. Once the solution on the glass substrate was dried, gold-palladium coating was performed over the substrate to avoid charge accumulation on the sample during the analysis. Subsequently, SEM was performed at 5.0kV with a working distance (WD) of 10mm. The device is equipped with Energy dispersive X-ray (EDX) detector, thus elemental analysis of the samples was also performed at 10.0kV.

3.2.6 X-ray Photoelectron Spectroscopy (XPS)

X-ray photoelectron spectroscopy was performed to understand the surface characteristics of the synthesized catalysts. PHI 5000 VersaProbe XPS instrument in METU Central Laboratory was used for XPS analysis. Al Kα was the X-ray source and the binding energies were calibrated using C 1s peak (284.5eV)

3.2.7 UV-Visible Diffused Reflectance Spectroscopy (DRS)

UV-Visible diffused reflectance spectroscopy (DRS) was carried out for the synthesized catalysts using the SHIMADZU UV-2600i instrument in the METU Department of Chemical Engineering. Barium sulfate (BaSO4) was used both as a reference and diluting material. Reflectance spectra were obtained in the range of 220-1400nm. DRS was also performed for catalysts reduced under 30sccm pure H_2 flow at 500°C to compare the optical properties with fresh catalysts.

3.2.8 In-situ DRIFTS of Adsorbed Pyridine

The surface acidity of the synthesized catalysts was determined using pyridine-FTIR spectroscopy using JASCO FT/IR device equipped with a reaction cell (Harricks-Praying Mantis). Before the measurement, the sample was purged with Argon to ensure the removal of physically adsorbed water at 500°C. Thereafter, the sample was reduced with dilute H_2 for the generation of active sites at 500°C for 1h. After reduction, the background scan was taken at 450, 350, 250, 150, and 50 °C under Ar flow. Then Pyridine vapor was introduced to the chamber without exposure to air and was adsorbed for 30mins at 50°C. Then, the flow was switched to Ar and Pyridine desorption spectrum was obtained at 50, 150, 250, 350, and 450 °C in the range of 400-4000cm^{-1} with 4cm^{-1} resolution and 256 scans accumulations.

3.2.9 Temperature Programmed Reduction(TPR)

The redox properties of the synthesized catalysts were investigated with temperature programmed reduction (TPR) of carbon monoxide (CO) or hydrogen(H_2). 200mg of catalyst sample was loaded into a ¼" quartz tubular reactor. The sample was heated under Ar flow to 550°C at 10°C/min. Thereafter, 30sccm of 10 vol% O_2 in Ar was fed to the reactor for 1h at the same temperature. The catalyst was then cooled to room temperature under Ar flow. Thereafter, 30sccm of 3 vol % H_2 in Ar or 30sccm of 10 vol% CO in Ar was fed to the reactor while heating the reactor at 10°C/min to 900°C. The consumption of CO or H_2 was monitored by an online mass spectrometer (HIDEN HPR20). The following signals were observed by mass spectrometer:

Table 3.1 Signals observed during CO/H_2-TPR

CO-TPR	H_2-TPR
CO(m/z): 28, 12	H_2(m/z): 2,1
CO_2(m/z): 44, 16	H_2O(m/z):18,17
H_2(m/z): 2,1	CO_2(m/z): 44, 16
H_2O(m/z):18,17	N_2(m/z):14
N_2(m/z):14	C(m/z):12
O_2(m/z):32	O_2(m/z):32

3.2.10 Temperature programmed surface reaction (TPSR)

Temperature programmed surface reaction (TPSR) was performed to investigate the in-situ reduction of titania during non-oxidative propane dehydrogenation. 50mg of titania catalyst was loaded into a ¼" quartz tubular reactor and heated to 600°C at 10°C/min under 30sccm Ar flow and kept for 1h. The catalyst sample was then cooled down to room temperature under Ar flow. Thereafter, 30sccm of 7 vol % C_3H_8 in Ar was fed to the reactor and the temperature was raised to 900°C at 10°C/min. The following signals were monitored with a mass spectrometer (HIDEN HPR20):

Table 3.2 Signals observed during TPSR-C_3H_8

Components	m/z
H_2	2
H_2O	18
$CO+CO_2$	12
C_3H_6	42
C_3H_8	43
C_2H_6	30

3.3 Activity Tests

3.3.1 Experimental setup

Non-oxidative propane dehydrogenation activity tests were carried out in an in-house developed system. The schematic and real photograph of the activity system is shown in Figure 3.2 and Figure 3.3 respectively.

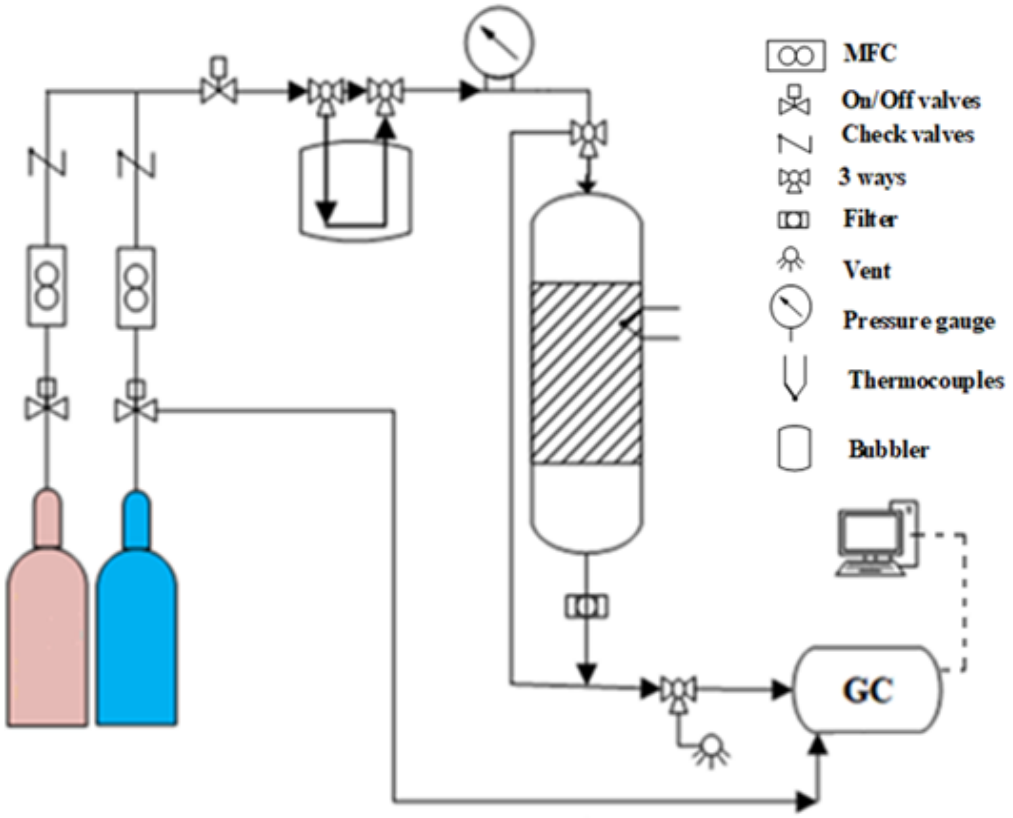

Figure 3.2. Schematic of propane dehydrogenation activity system

Figure 3.3. Propane dehydrogenation activity system (Real photograph)

The gas phase activity system was built using ¼'' stainless steel (SS) tubing. The setup comprises three specialized ALICAT mass flow controllers(MFCs). The outlet of these MFCs is equipped with a check valve which prevents the backflow of gases. Thus, this allows a flow of a mixture of gases with desirable composition and flow rates. With the use of a three-way valve, a bubbler can also be installed after the MFC's outlet line to introduce probing molecules such as water, if necessary for the activity. Thereafter, the line either bypasses the Gas Chromatograph (Agilent 8890) or follows the path into the ¼" quartz tubular reactor housed inside a vertical split

furnace (Protherm, Eurotherm 3208). The SS line which goes from the reactor outlet to the inlet of GC is heated and kept at 110°C to avoid water condensation in the lines. The heating of the SS line is assisted with the heating tapes which are controlled by the variac power supply. Depending on the reaction conditions, a condenser can also be placed at the outlet of the reactor to trap any water formed during the reaction before introducing the remaining effluents to the GC.

3.3.2 Quantification of effluents by online-gas chromatography

The effluents from the reaction are monitored with Agilent 8890 Gas Chromatography device. This device is equipped with three six-port pneumatic valves(Valve 1, Valve 2, and Valve 3) which direct the flow to the two capillary columns, viz.: Al_2O_3-S and molecular sieve columns. While the Al_2O_3-S column is suitable for the separation of light hydrocarbons(C1-C8), molecular sieve columns are suitable for the separation of permanent gases such as CO_x, N_2, H_2, and O_2. In our GC configuration, Al_2O_3-S is connected to the back Flame Ionization Detector (FID) detector which analyzes the hydrocarbons. The FID detector is kept at 275°C and the flame is assisted with pure hydrogen and dry air. On the other hand, the front Thermal Conductivity Detector (TCD) is kept at 250°C. TCD is connected to the molecular sieve for analyzing permanent gases. Argon is used as a carrier gas that assists the flow to the columns. During GC analysis, the oven temperature of GC is kept at 100°C. Run time for a single injection to the GC analysis last for 20mins and the following valve configurations (Table 3.3) is used to separate the hydrocarbons and permanent gases during a single run.

Table 3.3 Valve positions during GC injection analysis

Time(min)	Valve	Position
0.00	Valve 1	ON
0.10	Valve 3	ON
1.00	Valve 3	OFF
1.10	Valve 1	OFF
5.85	Valve 2	ON
12.50	Valve 2	OFF

3.3.3 Catalytic testing

In this study, all the non-oxidative propane dehydrogenation activity tests were performed at 1 bar using the experimental setup described in section 3.3.1.

For a typical non-oxidative propane dehydrogenation reaction, catalyst powders are loaded into the ¼" quartz tubular reactor. The catalyst bed is fixed in the center of the reactor with quartz wool at both ends of the bed. In some experiments where pressure build-up could be a problem, 50mg silica gel (Davisil 646, Sigma Aldrich) is mixed with 150mg of catalyst to prevent any pressure build-up during the reaction. The reactor is specifically designed to attach a thermocouple that can measure the temperature just above the bed in the reactor.

Once the catalyst bed is prepared, the reactor is heated under 30sccm Argon flow to the desired temperature at 10°C/min heating rate. Once the set point is reached, the catalyst is either pre-reduced using 30sccm of 3 vol% H_2 in Ar or 10 vol% CO in Ar flow for 1h. Hereafter, 30sccm of 7vol% propane in Ar is introduced to the reactor inlet and effluents are monitored with Agilent 8890 GC.

A blank experiment was performed using the same reactor equipped with the thermocouple mentioned above to examine the catalytic activity in the absence of a catalyst in the reactor at 550°C. The results in Figure B.4 reveal that the conversion and selectivity from blank propane dehydrogenation are about 0.05% and 68% respectively. Thus, the results from the blank experiment indicate negligible homogeneous catalytic activity under reaction conditions.

Propane conversion ($X_{C_3H_8}$) and propene selectivity($S_{C_3H_6}$) is calculated using equations **3.1** and **3.2** respectively.

$$X_{C_3H_8}(\%) = \frac{(\sum_{i=1}^{3} \gamma_i \times n_i) - (3 \times n_{C_3H_8})}{\sum_{i=1}^{3} \gamma_i \times n_i} \times 100\% \qquad \textbf{3.1}$$

$$S_{C_3H_6}(\%): \frac{3 \times n_{C_3H_6}}{(\sum_{i=1}^{k} \gamma_i \times n_i) - (3 \times n_{C_3H_8})} \times 100\% \qquad \textbf{3.2}$$

Where, γ_i: number of carbon atoms in the hydrocarbon, i and n_i: amount/concentration of hydrocarbon, i present in the effluent to the GC.

Further details for the calculation of the amount of hydrocarbons in the effluent are provided in Appendix C.

CHAPTER 4

RESULTS AND DISCUSSION

In this chapter, in-situ and ex-situ characterization results of synthesized catalysts are presented along with the non-oxidative propane dehydrogenation activity results.

4.1 Thermal Gravimetric Analysis(TGA)

TGA was performed under dry air to determine the thermal stability of the synthesized titania particles before any pretreatment. Figure 4.1. shows the plot of mass loss of uncalcined titania(ST and 6SCT) with respect to temperature changes. This thermogram can be divided into three stages. During the stage, I, the mass loss from room temperature to 150°C is due to the evaporation of physically adsorbed water, acetic acid, and other organic residues [110–112]. In stage II, from 150°C to 250°C, the mass loss can be attributed to the dehydroxylation [113–115]. Finally, in stage III, the mass loss from 250°C to 370°C can be attributed to the crystallization of titania to the anatase phase [114,116]. For ST sample, the shoulder peak at 410°C could be attributed to the decomposition of titanium precursor. After the crystallization, the sample remains stable until 900°C.

Since the crystalline phase composition of titania is affected by the calcination time and temperature, synthesized titania samples were calcined at 500°C for 1h. As can be seen from the TGA plots (Figure 4.1) This temperature is suitable enough to remove all the organic residues and adsorbed water and ensure only the anatase phase is present[114]. Also, the non-oxidative propane dehydrogenation reaction is generally performed between 500-700°C, titania particles have excellent stability in this temperature range as evident from the TGA curve.

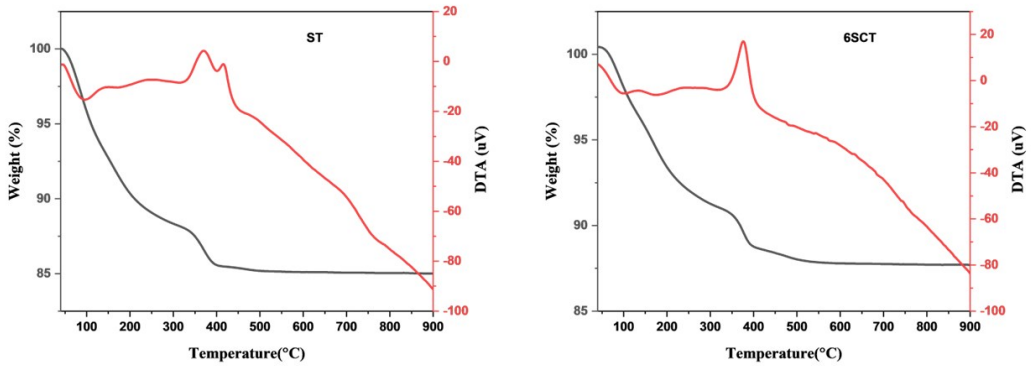

Figure 4.1. TGA DTA plot of titania

4.2 X-ray Diffraction (XRD)

X-Ray diffraction was performed to determine the crystallinity of the synthesized titania samples after calcination at 500°C for 1h. Figure 4.2 shows the diffraction patterns of synthesized titania samples in the 2θ range of 10-65°. All the samples exhibit diffraction peaks around 25.46°, 37.10°, 38.02°, 38.74°, 48.24°, 54.08°, 55.28°,62.86°, and 62.96° which corresponds to the anatase phase of titania in agreement with PDF-no. 96-152-6932. Thus, all the synthesized samples contain pure anatase phases without any traces of impurities.

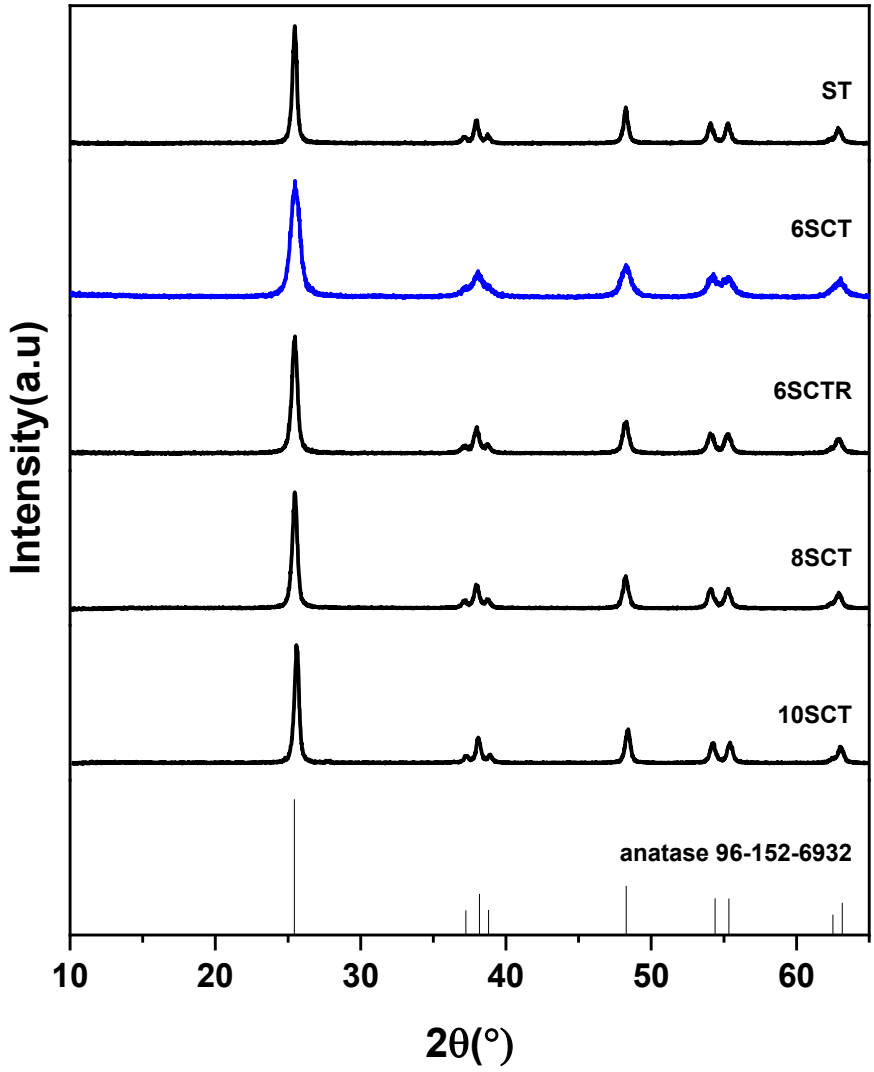

Figure 4.2. XRD patterns for synthesized titania catalysts

Crystallite size(d) was calculated using the Scherrer equation [109], $d=k\lambda/\beta Cos\theta$ where k is the shape factor constant, λ is X-ray wavelength, β is the full width at half maximum (FWHM) and θ is the Bragg angle. The crystallite sizes are tabulated below:

Table 4.1 Crystallite sizes of different synthesized titania catalysts

Catalyst	*Crystallite size(nm)*
ST	31.8
6SCT	16.4
6SCT (reduced)	28.6
8SCT	28.2
10SCT	31.0

XRD results of titania samples prepared with the addition of HCl during sol-gel synthesis showed slightly broader peaks. The broadening was the highest in the 6SCT sample which is reflected by the smallest crystallite size as determined with the Scherrer equation. Since H_2 reductive pretreatment is usually performed before the non-oxidative propane dehydrogenation experiment, XRD was also performed for 6SCT reduced under 30sccm H_2 flow at 500°C for 1hr to investigate the effect of H_2 treatment on phase composition and crystallinity. As evident from the XRD pattern, the anatase phase of titania remained unaltered after H_2 reduction treatment(6SCTR). However, the crystallite size increases from 16.4nm to 28.6nm after H_2 reductive treatment. This is reflected in the sharpening of anatase dominant peaks at 25.4° and 48.3° after H_2 reduction (Figure 4.3). This increase in the crystallite size is due to the Ostwald ripening process where the crystallites agglomerate at the expense of smaller crystallites[117]. The (200) diffraction peak for 6SCTR shifted to a higher diffraction angle in comparison with fresh TiO_2. This shift is mainly due to the decrease in the lattice parameter induced by the formation of oxygen vacancies under reductive treatment[54,118,119].

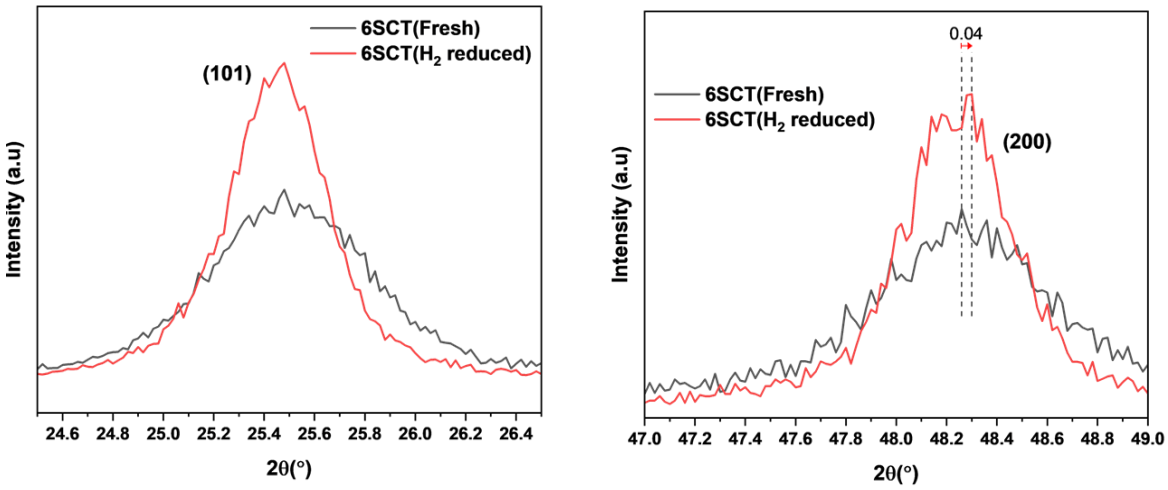

Figure 4.3. Locally amplified XRD pattern of fresh and H_2 reduced TiO_2

4.3 Raman spectroscopy

Raman spectroscopy is a vibrational spectroscopy technique that fundamentally relies on the scattering of incident light due to different chemical bonds[120]. Since the vibrations are unique to different chemical bonds, Raman spectroscopy can reveal information such as the chemical structure, phase composition, and chemical environment of the sample[121].

In our case, Raman spectroscopy was performed to elucidate the crystallinity and oxygen vacancies on untreated and HCl-treated titania. Figure 4.4 shows the Raman spectra of untreated and HCl-treated TiO_2.

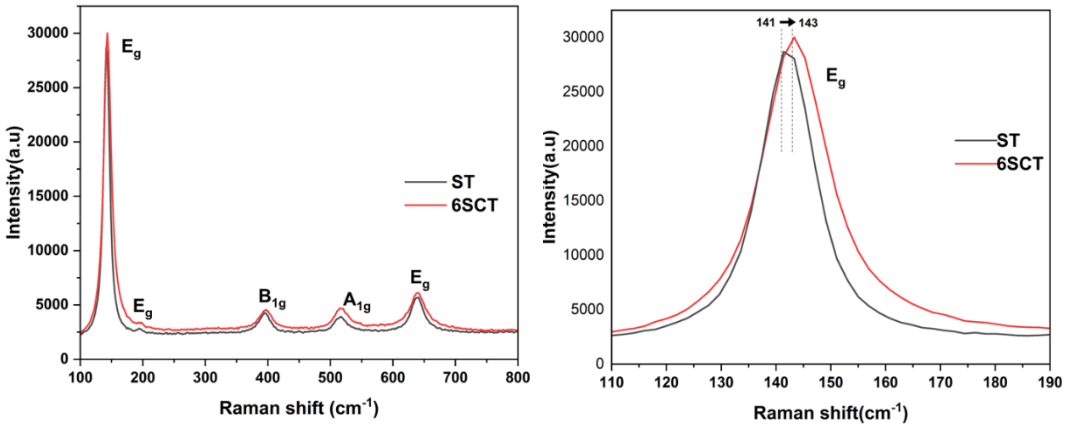

Figure 4.4. Raman spectra of untreated and HCl treated titania

For both samples, four Raman active modes were observed, viz, $E_g(141cm^{-1})$, $B_{1g}(394cm^{-1})$, $A_{1g}(514cm^{-1})$ and $E_g(638cm^{-1})$. The E_g, B_{1g}, and A_{1g} modes correspond to the symmetric stretching, symmetric bending, and asymmetric bending vibration of O-Ti-O respectively [92]. These modes suggest that both samples comprise of anatase phase of titania[122], which is in agreement with our XRD results. From the locally amplified Raman pattern, it can be observed that for the HCl treated TiO_2, the dominant peak of E_g at $141cm^{-1}$ displays blueshift and slight broadening in comparison with untreated TiO_2. This phenomenon is associated with decreased

crystallinity and the formation of oxygen vacancies. Due to the removal of lattice oxygen, the bond length of Ti-O shortens, resulting in the shift of E_g peak towards a higher wavenumber [123–126]. Thus, these results demonstrate that HCl addition during sol-gel synthesis leads to structural distortion and formation of oxygen vacancies.

4.4 Nitrogen Physisorption

The textural properties of synthesized titania particles were investigated with N_2-physisorption experiments. The average pore volume and average pore width were determined by the BJH desorption branch and the surface area was determined by the BET method. The results are tabulated below:

Table 4.2 Textural properties of synthesized titania samples

Samples	*BET surface area, m^2/g*	*Pore volume, cm^3/g*	*Pore width, nm*
ST	38.9	0.11	7.6
6SCT	47.7	0.18	12.3
8SCT	35.6	0.13	10.4
10SCT	27.1	0.13	14.1

As seen in Table 4.2, the BET surface area for ST titania sample is 38.9m^2/g. The addition of 6mL, 1M HCl during sol-gel synthesis resulted in an increase of the surface area. Surprisingly, a decreasing trend of BET surface area was observed upon increasing the volume of HCl during sol-gel synthesis.

N_2 adsorption-desorption isotherms for ST and 6SCT samples are shown in Figure 4.5 and Figure 4.6 respectively. N_2 adsorption-desorption isotherms for samples 8SCT and 10SCT are given in Figure D.6 and Figure D.7 respectively. Titania samples exhibit type IV isotherm according to IUPAC classifications which is a representative of mesoporous materials. The samples display two hysteresis steps which indicate the presence of bimodal porous structure[127–129]. For 6SCT, 8SCT and 10SCT samples, the first hysteresis can be regared as H1-type hysteresis in the relative pressure (P/P_0) between 0.45-0.9. This type of hysteresis is typically observed for porous materials consisting of agglomerates. For sample ST, the first hysteresis can be regarded as H2-type which indicates the presence of ink bottle pores. On the other hand, the second hysteresis for all samples could be classified as

H3-type hysteresis in the relative pressure(P/P_0) between 0.9-1 ranges which can be due to the capillary condensation of N_2 in the macropores of titania[130–134]. This type of hysteresis is typically observed in materials that have aggregates of plate like-particles yielding slit-type porous structures [130].

The presence of bimodal and unimodal porous structure for titania samples as predicted from the N_2 adsorption-desorption isotherms can also be confirmed by the BJH pore size distribution calculated from the desorption branch of the N_2 isotherm. From BJH desorption plots, samples ST, 6SCT, 8SCT, and 10SCT contain mesopores around 3.7, 11.4, 7.7 and 8.7nm respectively. Accordingly, the macropores for ST, 6SCT, 8SCT, and 10SCT samples are around 65.0, 63.7, 61.3 and 62.7nm respectively.

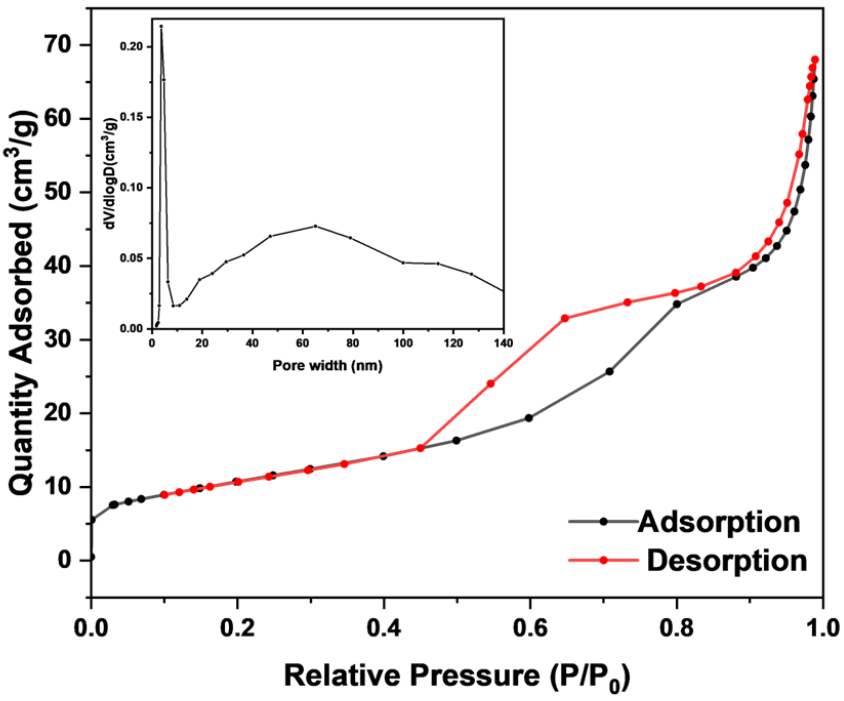

Figure 4.5. N_2 adsorption-desorption isotherm and BJH plot(inset) of ST sample

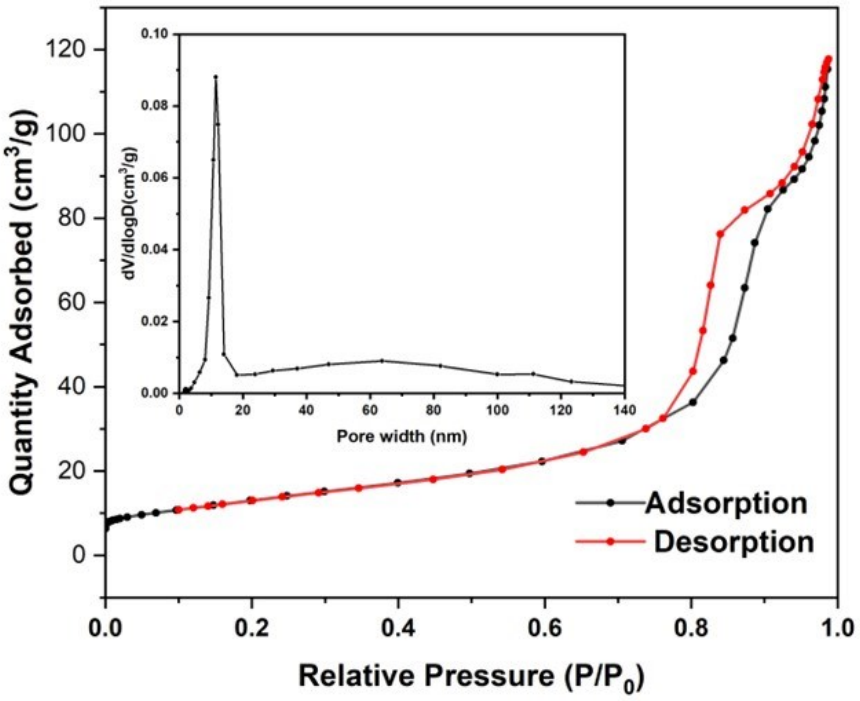

Figure 4.6. N_2 adsorption-desorption isotherm and BJH plot(inset) of 6SCT sample

4.5 Surface Morphology and Elemental Analysis

4.5.1 Surface Morphology

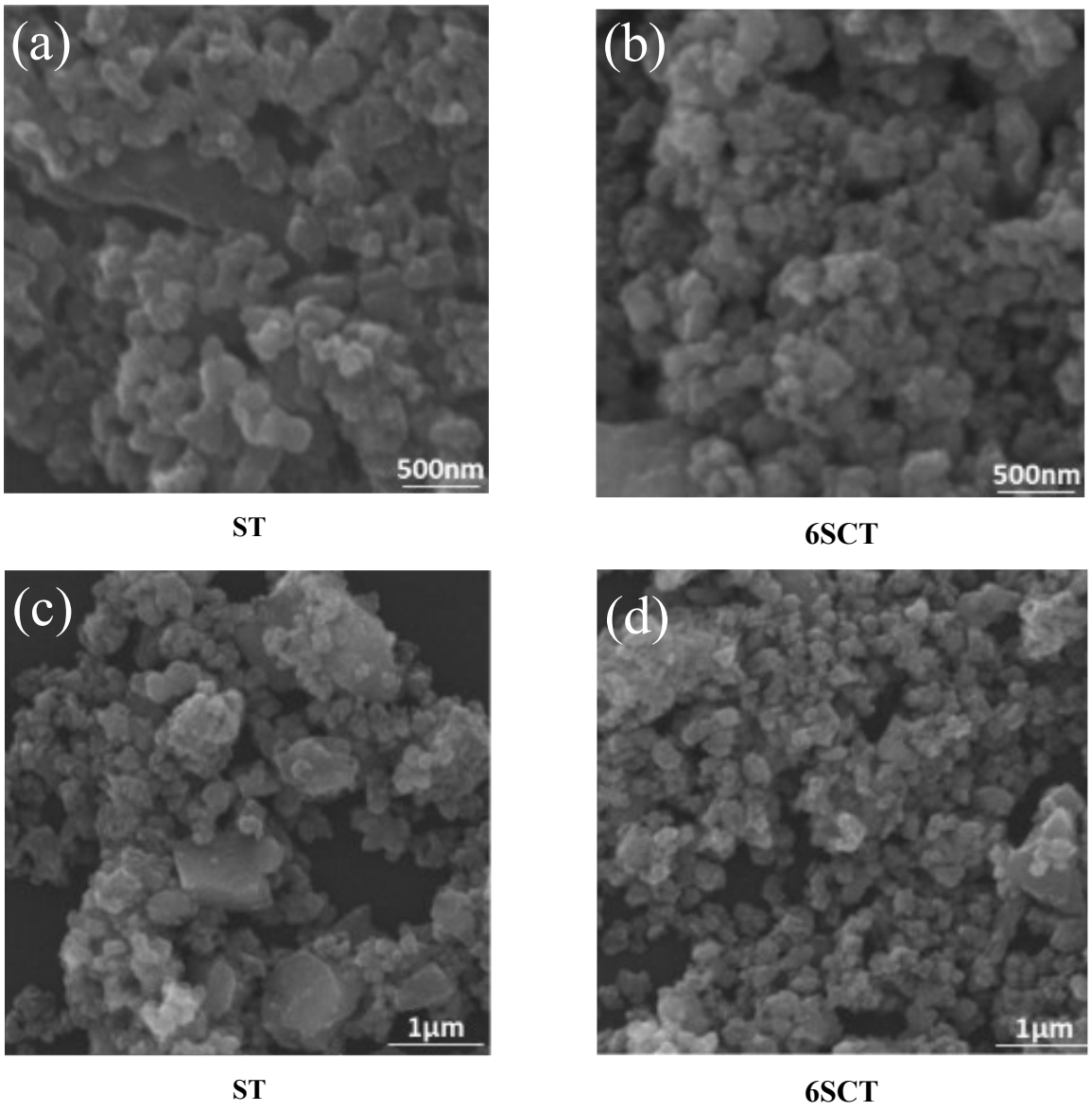

Figure 4.7. SEM images of synthesized titania samples; (a) and (c): ST titania at 500nm and 1µm scale respectively; (b) and (d): 6SCT titania at 500nm and 1µm scale respectively

The particle morphology of TiO_2 particles was analyzed with scanning electron microscopy (SEM). As seen in Figure 4.7, both ST and 6SCT titania samples have irregular morphology. Titania particles are observed in agglomerate form with irregular geometry. This agglomeration is due to the adhesion between titania nanoparticles. Titania samples in which HCl was added during the sol-gel synthesis(6SCT) showed slightly less agglomeration and higher dispersion of titania particles in comparison with ST titania. SEM images also reveal the presence of non-uniform holes between particles which give rise to the interparticle porosity. This would allow the easy removal of the products during a non-oxidative propane dehydrogenation reaction; thus, a high selectivity could be achieved.

4.5.2 Elemental Analysis

Elemental analysis of the synthesized samples was investigated with Energy Dispersive X-ray (EDX) spectroscopy. The EDX map and the imaging region used for elemental mapping for 6SCT and ST titania samples are shown in Figure 4.8 and Figure 4.9 respectively. For both samples, EDX signals associated with carbon(C), oxygen(O), gold (Au), palladium (Pd), and titanium (Ti) were detected. Before EDX-SEM analysis, samples were coated with a mixture of Au and Pd to avoid charging the surface. Thus, the Au and Pd signals are due to the coating of the samples with the Au-Pd mixture. The carbon signal is associated with the adhesive tape used during EDX-SEM analysis. Therefore, based on these results, the propane dehydrogenation activity could be solely based on titania material. The difference in the activity performance could be associated with the difference in the lattice structure between the two samples as discussed in sections 3.2.3, 3.2.4, 3.2.6, 3.2.7 and 3.2.8.

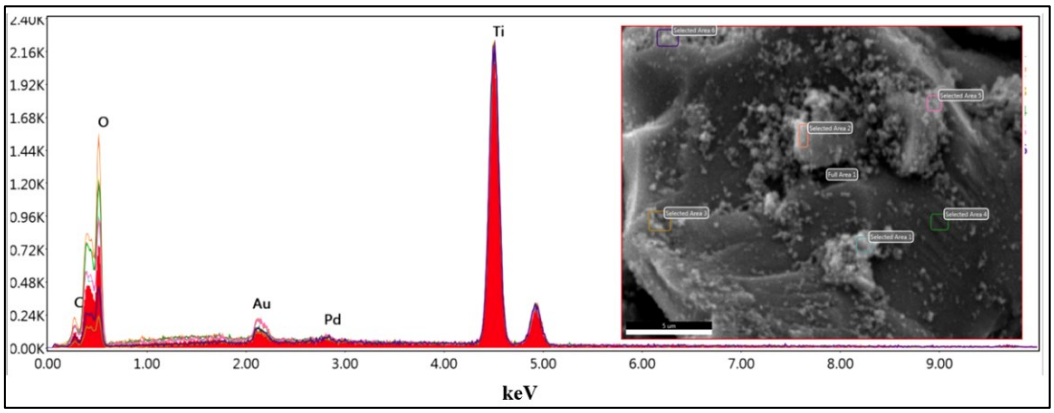

Figure 4.8. Energy dispersive X-ray elemental mapping of 6SCT titania

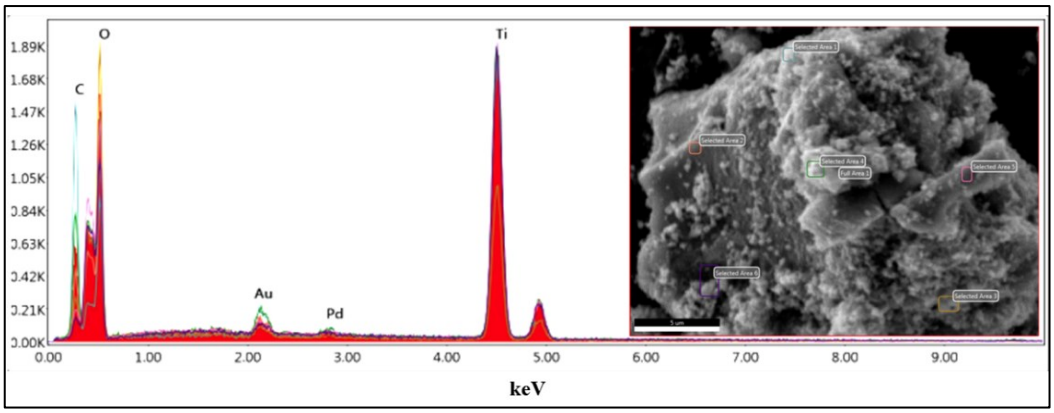

Figure 4.9. Energy dispersive X-ray elemental mapping of ST titania

4.6 X-ray Photoelectron Spectroscopy (XPS)

X-ray photoelectron spectroscopy (XPS) was carried out to investigate the surface chemical properties of the synthesized titania particles(ST and 6SCT) and the post-reaction 6SCT sample. The peaks related to Ti, O, and C were detected. The peak at 283eV is due to the C1s region which was used as a reference line for XPS analysis. The peaks related to Ti were observed at 463 and 458.63eV which are characteristic peaks of Ti $2p_{1/2}$ and Ti $2p_{3/2}$ respectively[72,135]. All samples exhibited a peak centered at 528.5eV which is associated with the lattice oxygen present in titania lattice. However, for the 6SCT sample, a shoulder peak at 530.1eV is also observed which could be attributed to the oxygen vacancies or surface hydroxyl species [73,136]. Since HCl was also added during the sol-gel synthesis for the 6SCT titania sample, a partial XPS scan for Cl 2p was also performed for all samples. As can be seen in Figure 4.10, no signals related to Cl were observed. Thus, the difference in the activity can be solely related to the difference in the structure of titania samples. The higher performance of the 6SCT sample could be attributed to the higher concentration of oxygen vacancies in comparison with the ST titania sample as seen from XPS plots. 6SCT sample was also characterized after 12h non-oxidative propane dehydrogenation activity (6SCT-PDH). As can be seen in Figure 4.10, the oxygen vacancy signal at 530.1eV is diminished after 15h non-oxidative propane dehydrogenation activity. As discussed later in section 4.11, the non-oxidative propane dehydrogenation activity over titania suffers a deactivation with time on stream due to coke deposition. Thus, the weakening of oxygen vacancy peak at 530.1eV after non-oxidative propane dehydrogenation reaction could be ascribed to the coke deposition over oxygen vacant sites.

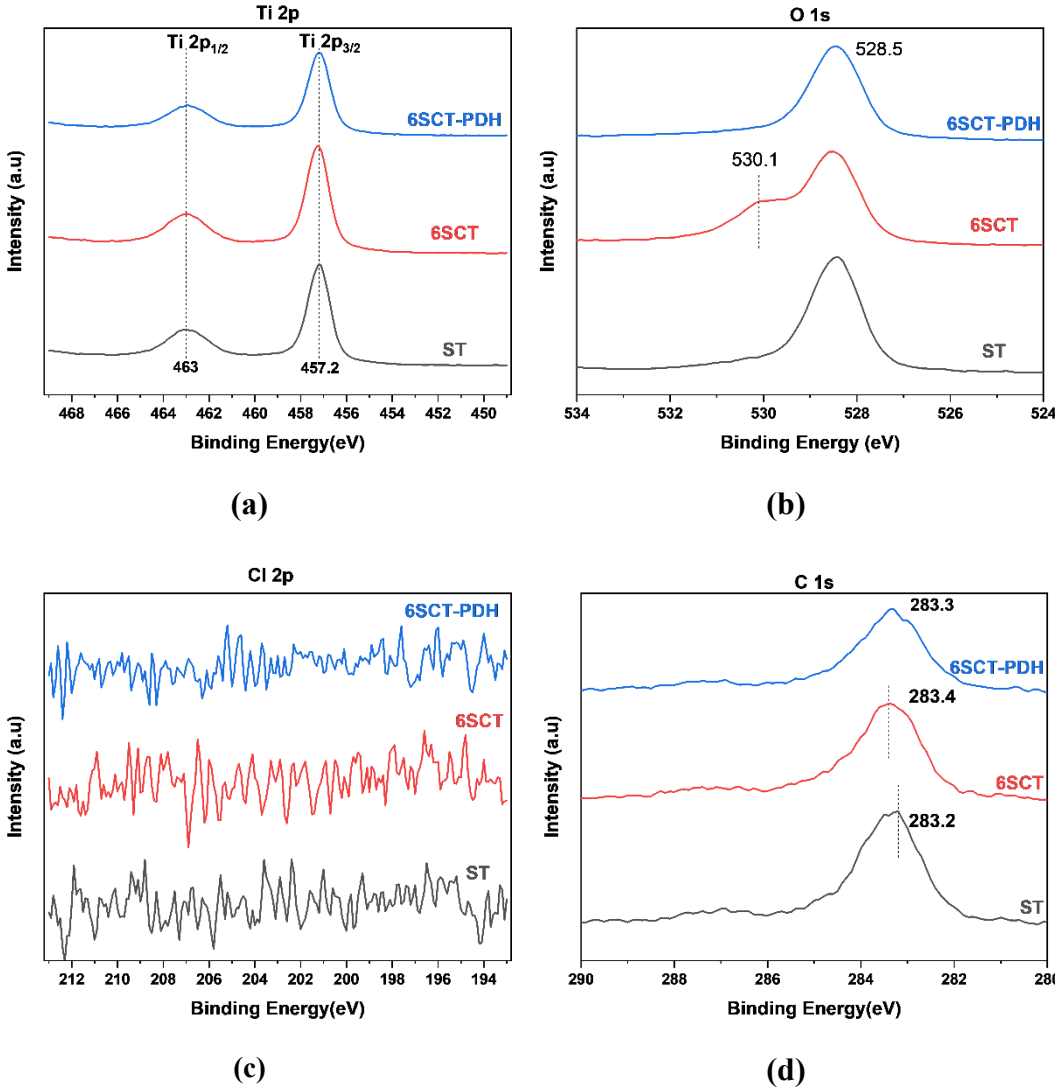

Figure 4.10. XPS partial scan: (a) Ti 2p (b) O 1s (c) Cl 2p and (d) C 1s

4.7 UV-Visible Diffused Reflectance Spectroscopy (DRS)

UV-Visible DRS was performed for ST and 6SCT titania catalysts to understand the formation of oxygen vacancies during reductive treatment.

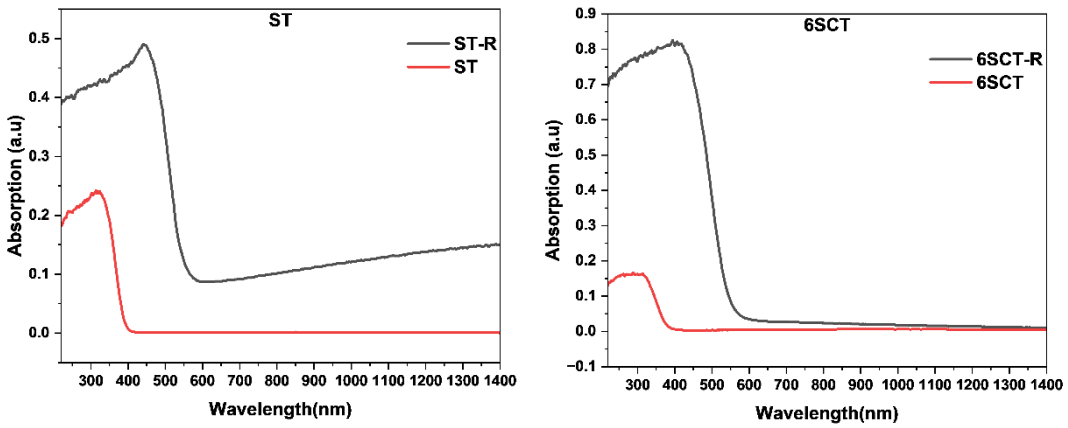

Figure 4.11. UV-Visible absorption spectra of fresh (ST and 6SCT) and H_2 reduced (ST-R and 6SCT-R). Reducing conditions: 30sccm pure H_2 flow for 1h at 500°C

Figure 4.11 reveals a red-shift in the absorption edge for both ST and 6SCT titania after reducing under the H_2 atmosphere. A higher light absorbance is also observed for hydrogen-treated samples in comparison with untreated samples. However, the 6SCT titania sample reduced under the H_2 environment possessed a higher light absorbance in comparison with H_2 reduced ST sample.

The change in absorption edge and increased absorbance could be attributed to the formation of oxygen vacancies. Since the defects (oxygen vacancies) are color centers [63], the formation of oxygen vacancies during H_2 reductive treatment causes the color change of titania from white to gray. This results in a higher absorbance of

light. The underlying phenomena behind this change are that the energy levels above the valence band undergo several transitions during the creation of oxygen vacancies by reductive treatment. These transitions subsequently cause absorption in the visible range[97].

The difference in the absorbance between ST and 6SCT titania catalyst is reflected in the non-oxidative propane dehydrogenation activity. Based on the prior discussion, the H_2-reduced 6SCT titania sample exhibited higher absorbance in comparison with H_2-reduced ST titania. This indicates the relative ease of the formation of oxygen vacancies over 6SCT in comparison with ST. Since the active sites over titania are coordinatively unsaturated Ti^{4+} cations with neighboring oxygen vacancies, 6SCT titania exhibited a higher propane dehydrogenation activity in comparison with ST titania.

4.8 In-situ DRIFTS of Adsorbed Pyridine

In catalysis, the surface acidic properties of metal oxide largely depend on the synthesis conditions and the post-treatment. The acidic sites are mainly Bronsted and Lewis acid centers which are typically defined as proton donors (H^+) and electron-pair acceptors respectively. Over metal oxides, the Bronsted acid centers could be -OH functional groups or water molecules adsorbed on the surface. These groups serve as the active centers for the adsorption of molecules via -H bonds. On the other hand, Lewis acidic centers over metal oxides comprise coordinatively unsaturated cations which can form coordination bonds with molecules having electron-dense regions[137].

As discussed in section 2.6.1, the active centers for propane dehydrogenation over bulk metal oxides are widely accepted as coordinatively unsaturated cations with neighboring oxygen vacancies. In the case of titania, which possesses both Lewis and Bronsted acidic characteristics[138], the active sites comprise fourfold-coordinated titanium atoms with neighboring oxygen vacancies [98]. Diffuse Reflectance Infrared Fourier Transform Spectroscopy (DRIFTS) of adsorbed pyridine (C_5H_5N) is an effective technique to distinguish between Bronsted and Lewis acidic sites over titania [103,104]. Being a weak base, pyridine adsorbs on Lewis acid sites by creating a coordination bond with coordinatively unsaturated Ti^{n+} sites. On the other hand, pyridine adsorbs on Bronsted acidic sites by forming Pyridinium ion (PyH^+). The adsorption of pyridine over different acidic sites is reflected on the IR spectrum[139].

In our case, Pyridine FTIR was carried out to determine the surface acidity of ST and 6SCT titania. Before the measurement, the sample was purged with Argon to ensure the removal of physically adsorbed water or any other surface impurities. Hydrogen pretreatment at 500°C was also carried out for the creation of coordinatively

unsaturated sites with the removal of lattice oxygen. Thereafter, pyridine was adsorbed at 50°C and the IR spectrum recorded at 50, 150, 250, 350, and 450°C is given in Figure 4.12. The active modes observed in the spectrum correspond to the ring vibrations of adsorbed pyridine. The band at 1443, 1489, 1574 and 1600cm^{-1} are associated with ν_{19b}, ν_{19a}, ν_{8b} and ν_{8a} ring vibrations of pyridine respectively [140,141].

Table 4.3 Peak assignments for adsorbed pyridine

Ring Vibrations	*Peak positions*	*Peak Assignment*
19b	1443	H-bonded pyridine
19a	1489	Pyridine bonded to Lewis site
8b	1574	Chemisorbed Pyridine
8a	1600	Pyridine bonded to Lewis acid sites

For both samples(ST and 6SCT), the IR active modes reveal that pyridine is chemisorbed, hydrogen-bonded, and adsorbed on Lewis acidic sites on the titania surface. No vibrational bands associated with physisorbed pyridine and pyridine bonded to Bronsted sites were detected for both samples.

The pyrdine-drifts results further confirms that the non-oxidative propane dehydrogenation activity is associated with the Lewis sites (coordinatively unsaturated Ti with neighboring oxygen vacancies). The higher activity performance of 6SCT can be attributed to the higher concentration of Lewis acidic sites in comparison with ST titania sample.

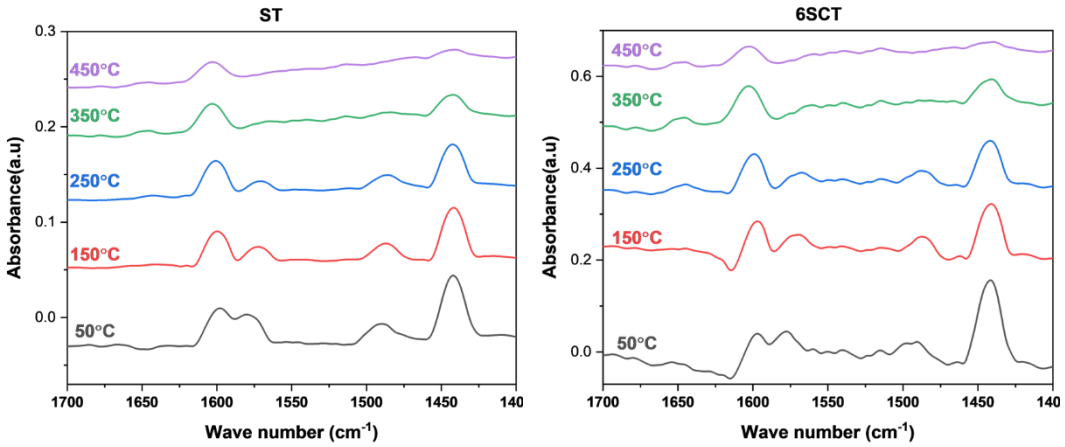

Figure 4.12. Pyridine FTIR spectra for ST and 6SCT titania

4.9 Temperature Programmed Reduction(TPR)

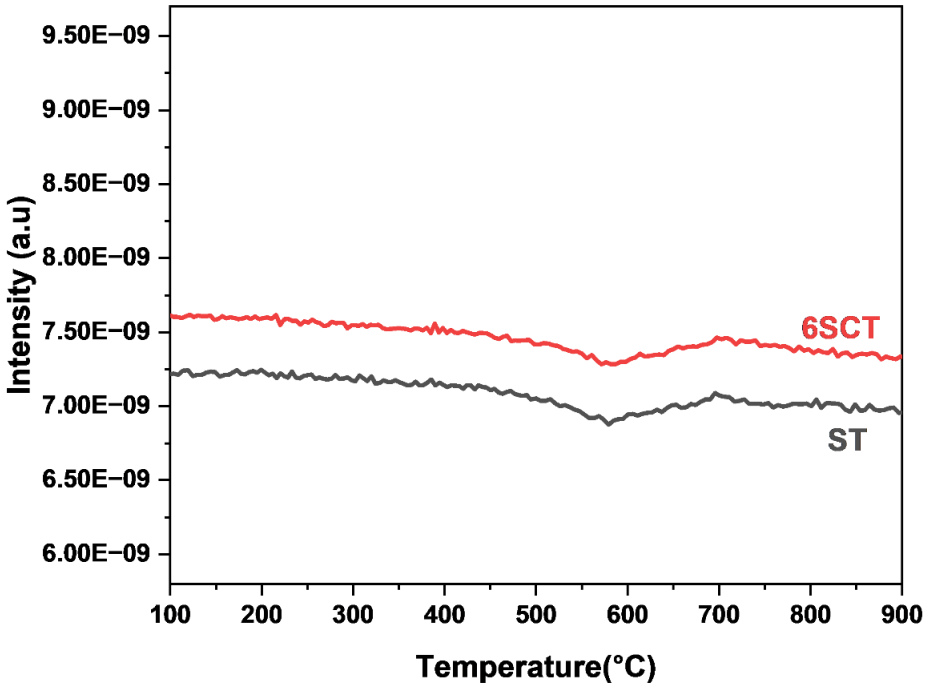

Figure 4.13. H_2-TPR profiles of ST and 6SCT titania

The redox properties of synthesized titania samples were characterized by H_2-TPR (Figure 4.13) and CO-TPR (Figure 4.16). As depicted in Figure 4.13, both titania samples possess weak H_2 consumption around 600°C. This consumption is associated with the interaction of H_2 with the lattice oxygen to yield water[142–144]. The H_2 consumption and its associated water formation peak are plotted in Figure 4.14 and Figure 4.15 for 6SCT and ST titania samples respectively.

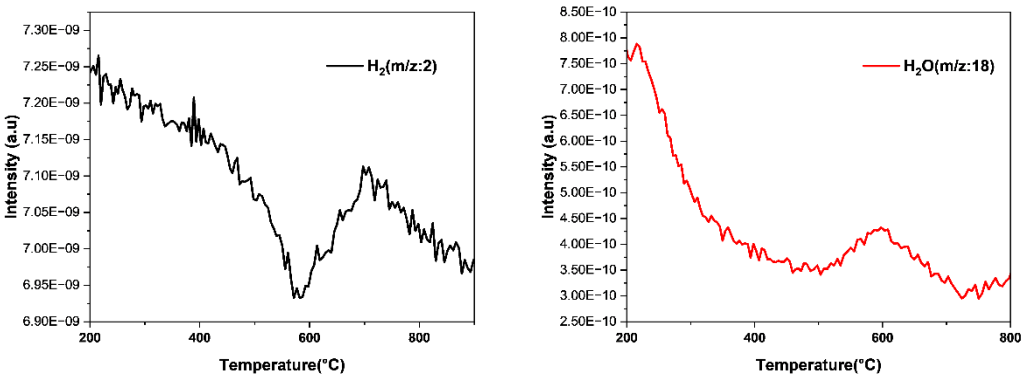

Figure 4.14. H_2 consumption and H_2O formation profiles as a function of temperature for the 6SCT sample

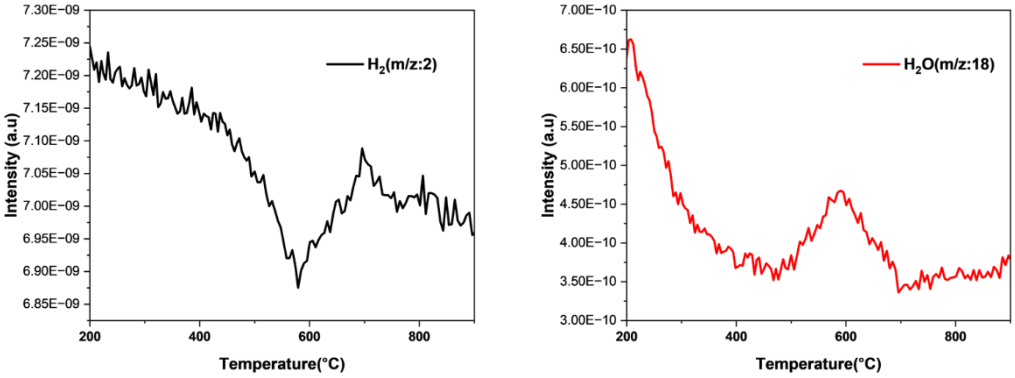

Figure 4.15. H_2 consumption and H_2O formation profiles as a function of temperature for ST sample

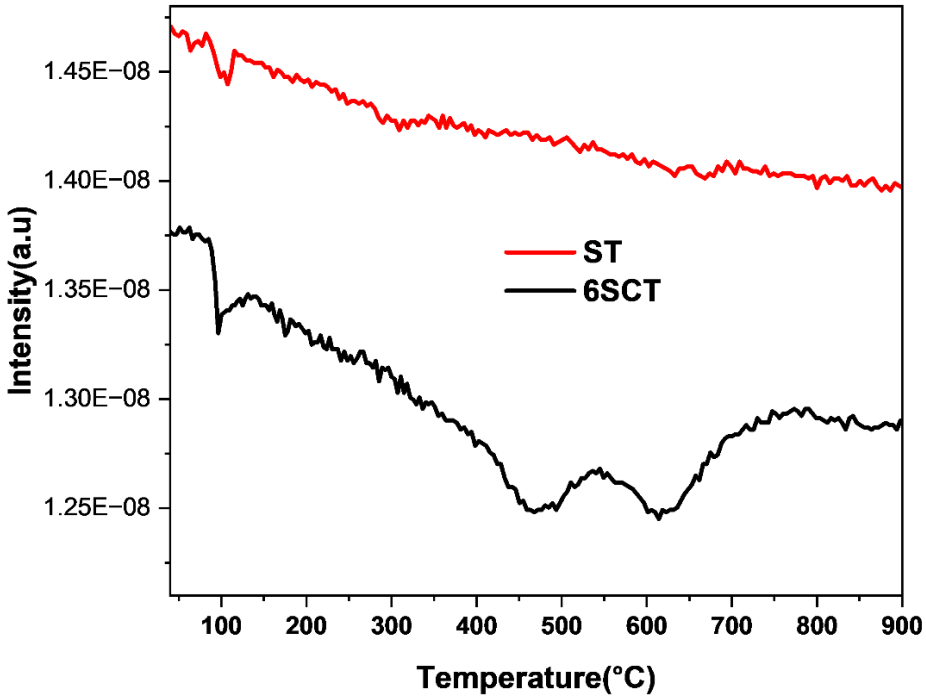

Figure 4.16. CO-TPR profiles of ST and 6SCT titania

Redox properties of titania samples were also investigated by CO-TPR. When used as a probe molecule, CO interacts with the lattice oxygen to yield CO_2. As depicted in Figure 4.16, two CO consumption signals are observed for the 6SCT sample which indicates the interaction of CO with different types of lattice oxygen in the 6SCT titania sample[145]. Another possibility of multiple CO consumption could be associated with the interaction of CO with specific sites over 6SCT catalyst to yield carbide and carbondioxide($2CO \rightarrow C + CO_2$). However, to verify this reasoning, characterization of post CO-TPR sample with techniques such as TGA or TPO are required. In comparison with 6SCT titania, the ST sample shows very low consumption of CO which is identified by a weak CO_2 formation signal around 600°C with a shoulder around 500°C. The CO consumption and its associated CO_2 formation peak are plotted in Figure 4.17 and Figure 4.18 for ST and 6SCT titania samples respectively.

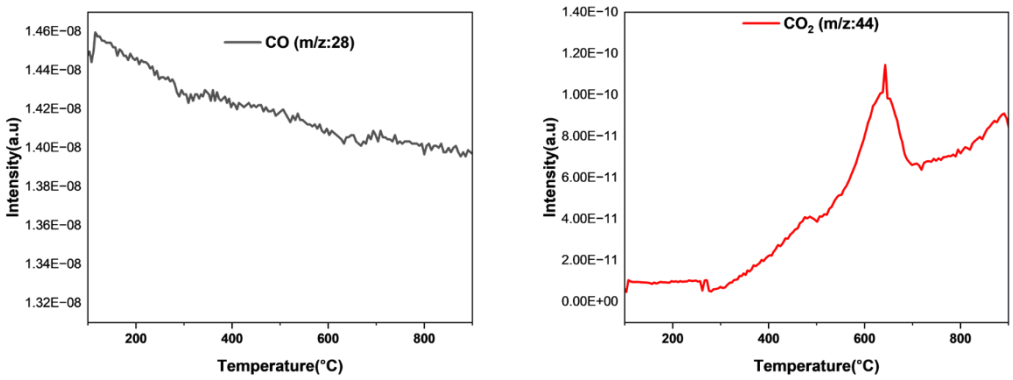

Figure 4.17. CO consumption and CO_2 formation profiles as a function of temperature for ST sample

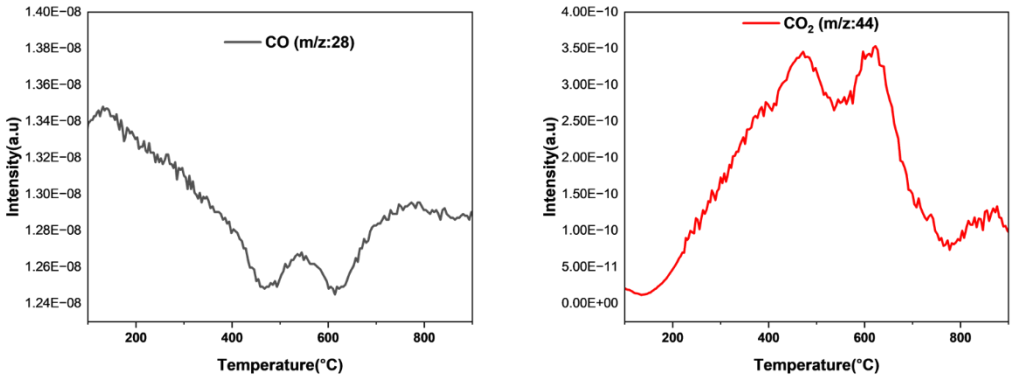

Figure 4.18. CO consumption and CO_2 formation profiles as a function of temperature for the 6SCT sample

4.10 Temperature Programmed Surface Reaction(TPSR)

Temperature programmed surface reaction (TPSR) was performed to investigate the in-situ reduction of titania during non-oxidative propane dehydrogenation. Since the sample was purged with Ar at 600°C, the contribution of physically or chemically adsorbed oxygen and water species to the mass spectrometer signal during the in-situ reduction is minimized.

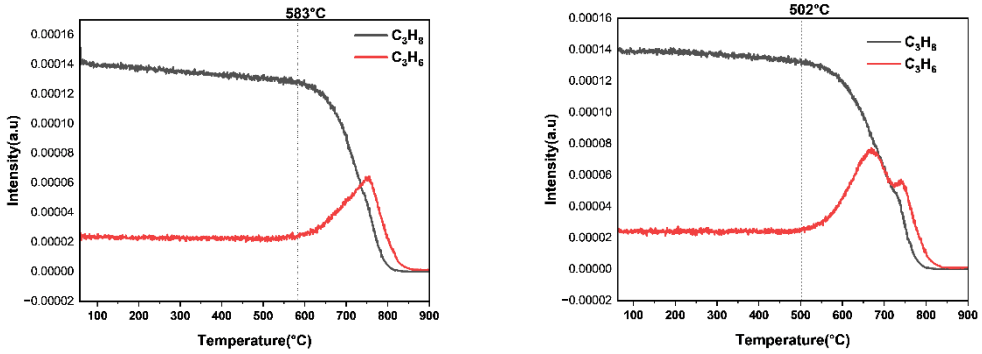

(a) **(b)**

Figure 4.19. Profiles of C_3H_8(m/z: 43) and C_3H_6 (m/z: 42) during C_3H_8-TPSR over (a) ST and (b) 6SCT

The profiles of C_3H_8(m/z: 43) and C_3H_6 (m/z: 42) during C_3H_8-TPSR are given in Figure 4.19. The C-H activation temperature could be predicted from the temperature where the C_3H_8 consumption begins. The C-H activation temperature over ST titania is around 583°C which is 81°C higher than the 6SCT sample. The results are in agreement with the high propane dehydrogenation activity observed over the 6SCT sample in comparison with the ST titania sample. This indicates the influence of HCl addition during the sol-gel synthesis of titania particles on the formation of oxygen vacancies.

4.11 Non-oxidative propane dehydrogenation activity

4.11.1 Finding the best performing titania catalyst for non-oxidative propane dehydrogenation

The non-oxidative propane dehydrogenation activity over bulk metal oxides such as zirconia and titania is widely accepted to be related to the concentration of coordinatively unsaturated cations located near oxygen vacancies[23]. Based on this literature fact, we aimed to synthesize non-noble and non-toxic titania with tunable oxygen vacancies. The oxygen vacancies over titania were modified by varying the volume of 1M HCl added during the sol-gel synthesis of titania particles. 5 different titania samples were synthesized by the addition of 0, 2, 6, 8, and 10mL of 1M HCl during the sol-gel synthesis. These titania samples were tested for non-oxidative propane dehydrogenation activity. Propane conversion and propene selectivity against time on stream at 550°C over these particles are given in Figure 4.20(a) and Figure 4.20(b) respectively. It can be seen that all titania samples which were synthesized by the addition of HCl during sol-gel synthesis exhibit higher propane conversion and propene selectivity in comparison with ST titania.

(a) (b)

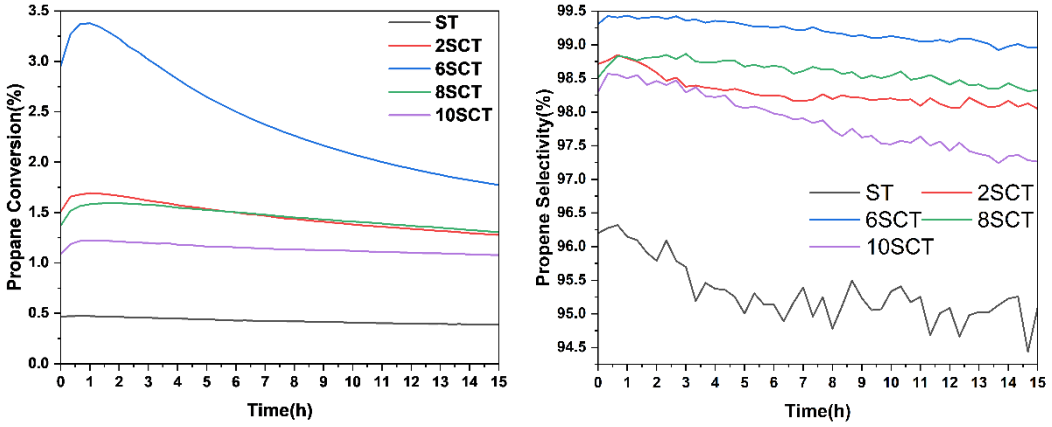

Figure 4.20. Non-oxidative propane dehydrogenation over different titania samples: (a) Propane conversion, (b) Propene selectivity; Test conditions: Temperature:550°C, Pressure:1bar, Catalyst mass: 150mg titania + 50mg Davisil 646 silica, 30sccm C_3H_8:Ar=6.9:93.1

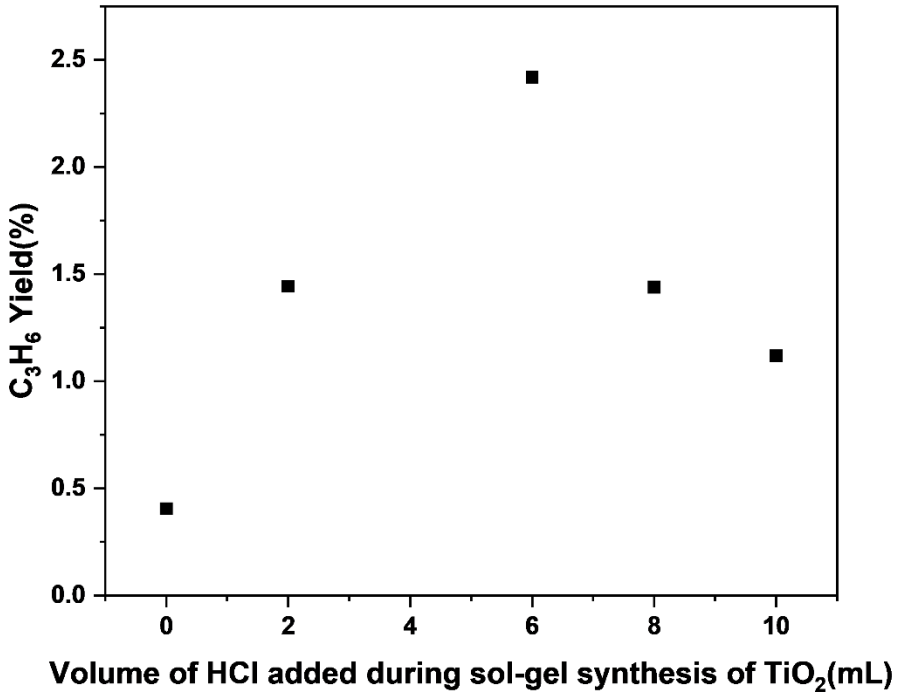

Figure 4.21. C_3H_6 yield (%) as a function of HCl volume(mL) added during sol-gel synthesis of TiO_2 particles. Test conditions: Temperature:550°C, Pressure:1bar, Catalyst mass: 150mg titania + 50mg Davisil 646 silica, 30sccm C_3H_8:Ar=6.9:93.1

The effect of the addition of a different volume of HCl during the sol-gel synthesis of titania towards propene yield in non-oxidative propane dehydrogenation can be more clearly observed in Figure 4.21. It can be seen that the yield to propene passed over a maximum over titania particles synthesized by the addition of 6mL of 1M HCl during the sol-gel synthesis. The addition of lower or higher than 6mL of 1M HCl poorly affects the yield of propene during non-oxidative propane dehydrogenation.

Other products formed during the non-oxidative propane dehydrogenation activity tests include methane, ethane and ethene as depicted in Figure B.5. However, the selectivity towards these products is only 0.27, 0.61 and 0.62% for methane, ethane and ethene respectively. In comparison, the selectivity towards propene is 99.3%

which is significantly higher than other products. Thus, the synthesized catalyst is highly selective towards propene.

4.11.2 Effect of pretreatment conditions in non-oxidative propane dehydrogenation activity over titania

The active sites for propane dehydrogenation are coordinatively unsaturated metal cations located near oxygen vacancies. These sites are typically generated by pre-reducing the catalyst under CO or H_2 environment at reaction temperatures. In addition to CO or H_2 reduction, these sites could also be generated in-situ during propane dehydrogenation reaction. Based on these considerations, we aimed to investigate the effect of different pre-reduction conditions on propane dehydrogenation activity for best and worst-performing titania samples. In order to do that, we conducted propane dehydrogenation activity tests over unreduced (no pretreatment) catalysts and H_2 or CO-reduced catalysts. The plots of propane conversion and propene selectivity as a function of time on stream for the 6SCT and ST titania sample are given in Figure 4.22 and Figure 4.23. For the 6SCT titania sample, it was found that the propane conversion and propene selectivity were the highest for the unreduced sample followed by H_2 and CO reduced sample. This finding is in contrast with the ST sample where the unreduced sample showed the worst propane conversion and propene selectivity compared with H_2 and CO reduced titania samples.

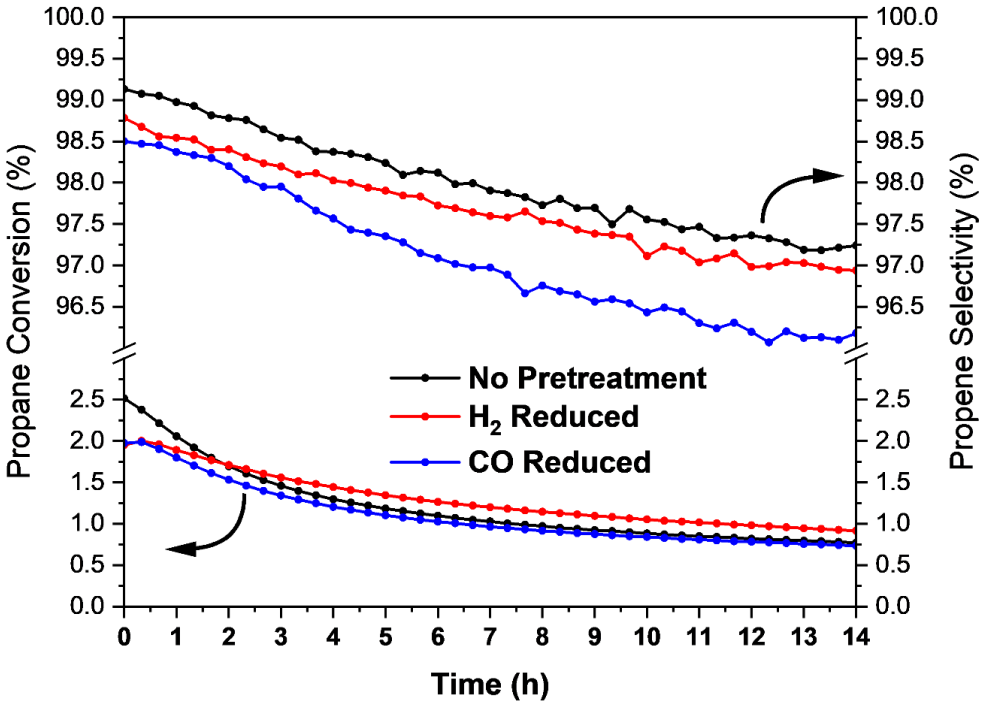

Figure 4.22. Propane conversion and propene selectivity as a function of time on stream for 6SCT titania. Test conditions: Temperature:550°C, Pressure:1bar, Catalyst mass: 200mg 6SCT titania, 30sccm C_3H_8:Ar=7:93

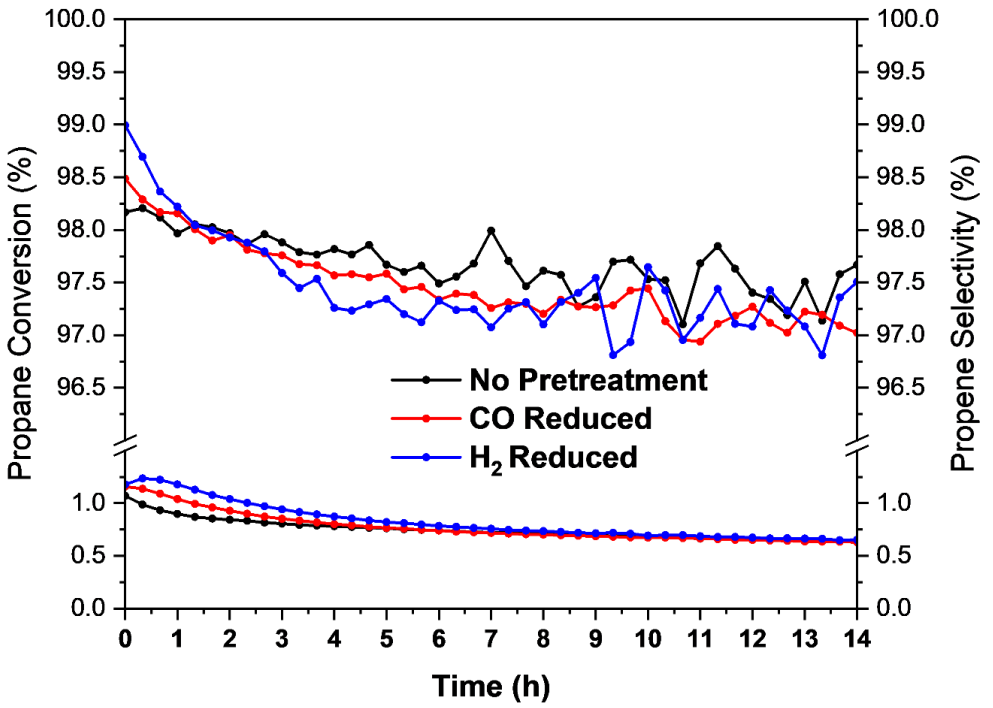

Figure 4.23. Propane conversion and propene selectivity as a function of time on stream for ST titania. Test conditions: Temperature:550°C, Pressure:1bar, Catalyst mass: 200mg ST titania, 30sccm C_3H_8:Ar=7:93

4.11.3 Effect of temperature on propane conversion and propene selectivity during non-oxidative propane dehydrogenation activity

According to the discussion in section 2.2, non-oxidative propane dehydrogenation is favored at high temperatures and low partial pressures of propane. The equilibrium propane conversion tends to increase as the temperature increases. However, at higher temperatures, the side reactions such as propane cracking and coke formation are also favored. Based on these considerations, we aimed to test the non-oxidative propane dehydrogenation activity at different temperatures.

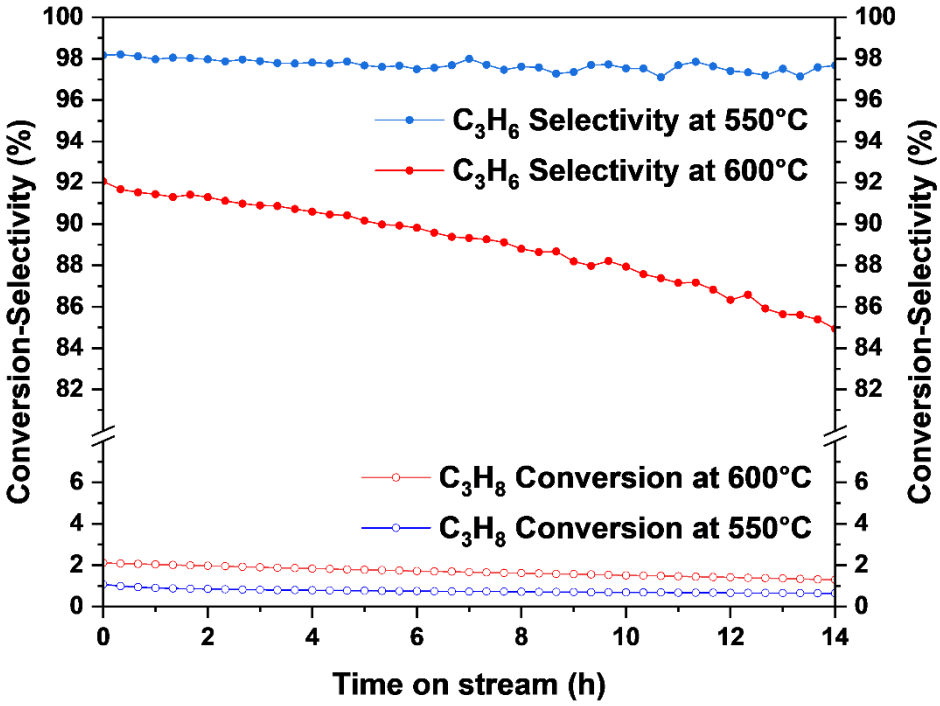

Figure 4.24. Propane conversion and propene selectivity as a function of time on stream for ST titania. Test conditions: Temperature:550°C or 600°C, Pressure:1bar, Catalyst mass: 200mg ST titania, 30sccm C_3H_8:Ar=7:93

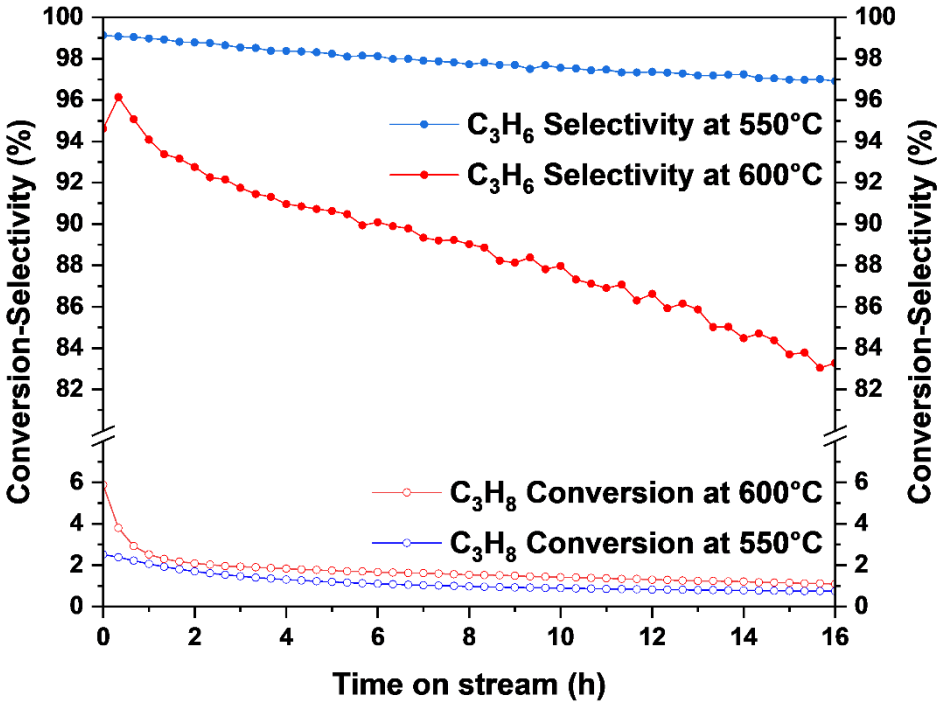

Figure 4.25. Propane conversion and propene selectivity as a function of time on stream for 6SCT titania. Test conditions: Temperature:550°C or 600°C, Pressure:1bar, Catalyst mass: 200mg 6SCT titania, 30sccm C_3H_8:Ar=7:93

Figure 4.24 and Figure 4.25 shows the conversion-selectivity plot as a function of time on stream(TOS) for ST and 6SCT titania catalysts respectively. It can be seen that both ST and 6SCT possess a high propane conversion and low propene selectivity at high temperatures (600°C) in comparison with low temperatures (550°C).

For our best-performing catalyst (6SCT), initial propane conversion increased from about 2% at 550°C to nearly 6% at 600°C. With time on stream, propane conversion was relatively stable at 550°C. However, at 600°C propane conversion decreased sharply from 6% to nearly 2% in approximately 2h of time on stream. Hereafter, propane conversion remained relatively stable with time on stream. On the other hand, the propene selectivity for 6SCT decreased from 99% to about 97% at 550°C

during 16h TOS. However, at 600°C the propene selectivity linearly decreased from 96% to about 83% during 16h TOS non-oxidative propane dehydrogenation activity.

For the ST titania sample, the initial propane conversion increased from 1% at 550°C to about 2% at 600°C. Surprisingly for both temperatures, relatively stable propane conversion was observed for 14h TOS. On the other hand, the propene selectivity decreased linearly from 92% to about 85% after 14h time on stream at 600°C. Surprisingly, the propene selectivity remained relatively stable at 550°C maintaining about 98% propene selectivity for 14h TOS.

Regardless of the decreasing propane conversion and propene selectivity with time on stream, we can see that the 6SCT titania sample exhibited nearly 3 times high initial propane conversion in comparison with the ST sample at high temperature (600°C). Also, the initial selectivity for propene is higher at high temperatures for 6SCT in comparison with ST. The results suggest that our synthesized 6SCT titania sample is highly selective for non-oxidative propane dehydrogenation in comparison with ST titania. This indicates that a high initial propane conversion and high propene selectivity could be obtained over 6SCT titania.

4.11.4 Long-term non-oxidative propane dehydrogenation activity test for the best performing catalyst

The relatively long-term non-oxidative propane dehydrogenation activity test was performed over the best-performing titania catalyst (6SCT) to investigate its industrial importance. It was aimed to see whether a high propene selectivity could be maintained at relatively higher propane conversions.

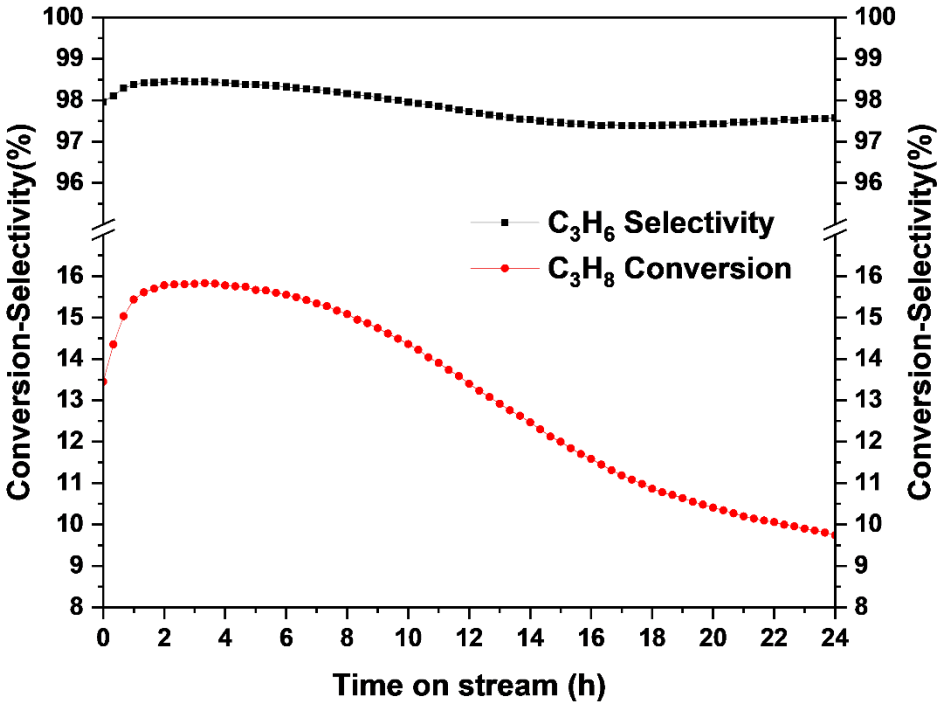

Figure 4.26. Propane conversion and propene selectivity as a function of time on stream for 6SCT titania. Test conditions: Temperature:550°C, Pressure:1bar, Catalyst mass: 1.8g 6SCT titania, 10sccm C_3H_8:Ar=7:93

As can be seen from Figure 4.26, the propane conversion increased from about 13% to about 15% in less than 1h time on stream and was relatively stable for 8h. Thereafter, the propane conversion gradually decreased to about 10% at the end of 24h propane dehydrogenation. On the other hand, selectivity to propene slightly

increased at the beginning of the reaction which was relatively stable throughout the activity period, reducing to only about 97.4% at the end of 24h propane dehydrogenation activity.

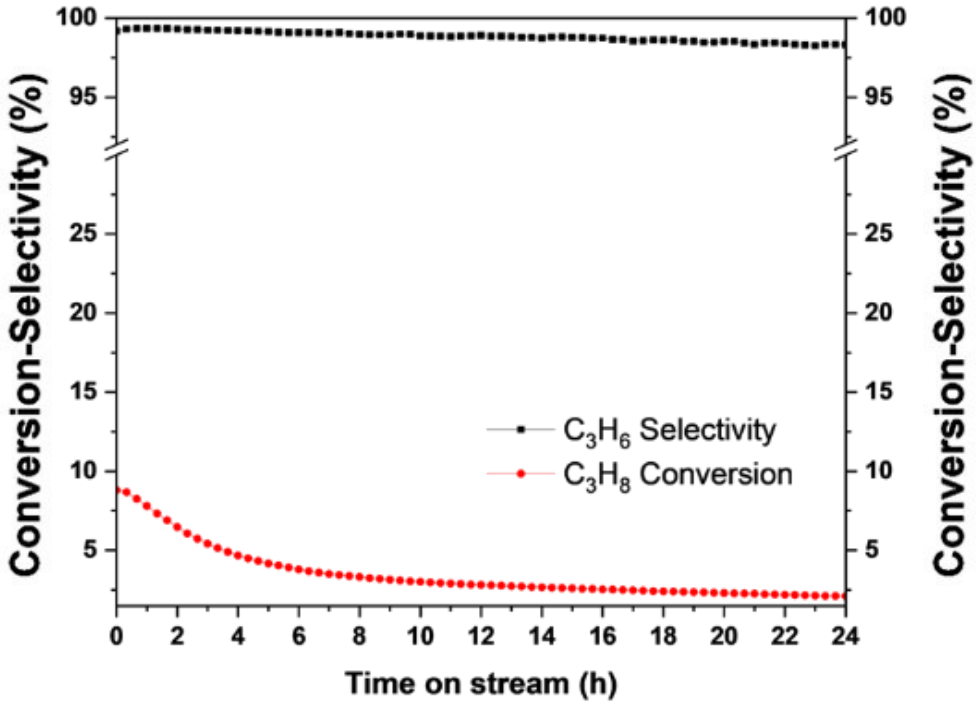

Figure 4.27. Propane conversion and propene selectivity as a function of time on stream for 6SCT titania. Test conditions: Temperature:550°C, Pressure:1bar, Catalyst mass: 0.903g 6SCT titania, 30sccm C_3H_8:Ar=7:93

Long-term non-oxidative propane dehydrogenation activity tests were also performed for different WHSV. Two different non-oxidative propane dehydrogenation activity tests were performed at 550°C using 30sccm and 5sccm 7vol % propane in Ar feed. For both tests, approximately 0.903g 6SCT titania catalyst was used.

It can be seen in Figure 4.27, that using 30sccm of 7vol% propane in Ar feed, an initial propane conversion of about 8% is achieved which decreased rapidly to about

4% in 5h time on stream. Hereafter, the propane conversion decreased relatively slowly to about 2.3% after 24h time on stream.

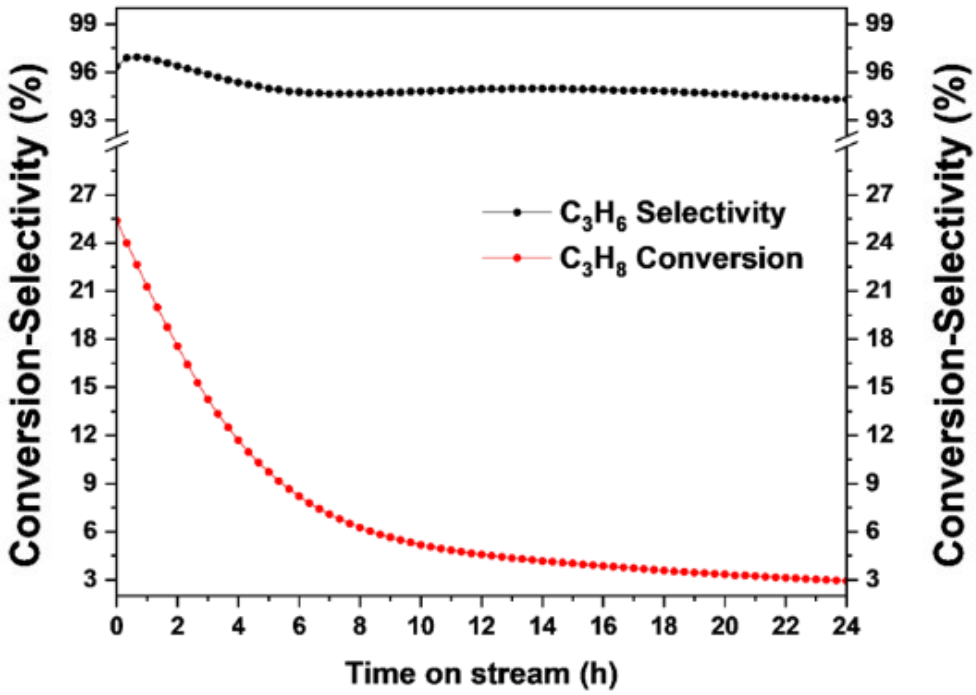

Figure 4.28. Propane conversion and propene selectivity as a function of time on stream for 6SCT titania. Test conditions: Temperature:550°C, Pressure:1bar, Catalyst mass: 0.903g 6SCT titania, 5sccm C_3H_8:Ar=7:93

Similar behavior is observed for non-oxidative propane dehydrogenation activity over 0.903g 6SCT titania catalyst using 5sccm 7vol% propane in Ar feed. As depicted in Figure 4.28, an initial propane conversion of about 25% is achieved with 96% propene selectivity. With 5h time on stream, propane conversion decreased rapidly to about 9%. Hereafter, propane conversion decreased relatively slowly to about 4% after 24h on stream. Surprisingly, during 24h time on stream, propene selectivity decreased from 96% in the beginning to only about 94% after 24h time on stream.

These results demonstrate the industrial importance of our best-performing 6SCT titania catalyst, indicating that a high propene selectivity could be maintained at relatively higher propane conversion

4.11.5 Effect of co-feeding H_2 and C_3H_8 on non-oxidative propane dehydrogenation activity

Based on the prior discussion, the non-oxidative propane dehydrogenation over titania (6SCT) undergoes a quick deactivation at high initial conversion experiments. This is mainly due to the coke deposition (propene intermediates) which covers the titania surface and prevents the exposure of active sites for non-oxidative propane dehydrogenation. Coke deposition could be minimized with H_2 co-feeding. H_2 can react with propene intermediates to yield propane and thus the coke depostion could be hindered [146]. Therefore, we aimed to co-feed hydrogen with propane during the non-oxidative propane dehydrogenation to attain on-stream stability. Conversion-selectivity plot with time on stream for 30sccm 7 vol% propane in Ar and 0.4sccm H_2 and 30sccm 7 vol% propane in Ar is given in Figure 4.29. The results show that co-feeding hydrogen negatively affects the conversion which decays relatively faster in comparison with H_2-free propane feed. The results are contrary to the findings of Otroshchenko et al. [146] where co-feeding hydrogen with propane improved the on-stream stability by removing the coke species through their hydrogenation.

However, our finding is still rudimentary to conclude any effect of co-feeding hydrogen on on-stream stability of propane dehydrogenation. For future experiments, we aim to test different compositions of hydrogen to see their effect on the long-term stability of non-oxidative propane dehydrogenation.

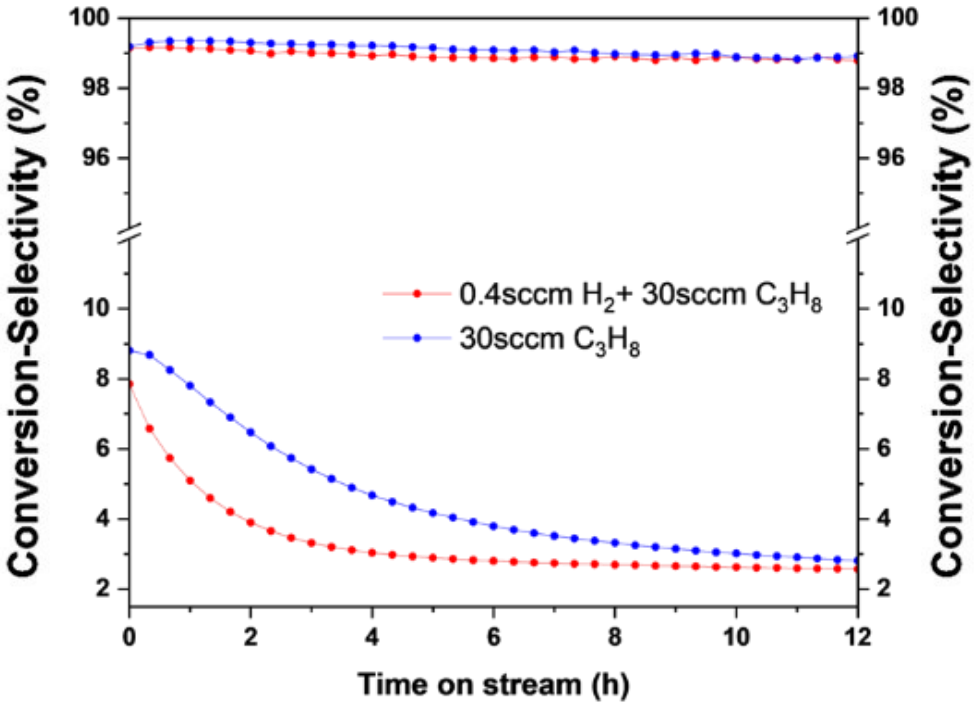

Figure 4.29. Propane conversion and propene selectivity as a function of time on stream for 6SCT titania. Test conditions: Temperature:550°C, Pressure:1bar, Catalyst mass: 0.903g 6SCT titania, Feed 30sccm C_3H_8:Ar=7:93 or 30sccm C_3H_8:Ar=7:93 + 0.4sccm H_2(pure)

CHAPTER 5

CONCLUSIONS

In this study, we have demonstrated the use of titania as an active material for propene production via non-oxidative propane dehydrogenation. Unlike conventional non-oxidative propane dehydrogenation catalysts (Pt or Cr_2O_3), the active sites over bulk titania comprises surface defects. Taking into consideration the aforementioned fact, we postulated a novel sol-gel method of synthesizing non-toxic, non-noble, and dopant-free titania with tunable oxygen vacancies (defects) for non-oxidative propane dehydrogenation. The oxygen vacancies over titania were tuned during the in-situ synthesis of titania by varying the volume (0,2,6,8 and 10mL) of 1M HCl. Synthesized catalysts were characterized by nitrogen physisorption, X-ray diffraction (XRD), Raman spectroscopy, H_2 or CO-TPR, UV-Visible spectroscopy, Pyridine in-situ drift, X-ray photoelectron spectroscopy (XPS), Thermal Gravimetric Analysis (TGA) and tested for non-oxidative propane dehydrogenation activity. The findings are listed as follows:

- TGA results showed excellent thermal stability of synthesized titania catalysts. No mass loss was observed above 500°C. This indicates that our synthesized titania catalysts are thermally stable in the operating conditions(500-700°C) of non-oxidative propane dehydrogenation.
- X-ray diffraction results revealed that all synthesized titania catalysts calcined at 500°C for 1h under static air exhibited only patterns of pure anatase titania. However, catalysts synthesized with the addition of a different volume of 1M HCl display different crystallite sizes as determined with the Scherrer equation.
- Raman spectroscopy revealed $E_g(141cm^{-1})$, $B_{1g}(394cm^{-1})$, $A_{1g}(514cm^{-1})$ and $E_g(638cm^{-1})$ modes for both ST and 6SCT titania samples. These modes are

characteristics of the anatase phase of titania. However, the 6SCT sample displayed a blue shift for Eg mode at 143cm^{-1} in comparison with ST which displayed Eg mode at 141cm^{-1}. This shift can be attributed to the incorporation of oxygen vacancies over 6SCT in comparison with ST titania.

- N_2 physisorption results revealed that all synthesized samples were mesoporous with type IV IUPAC isotherm. BET surface area was found to increase with the addition of 1M HCl up to 6mL. Thereafter, the addition of HCl resulted in a decrease in BET surface area. Titania samples synthesized with the addition of HCl during sol-gel synthesis displayed multi-modal porous structure as evident from BJH pore size distribution and multiple hysteresis steps in adsorption-desorption isotherm.
- Scanning electron microscopy(SEM) analysis showed random morphology of titania particles for all synthesized samples. Titania particles were observed in agglomerated form with irregular morphology.
- Electron dispersive X-ray(EDX) spectroscopy revealed the presence of Ti and O atoms for all synthesized samples. This indicates that the propane dehydrogenation activity is solely based on titania.
- X-ray photoelectron spectroscopy (XPS) results displayed signals associated with Ti $2p_{1/2}$, Ti$2p_{3/2}$, O1s, and C1s for fresh ST, 6SCT, and post-activity 6SCT titania samples. No signals of Cl 2p were detected indicating the non-oxidative propane dehydrogenation activity is solely based on titania. All samples exhibited similar patterns of Ti $2p_{1/2}$ and Ti$2p_{3/2}$ signals. However, O1s spectra revealed on oxygen vacancy signal at 530.1eV binding energy for fresh 6SCT sample in comparison with ST titania.
- UV-Visible spectroscopy for fresh and H_2 reduced ST and 6SCT titania samples at 500°C revealed an increased absorbance and red-shift of absorption edge for H_2 reduced samples in comparison with fresh samples.
- In-situ pyridine DRIFTS results for ST and 6SCT samples showed pyridine adsorption bands at 1443, 1489, 1574, and 1600cm^{-1}. These signals are associated with ν_{19b}, ν_{19a}, ν_{8b}, and ν_{8a} ring vibrations of pyridine respectively.

No signals associated with Bronsted acidic sites were detected for both samples. However, the signals were relatively intense for 6SCT in comparison with the ST titania sample.

- H_2-Temperature programmed reduction (TPR) for ST and 6SCT titania samples showed weak H_2 consumption around 600°C for both samples. The H_2 consumption signal was associated with the formation of water due to the interaction of H_2 with lattice oxygen.
- CO-Temperature programmed reduction (TPR) displayed multiple CO consumption signals for 6SCT whereas the ST sample exhibited only weak CO consumption. The CO consumption was associated with the interaction of CO with lattice oxygen. Multiple CO consumption for the 6SCT sample indicated different types of lattice defects over the 6SCT titania sample.
- Temperature programmed surface reaction (TPSR) of propane revealed that propane could be activated at a lower temperature of 502°C over 6SCT in comparison with ST titania where propane was activated at 583°C.
- Non-oxidative propane dehydrogenation activity tests at 1bar and 550°C revealed that:
    - The addition of 6mL,1M HCl during the sol-gel synthesis of titania resulted in the highest propane conversion and propene selectivity in comparison with other volumes of 1M HCl(0,2,8 and 10mL).
    - No pre-treatment of the 6SCT sample showed the highest initial propane conversion and propene selectivity in comparison with CO and H_2 pre-reduction for 1h.
    - For the ST sample, H_2 or CO pre-treatment positively affected the initial propane conversion and initial propene selectivity in comparison with no pretreatment.
    - Co-feeding H_2 with a propane stream negatively affected the initial propane conversion and propene selectivity in comparison with H_2-free feed.

    - By varying weight hourly space velocity(WHSV), different initial propane conversions could be achieved. Our results for the 6SCT sample showed that an initial propane conversion of approximately 25% is achievable with high 96% propene selectivity.
- Non-oxidative propane dehydrogenation activity at 600°C displayed a three times increase in the initial propane conversion over 6SCT titania in comparison with non-oxidative propane dehydrogenation activity at 550°C. For the ST sample, initial propane conversion nearly doubled at 600°C compared with 550°C. However, with increasing operating temperature the selectivity to propene was negatively affected for both samples.

All in all, our synthesized titania catalysts showed promising results for non-oxidative propane dehydrogenation. Unlike conventional non-oxidative propane dehydrogenation catalysts, our synthesized catalysts do not involve any expensive and toxic materials such as Pt and Cr_2O_3 respectively. Since the active sites over titania catalysts are surface defects, our synthesized catalysts are free from sintering or loss of structure which is typically observed in conventional non-oxidative propane dehydrogenation catalysts. Therefore, our study could be a breakthrough for non-oxidative propane dehydrogenation and could mitigate the economical and environmental challenges faced by commercial non-oxidative propane dehydrogenation technologies.

REFERENCES

[1] Polypropylene is now recommended in masks. Should I be concerned? Your mask questions answered | CBC News, (n.d.). https://www.cbc.ca/news/health/ask-covid-mask-questions-1.5782108 (accessed February 8, 2022).

[2] Phenol, (n.d.). https://www.bionity.com/en/encyclopedia/Phenol.html (accessed February 8, 2022).

[3] Coronavirus disease 2019: Affordable alternatives of household disinfectants for community, (n.d.). https://www.ncbi.nlm.nih.gov/pmc/articles/PMC7275191/ (accessed February 8, 2022).

[4] Acetone Properties & Uses | Chemical Safety Facts, (n.d.). https://www.chemicalsafetyfacts.org/acetone/ (accessed February 8, 2022).

[5] • Propylene production capacity globally 2030 | Statista, (n.d.). https://www.statista.com/statistics/1065879/global-propylene-production-capacity/ (accessed February 8, 2022).

[6] M. Monai, M. Gambino, S. Wannakao, B.M. Weckhuysen, Propane to olefins tandem catalysis: a selective route towards light olefins production, Chem. Soc. Rev. (2021). https://doi.org/10.1039/D1CS00357G.

[7] Applied Plastics Engineering Handbook, 2017. https://doi.org/10.1016/c2014-0-04118-4.

[8] T.K. Phung, T.L.M. Pham, K.B. Vu, G. Busca, (Bio)Propylene production processes: A critical review, J. Environ. Chem. Eng. 9 (2021). https://doi.org/10.1016/J.JECE.2021.105673.

[9] I. Amghizar, J.N. Dedeyne, D.J. Brown, G.B. Marin, K.M. Van Geem, Sustainable innovations in steam cracking: CO2 neutral olefin production, React. Chem. Eng. 5 (2020) 239–257. https://doi.org/10.1039/C9RE00398C.

[10] Z. Gholami, F. Gholami, Z. Tišler, M. Tomas, M. Vakili, A Review on Production of Light Olefins via Fluid Catalytic Cracking, Energies 2021, Vol. 14, Page 1089. 14 (2021) 1089. https://doi.org/10.3390/EN14041089.

[11] F. Güleç, W. Meredith, C.E. Snape, Progress in the CO2 Capture Technologies for Fluid Catalytic Cracking (FCC) Units—A Review, Front. Energy Res. 8 (2020) 62. https://doi.org/10.3389/FENRG.2020.00062/BIBTEX.

[12] D. Üner, Advances in refining catalysis, (n.d.) 410.

[13] X. Huang, F. Zhang, M. Fan, Y. Wang, Catalytic Coal Gasification, Sustain. Catal. Process. (2015) 179–199. https://doi.org/10.1016/B978-0-444-59567-6.00007-8.

[14] J.G. Speight, Handbook of industrial hydrocarbon processes, Handb. Ind. Hydrocarb. Process. (2019) 1–786. https://doi.org/10.1016/C2015-0-06314-6.

[15] Z. Teimouri, N. Abatzoglou, A.K. Dalai, Kinetics and Selectivity Study of Fischer–Tropsch Synthesis to C5+ Hydrocarbons: A Review, Catal. 2021, Vol. 11, Page 330. 11 (2021) 330. https://doi.org/10.3390/CATAL11030330.

[16] M.R. Gogate, Petroleum Science and Technology Methanol-to-olefins process technology: current status and future prospects Methanol-to-olefins process technology: current status and future prospects, (2019). https://doi.org/10.1080/10916466.2018.1555589.

[17] M. Yang, D. Fan, Y. Wei, P. Tian, Z. Liu, M. Yang, D. Fan, Y. Wei, P. Tian, Z. Liu, PROGRESS REPORT 1902181 (1 of 15) Recent Progress in Methanol-to-Olefins (MTO) Catalysts, (2019). https://doi.org/10.1002/adma.201902181.

[18] H. Koempel, W. Liebner, Lurgi's Methanol To Propylene (MTP®) Report on a successful commercialisation, Stud. Surf. Sci. Catal. 167 (2007) 261–267. https://doi.org/10.1016/S0167-2991(07)80142-X.

[19] A. Akah, M. Al-Ghrami, Maximizing propylene production via FCC technology, Appl. Petrochemical Res. 2015 54. 5 (2015) 377–392. https://doi.org/10.1007/S13203-015-0104-3.

[20] S. Bilgen, İ. Sarıkaya, New horizon in energy: Shale gas, J. Nat. Gas Sci. Eng. 35 (2016) 637–645. https://doi.org/10.1016/J.JNGSE.2016.09.014.

[21] J. Bellani, H.K. Verma, D. Khatri, D. Makwana, M. Shah, Shale gas: a step toward sustainable energy future, J. Pet. Explor. Prod. 11 (2021) 2127–2141. https://doi.org/10.1007/S13202-021-01157-7.

[22] X. Li, C. Pei, J. Gong, Shale gas revolution: Catalytic conversion of C1–C3 light alkanes to value-added chemicals, Chem. 7 (2021) 1755–1801. https://doi.org/10.1016/J.CHEMPR.2021.02.002.

[23] T. Otroshchenko, G. Jiang, V.A. Kondratenko, U. Rodemerck, E. V. Kondratenko, Current status and perspectives in oxidative, non-oxidative and CO 2 -mediated dehydrogenation of propane and isobutane over metal oxide catalysts, Chem. Soc. Rev. 50 (2021) 473–527. http://xlink.rsc.org/?DOI=D0CS01140A.

[24] J.H. Carter, T. Bere, J.R. Pitchers, D.G. Hewes, B.D. Vandegehuchte, C.J. Kiely, S.H. Taylor, G.J. Hutchings, Direct and oxidative dehydrogenation of propane: from catalyst design to industrial application, Green Chem. 23 (2021) 9747–9799. https://doi.org/10.1039/D1GC03700E.

[25] X. Chen, Y. Chen, C. Song, P. Ji, N. Wang, W. Wang, L. Cui, Recent Advances in Supported Metal Catalysts and Oxide Catalysts for the Reverse Water-Gas Shift Reaction, Front. Chem. 8 (2020) 709. https://doi.org/10.3389/fchem.2020.00709.

[26] M.A. Atanga, F. Rezaei, A. Jawad, M. Fitch, A.A. Rownaghi, Oxidative dehydrogenation of propane to propylene with carbon dioxide, Appl. Catal. B Environ. 220 (2018) 429–445. https://doi.org/10.1016/J.APCATB.2017.08.052.

[27] F. Cavani, N. Ballarini, A. Cericola, Oxidative dehydrogenation of ethane and propane: How far from commercial implementation?, Catal. Today. 127 (2007) 113–131. https://doi.org/10.1016/J.CATTOD.2007.05.009.

[28] S. Lawson, K. Baamran, K. Newport, T. Alghamadi, G. Jacobs, F. Rezaei, A.A. Rownaghi, Integrated direct air capture and oxidative dehydrogenation of propane with CO2 at isothermal conditions, Appl. Catal. B Environ. 303 (2022). https://doi.org/10.1016/J.APCATB.2021.120907.

[29] S. Chen, X. Chang, G. Sun, T. Zhang, Y. Xu, Y. Wang, C. Pei, J. Gong, Propane dehydrogenation: Catalyst development, new chemistry, and emerging technologies, Chem. Soc. Rev. 50 (2021) 3315–3354. https://doi.org/10.1039/D0CS00814A.

[30] Individual news – ICIS Explore, (n.d.). https://www.icis.com/explore/resources/news/2006/07/05/1070674/timeline-a-very-short-history-of-mtbe-in-the-us/ (accessed March 19, 2022).

[31] UPDATE - BASF: Agreement with ThyssenKrupp Industrial Solutions on development of PDH technology | Plasteurope.com, (n.d.). https://www.plasteurope.com/news/UPDATE_-_BASF_t245569/ (accessed March 21, 2022).

[32] Chromium: health effects | SA Health, (n.d.). https://www.sahealth.sa.gov.au/wps/wcm/connect/public+content/sa+health+internet/conditions/chemicals+and+contaminants/chromium+health+effects (accessed March 29, 2022).

[33] Chromium Toxicity - Nutritional Disorders - MSD Manual Professional Edition, (n.d.). https://www.msdmanuals.com/professional/nutritional-

disorders/mineral-deficiency-and-toxicity/chromium-toxicity (accessed March 29, 2022).

[34] Chromium Toxicity And Its Health Hazards, (n.d.). https://www.journalijar.com/article/5151/chromium-toxicity-and-its-health-hazards/ (accessed March 29, 2022).

[35] Platinum, (n.d.). https://nature.berkeley.edu/classes/eps2/wisc/pt.html (accessed March 29, 2022).

[36] Platinum facts, (n.d.). https://www.nrcan.gc.ca/our-natural-resources/minerals-mining/minerals-metals-facts/platinum-facts/20520 (accessed March 29, 2022).

[37] C. Sealy, The problem with platinum, Mater. Today. 11 (2008) 65–68. https://doi.org/10.1016/S1369-7021(08)70254-2.

[38] J. Tollefson, Energy crisis upsets platinum market, Nature. 451 (2008) 877. https://doi.org/10.1038/451877A.

[39] M. Martino, E. Meloni, G. Festa, V. Palma, Propylene synthesis: Recent advances in the use of pt-based catalysts for propane dehydrogenation reaction, Catalysts. 11 (2021). https://doi.org/10.3390/CATAL11091070.

[40] Chlorine (Cl) - Chemical properties, Health and Environmental effects, (n.d.). https://www.lenntech.com/periodic/elements/cl.htm (accessed March 31, 2022).

[41] Does Chlorine Gas Have a Negative Effect on the Environment?, (n.d.). https://education.seattlepi.com/chlorine-gas-negative-effect-environment-6120.html (accessed March 31, 2022).

[42] Chlorine, pollution and the environment - WEN Trust, (n.d.). https://www.mcspotlight.org/media/reports/wenchlorine.html (accessed March 31, 2022).

[43] Chlorine and compounds | National Pollutant Inventory, (n.d.). http://www.npi.gov.au/resource/chlorine-and-compounds (accessed March 31, 2022).

[44] M.J. Gázquez, J.P. Bolívar, R. Garcia-Tenorio, F. Vaca, M.J. Gázquez, J.P. Bolívar, R. Garcia-Tenorio, F. Vaca, A Review of the Production Cycle of Titanium Dioxide Pigment, Mater. Sci. Appl. 5 (2014) 441–458. https://doi.org/10.4236/MSA.2014.57048.

[45] C. Chen, J. Wang, Nanoscale Titanium Dioxide: Environmental Health and Ecotoxicological Effects, Encycl. Environ. Heal. (2011) 12–21. https://doi.org/10.1016/B978-0-444-52272-6.00646-2.

[46] J. Rouquerol, K.S.W. Sing, P. Llewellyn, Adsorption by Metal Oxides, Adsorpt. by Powders Porous Solids Princ. Methodol. Appl. Second Ed. (2014) 393–465. https://doi.org/10.1016/B978-0-08-097035-6.00011-5.

[47] M. Mohamad, B.U. Haq, R. Ahmed, A. Shaari, N. Ali, R. Hussain, A density functional study of structural, electronic and optical properties of titanium dioxide: Characterization of rutile, anatase and brookite polymorphs, Mater. Sci. Semicond. Process. 31 (2015) 405–414. https://doi.org/10.1016/J.MSSP.2014.12.027.

[48] I. Ali, M. Suhail, Z.A. Alothman, A. Alwarthan, Recent advances in syntheses, properties and applications of TiO 2 nanostructures, (2018). https://doi.org/10.1039/c8ra06517a.

[49] J. Zhang, P. Zhou, J. Liu, J. Yu, New understanding of the difference of photocatalytic activity among anatase, rutile and brookite TiO2, Phys. Chem. Chem. Phys. 16 (2014) 20382–20386. https://doi.org/10.1039/C4CP02201G.

[50] M. Carlo Ye Luo, A. Benali, L. Shulenburger, al -, T. Thuong Huyen Tran, H. Kosslick, A. Schulz, D. Reyes-Coronado, G. Rodríguez-Gattorno, M.E. Espinosa-Pesqueira, C. Cab, R. de Coss, G. Oskam, Phase-pure TiO2 nanoparticles: anatase, brookite and rutile, Nanotechnology. 19 (2008)

145605. https://doi.org/10.1088/0957-4484/19/14/145605.

[51] N.S. Allen, N. Mahdjoub, V. Vishnyakov, P.J. Kelly, R.J. Kriek, The effect of crystalline phase (anatase, brookite and rutile) and size on the photocatalytic activity of calcined polymorphic titanium dioxide (TiO2), Polym. Degrad. Stab. 150 (2018) 31–36. https://doi.org/10.1016/J.POLYMDEGRADSTAB.2018.02.008.

[52] N. Mahdjoub, N. Allen, P. Kelly, V. Vishnyakov, Thermally induced phase and photocatalytic activity evolution of polymorphous titania, J. Photochem. Photobiol. A Chem. 210 (2010) 125–129. https://doi.org/10.1016/J.JPHOTOCHEM.2010.01.007.

[53] Z. Zhang, J.T. Yates, Defects on TiO2—key pathways to important surface processes, Springer Ser. Surf. Sci. 58 (2015) 81–121. https://doi.org/10.1007/978-3-319-14367-5_3/FIGURES/22.

[54] C. Foo, Y. Li, K. Lebedev, T. Chen, S. Day, C. Tang, S.C.E. Tsang, Characterisation of oxygen defects and nitrogen impurities in TiO2 photocatalysts using variable-temperature X-ray powder diffraction, Nat. Commun. 2021 121. 12 (2021) 1–13. https://doi.org/10.1038/s41467-021-20977-z.

[55] A. Kumar, V. Krishnan, A. Kumar, V. Krishnan, Vacancy Engineering in Semiconductor Photocatalysts: Implications in Hydrogen Evolution and Nitrogen Fixation Applications, Adv. Funct. Mater. 31 (2021) 2009807. https://doi.org/10.1002/ADFM.202009807.

[56] S. Rehman, R. Ullah, A.M. Butt, N.D. Gohar, Strategies of making TiO2 and ZnO visible light active, J. Hazard. Mater. 170 (2009) 560–569. https://doi.org/10.1016/J.JHAZMAT.2009.05.064.

[57] J. Su, X. Zou, J.S. Chen, Self-modification of titanium dioxide materials by Ti3+ and/or oxygen vacancies: New insights into defect chemistry of metal oxides, RSC Adv. 4 (2014) 13979–13988.

https://doi.org/10.1039/c3ra47757f.

[58] X. Pan, M.Q. Yang, X. Fu, N. Zhang, Y.J. Xu, Defective TiO2 with oxygen vacancies: synthesis, properties and photocatalytic applications, Nanoscale. 5 (2013) 3601–3614. https://doi.org/10.1039/C3NR00476G.

[59] Y. Huang, Y. Yu, Y. Yu, B. Zhang, Oxygen Vacancy Engineering in Photocatalysis, Sol. RRL. 4 (2020). https://doi.org/10.1002/solr.202000037.

[60] H. Liu, H.T. Ma, X.Z. Li, W.Z. Li, M. Wu, X.H. Bao, The enhancement of TiO2 photocatalytic activity by hydrogen thermal treatment, Chemosphere. 50 (2003) 39–46. https://doi.org/10.1016/S0045-6535(02)00486-1.

[61] C.F. Li, X. Guo, Q.H. Shang, X. Yan, C. Ren, W.Z. Lang, Y.J. Guo, Defective TiO2 for Propane Dehydrogenation, Ind. Eng. Chem. Res. 59 (2020) 4377–4387. https://doi.org/10.1021/ACS.IECR.9B06759/SUPPL_FILE/IE9B06759_SI_001.PDF.

[62] Y. Zhao, Y. Zhao, R. Shi, B. Wang, G.I. N Waterhouse, L.-Z. Wu, C.-H. Tung, T. Zhang, Y.X. Zhao, R. Shi, L. Wu, C. Tung, T. Zhang, Y.F. Zhao, B. Wang, G.I. N Waterhouse, Tuning Oxygen Vacancies in Ultrathin TiO2 Nanosheets to Boost Photocatalytic Nitrogen Fixation up to 700 nm, Adv. Mater. 31 (2019) 1806482. https://doi.org/10.1002/ADMA.201806482.

[63] Z. Wang, C. Yang, T. Lin, H. Yin, P. Chen, D. Wan, F. Xu, F. Huang, J. Lin, X. Xie, M. Jiang, Visible-light photocatalytic, solar thermal and photoelectrochemical properties of aluminium-reduced black titania, Energy Environ. Sci. 6 (2013) 3007–3014. https://doi.org/10.1039/C3EE41817K.

[64] Z. Zhao, H. Tan, H. Zhao, Y. Lv, L.J. Zhou, Y. Song, Z. Sun, Reduced TiO 2 rutile nanorods with well-defined facets and their visible-light photocatalytic activity, Chem. Commun. 50 (2014) 2755–2757. https://doi.org/10.1039/C3CC49182J.

[65] J. Xia, H. Zhao, W.K. Pang, Z. Yin, B. Zhou, G. He, Z. Guo, Y. Du, Lanthanide doping induced electrochemical enhancement of Na2Ti3O7 anodes for sodium-ion batteries, Chem. Sci. 9 (2018) 3421–3425. https://doi.org/10.1039/C7SC05185A.

[66] D. Li, H. Haneda, N.K. Labhsetwar, S. Hishita, N. Ohashi, Visible-light-driven photocatalysis on fluorine-doped TiO2 powders by the creation of surface oxygen vacancies, Chem. Phys. Lett. 401 (2005) 579–584. https://doi.org/10.1016/J.CPLETT.2004.11.126.

[67] Z. Cao, T. Zhang, P. Ren, D. Cao, Y. Lin, L. Wang, B. Zhang, X. Xiang, Doping of Chlorine from a Neoprene Adhesive Enhances Degradation Efficiency of Dyes by Structured TiO2-Coated Photocatalytic Fabrics, Catal. 2020, Vol. 10, Page 69. 10 (2020) 69. https://doi.org/10.3390/CATAL10010069.

[68] Y.W. Sakai, K. Obata, K. Hashimoto, H. Irie, Enhancement of visible light-induced hydrophilicity on nitrogen and sulfur-codoped TiO2 thin films, Vacuum. 83 (2008) 683–687. https://doi.org/10.1016/J.VACUUM.2008.04.022.

[69] F. Wei, L. Ni, P. Cui, Preparation and characterization of N–S-codoped TiO2 photocatalyst and its photocatalytic activity, J. Hazard. Mater. 156 (2008) 135–140. https://doi.org/10.1016/J.JHAZMAT.2007.12.018.

[70] S. In, A. Orlov, R. Berg, F. García, S. Pedrosa-Jimenez, M.S. Tikhov, D.S. Wright, R.M. Lambert, Effective visible light-activated B-doped and B,N-codoped TiO2 photocatalysts, J. Am. Chem. Soc. 129 (2007) 13790–13791. https://doi.org/10.1021/JA0749237/SUPPL_FILE/JA0749237SI20071004_060913.PDF.

[71] S. Banerjee, D.D. Dionysiou, S.C. Pillai, Self-cleaning applications of TiO2 by photo-induced hydrophilicity and photocatalysis, Appl. Catal. B Environ. 176–177 (2015) 396–428. https://doi.org/10.1016/J.APCATB.2015.03.058.

[72] H. Tan, Z. Zhao, M. Niu, C. Mao, D. Cao, D. Cheng, P. Feng, Z. Sun, A facile and versatile method for preparation of colored TiO2 with enhanced solar-driven photocatalytic activity, Nanoscale. 6 (2014) 10216–10223. https://doi.org/10.1039/C4NR02677B.

[73] A. Sinhamahapatra, J.P. Jeon, J.S. Yu, A new approach to prepare highly active and stable black titania for visible light-assisted hydrogen production, Energy Environ. Sci. 8 (2015) 3539–3544. https://doi.org/10.1039/C5EE02443A.

[74] F. Zuo, L. Wang, T. Wu, Z. Zhang, D. Borchardt, P. Feng, Self-doped Ti3+ enhanced photocatalyst for hydrogen production under visible light, J. Am. Chem. Soc. 132 (2010) 11856–11857. https://doi.org/10.1021/JA103843D/SUPPL_FILE/JA103843D_SI_001.PDF .

[75] C. Fan, C. Chen, J. Wang, X. Fu, Z. Ren, G. Qian, Z. Wang, Black Hydroxylated Titanium Dioxide Prepared via Ultrasonication with Enhanced Photocatalytic Activity, Sci. Reports 2015 51. 5 (2015) 1–10. https://doi.org/10.1038/srep11712.

[76] F.Z. Haque, R. Nandanwar, P. Singh, Evaluating photodegradation properties of anatase and rutile TiO2 nanoparticles for organic compounds, Optik (Stuttg). 128 (2017) 191–200. https://doi.org/10.1016/J.IJLEO.2016.10.025.

[77] M. D'Arienzo, R. Scotti, B. Di Credico, M. Redaelli, Synthesis and Characterization of Morphology-Controlled TiO2 Nanocrystals: Opportunities and Challenges for their Application in Photocatalytic Materials, Stud. Surf. Sci. Catal. 177 (2017) 477–540. https://doi.org/10.1016/B978-0-12-805090-3.00013-9.

[78] A. Sarkar, N. Saha, G. Majumdar, Fabrication and Characterization of Flexible Semi-conducting Nanocomposite Polymer, Ref. Modul. Mater. Sci. Mater. Eng. (2022). https://doi.org/10.1016/B978-0-12-820352-1.00198-X.

[79] E. Yilmaz, M. Soylak, Functionalized nanomaterials for sample preparation methods, Handb. Nanomater. Anal. Chem. Mod. Trends Anal. (2019) 375–413. https://doi.org/10.1016/B978-0-12-816699-4.00015-3.

[80] C. Bock, H. Halvorsen, B. Macdougall, Catalyst Synthesis Techniques, (2009).

[81] T.K. Tseng, Y.S. Lin, Y.J. Chen, H. Chu, A Review of Photocatalysts Prepared by Sol-Gel Method for VOCs Removal, Int. J. Mol. Sci. 2010, Vol. 11, Pages 2336-2361. 11 (2010) 2336–2361. https://doi.org/10.3390/IJMS11062336.

[82] S. Gopal Ullattil, P. Periyat, S. Ullattil, P. Periyat, S. Pillai, S. Hehir, Sol-Gel Synthesis of Titanium Dioxide, Adv. Sol-Gel Deriv. Mater. Technol. (2017) 271–283. https://doi.org/10.1007/978-3-319-50144-4_9.

[83] A. Schmid, F. Kersten, S. Rentrop, al -, M. Joozdani -, P. Khodaparast, Z. Ounaies, Influence of dispersion states on the performance of polymer-based nanocomposites, Smart Mater. Struct. 23 (2014) 104004. https://doi.org/10.1088/0964-1726/23/10/104004.

[84] J. Bergek, B. Elgh, A.E.C. Palmqvist, L. Nordstierna, Formation of titanium dioxide core–shell microcapsules through a binary-phase spray technique, Phys. Chem. Chem. Phys. 19 (2017) 23878–23886. https://doi.org/10.1039/C7CP02571H.

[85] A. Mezni, ab Nesrine Ben Saber, M.M. Ibrahim, bc Maged El-Kemary, cd Ali Aldalbahi, P. Feng, L. Samia Smiri, T. Altalhi, Facile synthesis of highly thermally stable TiO 2 photocatalysts, New J. Chem. 41 (2017) 5021. https://doi.org/10.1039/c7nj00747g.

[86] B.H. Stott T, A. Professor of Physical Chemistry, A theory of the catalytic surface, Proc. R. Soc. London. Ser. A, Contain. Pap. a Math. Phys. Character. 108 (1925) 105–111. https://doi.org/10.1098/RSPA.1925.0061.

[87] M. Boudart, Catalysis by Supported Metals, Adv. Catal. 20 (1969) 153–166. https://doi.org/10.1016/S0360-0564(08)60271-0.

[88] A.S. Crampton, M.D. Rötzer, C.J. Ridge, B. Yoon, F.F. Schweinberger, U. Landman, U. Heiz, Assessing the concept of structure sensitivity or insensitivity for sub-nanometer catalyst materials, Surf. Sci. 652 (2016) 7–19. https://doi.org/10.1016/J.SUSC.2016.02.006.

[89] N.D. Spencer, R.C. Schoonmaker, G.A. Somorjai, Iron single crystals as ammonia synthesis catalysts: Effect of surface structure on catalyst activity, J. Catal. 74 (1982) 129–135. https://doi.org/10.1016/0021-9517(82)90016-1.

[90] Y. Pan, X. Shen, L. Yao, A. Bentalib, Z. Peng, Active Sites in Heterogeneous Catalytic Reaction on Metal and Metal Oxide: Theory and Practice, Catal. 2018, Vol. 8, Page 478. 8 (2018) 478. https://doi.org/10.3390/CATAL8100478.

[91] Y. Zhang, Y. Zhao, T. Otroshchenko, A. Perechodjuk, V.A. Kondratenko, S. Bartling, U. Rodemerck, D. Linke, H. Jiao, G. Jiang, E. Kondratenko V, Structure-Activity-Selectivity Relationships in Propane Dehydrogenation over Rh/ZrO2 Catalysts, ACS Catal. 10 (2020) 6377–6388. https://doi.org/10.1021/acscatal.0c01455.

[92] Z. Xie, T. Yu, W. Song, J. Li, Z. Zhao, B. Liu, Z. Gao, D. Li, Highly active nanosized anatase TiO2−x oxide catalysts in situ formed through reduction and Ostwald ripening processes for propane dehydrogenation, ACS Catal. 10 (2020) 14678–14693. https://doi.org/10.1021/ACSCATAL.0C02825/SUPPL_FILE/CS0C02825_SI_001.PDF.

[93] T. Otroshchenko, S. Sokolov, M. Stoyanova, V.A. Kondratenko, U. Rodemerck, D. Linke, E. V. Kondratenko, ZrO2-Based Alternatives to Conventional Propane Dehydrogenation Catalysts: Active Sites, Design, and Performance, Angew. Chemie Int. Ed. 54 (2015) 15880–15883.

https://doi.org/10.1002/ANIE.201508731.

[94] T. Otroshchenko, V.A. Kondratenko, U. Rodemerck, D. Linke, E. V. Kondratenko, ZrO2-based unconventional catalysts for non-oxidative propane dehydrogenation: Factors determining catalytic activity, J. Catal. 348 (2017) 282–290. https://doi.org/10.1016/j.jcat.2017.02.016.

[95] Y. Zhang, Y. Zhao, T. Otroshchenko, H. Lund, M.-M. Pohl, U. Rodemerck, D. Linke, H. Jiao, G. Jiang, E. V Kondratenko, Control of coordinatively unsaturated Zr sites in ZrO2 for efficient C–H bond activation, Nat. Commun. 9 (2018) 3794. https://doi.org/10.1038/s41467-018-06174-5.

[96] D. Eder, R. Kramer, The stoichiometry of hydrogen reduced zirconia and its influence on catalytic activity - Part 1: Volumetric and conductivity studies, Phys. Chem. Chem. Phys. 4 (2002) 795–801. https://doi.org/10.1039/B109887J.

[97] C. Gionco, M.C. Paganini, E. Giamello, R. Burgess, C. Di Valentin, G. Pacchioni, Paramagnetic Defects in Polycrystalline Zirconia: An EPR and DFT Study, (2013). https://doi.org/10.1021/cm400728j.

[98] C.-F. Li, X. Guo, Q.-H. Shang, X. Yan, C. Ren, W.-Z. Lang, Y.-J. Guo, Defective TiO2 for Propane Dehydrogenation, Ind. Eng. Chem. Res. 59 (2020) 4377–4387. https://doi.org/10.1021/acs.iecr.9b06759.

[99] W. Yu, ab Fengjie Chen, ab Yarui Wang ab, L. Zhao, Rapid evaluation of oxygen vacancies-enhanced photogeneration of the superoxide radical in nano-TiO 2 suspensions †, (2020). https://doi.org/10.1039/d0ra06299e.

[100] O. Al-Madanat, B.N. Nunes, Y. Alsalka, A. Hakki, M. Curti, A.O.T. Patrocinio, D.W. Bahnemann, Application of EPR Spectroscopy in TiO2 and Nb2O5 Photocatalysis, Catal. 2021, Vol. 11, Page 1514. 11 (2021) 1514. https://doi.org/10.3390/CATAL11121514.

[101] J. Wan, W. Chen, C. Jia, L. Zheng, J. Dong, X. Zheng, Y. Wang, W. Yan, C.

Chen, Q. Peng, D. Wang, Y. Li, J.W. Wan, W.X. Chen, C. Chen, Q. Peng, D.S. Wang, Y.D. Li, C.Y. Jia, L.R. Zheng, J.C. Dong, X.S. Zheng, W.S. Yan, Y. Wang, Defect Effects on TiO2 Nanosheets: Stabilizing Single Atomic Site Au and Promoting Catalytic Properties, Adv. Mater. 30 (2018) 1705369. https://doi.org/10.1002/ADMA.201705369.

[102] M. Dixit, P. Kostetskyy, G. Mpourmpakis, Structure-Activity Relationships in Alkane Dehydrogenation on γ-Al2O3: Site-Dependent Reactions, ACS Catal. 8 (2018) 11570–11578. https://doi.org/10.1021/ACSCATAL.8B03484/SUPPL_FILE/CS8B03484_SI_001.PDF.

[103] M.I. Zaki, M.A. Hasan, F.A. Al-Sagheer, L. Pasupulety, In situ FTIR spectra of pyridine adsorbed on SiO2–Al2O3, TiO2, ZrO2 and CeO2: general considerations for the identification of acid sites on surfaces of finely divided metal oxides, Colloids Surfaces A Physicochem. Eng. Asp. 190 (2001) 261–274. https://doi.org/10.1016/S0927-7757(01)00690-2.

[104] N.S. Gould, B. Xu, Quantification of acid site densities on zeolites in the presence of solvents via determination of extinction coefficients of adsorbed pyridine, J. Catal. 358 (2018) 80–88. https://doi.org/10.1016/J.JCAT.2017.11.016.

[105] P. Wang, Z. Xu, T. Wang, Y. Yue, X. Bao, H. Zhu, Unmodified bulk alumina as an efficient catalyst for propane dehydrogenation, Catal. Sci. Technol. 10 (2020) 3537–3541. https://doi.org/10.1039/D0CY00779J.

[106] T.P. Otroshchenko, V.A. Kondratenko, U. Rodemerck, D. Linke, E. V Kondratenko, Non-oxidative dehydrogenation of propane, n-butane, and isobutane over bulk ZrO2-based catalysts: effect of dopant on the active site and pathways of product formation, Catal. Sci. Technol. 7 (2017) 4499–4510. https://doi.org/10.1039/c7cy01583f.

[107] Y. Zhang, Y. Zhao, T. Otroshchenko, S. Han, H. Lund, U. Rodemerck, D.

Linke, H. Jiao, G. Jiang, E. V Kondratenko, The effect of phase composition and crystallite size on activity and selectivity of ZrO2 in non-oxidative propane dehydrogenation, J. Catal. 371 (2019) 313–324. https://doi.org/10.1016/j.jcat.2019.02.012.

[108] A. Bouziani, J. Park, A. Ozturk, Synthesis of α-Fe2O3/TiO2 heterogeneous composites by the sol-gel process and their photocatalytic activity, J. Photochem. Photobiol. A Chem. 400 (2020) 112718. https://doi.org/10.1016/J.JPHOTOCHEM.2020.112718.

[109] V.S. Vinila, J. Isac, Synthesis and structural studies of superconducting perovskite GdBa2Ca3Cu4O10.5+δ nanosystems, Des. Fabr. Charact. Multifunct. Nanomater. (2022) 319–341. https://doi.org/10.1016/B978-0-12-820558-7.00022-4.

[110] A. Grozdanov, A. Ce, P. Makreski, G. Gentile, B. Ranguelov, E. Fidančevska, Characterization of Nanoscaled TiO 2 Produced by Simplified Sol-Gel Method Using Organometallic Precursor, (2015). https://doi.org/10.1115/1.4029112.

[111] S. Yurdakal, Ş.Ö. Yanar, S. Çetinkaya, O. Alagöz, P. Yalçın, L. Özcan, Green photocatalytic synthesis of vitamin B3 by Pt loaded TiO2 photocatalysts, Appl. Catal. B Environ. 202 (2017) 500–508. https://doi.org/10.1016/J.APCATB.2016.09.063.

[112] N. Saikumari, S.M. Dev, S.A. Dev, Effect of calcination temperature on the properties and applications of bio extract mediated titania nano particles, Sci. Reports 2021 111. 11 (2021) 1–17. https://doi.org/10.1038/s41598-021-80997-z.

[113] M.M. Viana, V.F. Soares, N.D.S. Mohallem, Synthesis and characterization of TiO2 nanoparticles, Ceram. Int. 36 (2010) 2047–2053. https://doi.org/10.1016/J.CERAMINT.2010.04.006.

[114] R. Trejo-Tzab, L. Caballero-Espada, P. Quintana, A. Ávila-Ortega, R.A.

Medina-Esquivel, Controlled Phase Changes of Titania Using Nitrogen Plasma, Nanoscale Res. Lett. 12 (2017) 1–8. https://doi.org/10.1186/S11671-016-1821-Y/FIGURES/6.

[115] J.Y. Huh, J. Lee, S.Z.A. Bukhari, J.H. Ha, I.H. Song, Development of TiO2-coated YSZ/silica nanofiber membranes with excellent photocatalytic degradation ability for water purification, Sci. Reports 2020 101. 10 (2020) 1–12. https://doi.org/10.1038/s41598-020-74637-1.

[116] L.M. Anaya-Esparza, N. González-Silva, E.M. Yahia, O.A. González-Vargas, E. Montalvo-González, A. Pérez-Larios, Effect of TiO 2-ZnO-MgO Mixed Oxide on Microbial Growth and Toxicity against Artemia salina, (2019). https://doi.org/10.3390/nano9070992.

[117] H.G. Yang, H.C. Zeng, Preparation of hollow anatase TiO2 nanospheres via Ostwald ripening, J. Phys. Chem. B. 108 (2004) 3492–3495. https://doi.org/10.1021/JP0377782/SUPPL_FILE/JP0377782SI20031210_013758.PDF.

[118] Q. Wu, Q. Zheng, R. Van De Krol, Creating oxygen vacancies as a novel strategy to form tetrahedrally coordinated Ti 4+ in Fe/TiO 2 nanoparticles, J. Phys. Chem. C. 116 (2012) 7219–7226. https://doi.org/10.1021/JP212577G/ASSET/IMAGES/LARGE/JP-2011-12577G_0008.JPEG.

[119] T. Xia, X. Chen, Revealing the structural properties of hydrogenated black TiO2 nanocrystals, J. Mater. Chem. A. 1 (2013) 2983–2989. https://doi.org/10.1039/C3TA01589K.

[120] An Introduction to Raman Spectroscopy: Introduction and Basic Principles - 2014 - Wiley Analytical Science, (n.d.). https://analyticalscience.wiley.com/do/10.1002/sepspec.1882education/full/ (accessed May 14, 2022).

[121] M. Khorasaninejad, M.M. Adachi, J. Walia, K.S. Karim, S.S. Saini, Raman

spectroscopy of core/shell silicon nanowires grown on different substrates, Phys. Status Solidi. 210 (2013) 373–377. https://doi.org/10.1002/PSSA.201228235.

[122] A.K.P.D. Savio, J. Fletcher, K. Smith, R. Iyer, J.M. Bao, F.C. Robles Hernández, Environmentally effective photocatalyst CoO–TiO2 synthesized by thermal precipitation of Co in amorphous TiO2, Appl. Catal. B Environ. 182 (2016) 449–455. https://doi.org/10.1016/J.APCATB.2015.09.047.

[123] H. Song, C. Li, Z. Lou, Z. Ye, L. Zhu, Effective Formation of Oxygen Vacancies in Black TiO2 Nanostructures with Efficient Solar-Driven Water Splitting, ACS Sustain. Chem. Eng. 5 (2017) 8982–8987. https://doi.org/10.1021/ACSSUSCHEMENG.7B01774/SUPPL_FILE/SC7B01774_SI_001.PDF.

[124] Q. Wang, S. Zhang, H. He, C. Xie, Y. Tang, C. He, M. Shao, H. Wang, Oxygen Vacancy Engineering in Titanium Dioxide for Sodium Storage, Chem. – An Asian J. 16 (2021) 3–19. https://doi.org/10.1002/ASIA.202001172.

[125] J. Chen, Z. Ding, C. Wang, H. Hou, Y. Zhang, C. Wang, G. Zou, X. Ji, Black Anatase Titania with Ultrafast Sodium-Storage Performances Stimulated by Oxygen Vacancies, ACS Appl. Mater. Interfaces. 8 (2016) 9142–9151. https://doi.org/10.1021/ACSAMI.6B01183/ASSET/IMAGES/AM-2016-011835_M001.GIF.

[126] T. Gakhar, A. Hazra, Oxygen vacancy modulation of titania nanotubes by cathodic polarization and chemical reduction routes for efficient detection of volatile organic compounds, V. 12 (2020) 9082–9093. https://doi.org/10.1039/C9NR10795A.

[127] Y. Zhao, D. Wu, T. Tang, Y. Sun, One-step synthesis of hydrophobic mesoporous silica ellipsoidal particles with a bimodal mesopore system, Mater. Res. Bull. 48 (2013) 4839–4843.

https://doi.org/10.1016/J.MATERRESBULL.2013.08.026.

[128] L. Lyu, M. Shengene, Q. Ma, J. Sun, X. Gao, H. Fan, J. Zhang, T.S. Zhao, Synergy of macro-meso bimodal pore and Ni-Co alloy for enhanced stability in dry reforming of methane, Fuel. 310 (2022) 122375. https://doi.org/10.1016/J.FUEL.2021.122375.

[129] H. Yan, G. Zhang, Y. Xu, Q. Zhang, J. Liu, G. Li, Y. Zhao, Y. Wang, Y. Zhang, High CO2 adsorption on amine-functionalized improved macro-/mesoporous multimodal pore silica, Fuel. 315 (2022) 123195. https://doi.org/10.1016/J.FUEL.2022.123195.

[130] T. Tao, A.M. Glushenkov, Q. Chen, H. Hu, D. Zhou, H. Zhang, M. Boese, S. Liu, R. Amal, Y. Chen, Porous TiO 2 with a controllable bimodal pore size distribution from natural ilmenite, CrystEngComm. 13 (2011) 1322–1327. https://doi.org/10.1039/C0CE00533A.

[131] H. Funabashi, S. Takeuchi, S. Tsujimura, Hierarchical meso/macro-porous carbon fabricated from dual MgO templates for direct electron transfer enzymatic electrodes, Sci. Reports 2017 71. 7 (2017) 1–9. https://doi.org/10.1038/srep45147.

[132] T. Yuan, W. Zhang, W.T. Li, C. Song, Y.S. He, J.M. Razal, Z.F. Ma, J. Chen, N-doped pierced graphene microparticles as a highly active electrocatalyst for Li-air batteries, 2D Mater. 2 (2015). https://doi.org/10.1088/2053-1583/2/2/024002.

[133] G. Sun, K. Li, L. Xie, J. Wang, Y. Li, Preparation of mesoporous carbon spheres with a bimodal pore size distribution and its application for electrochemical double layer capacitors based on ionic liquid as the electrolyte, Microporous Mesoporous Mater. 151 (2012) 282–286. https://doi.org/10.1016/J.MICROMESO.2011.10.023.

[134] H. Qian, F. Sun, W. Zhang, C. Huang, Y. Wang, K. Fang, Efficient metal borate catalysts for oxidative dehydrogenation of propane, Catal. Sci.

Technol. (2022). https://doi.org/10.1039/D1CY01792F.

[135] J.Y. Tai, K.H. Leong, P. Saravanan, A.A. Aziz, L.C. Sim, Dopant-free oxygen-rich titanium dioxide: LED light-induced photocatalysis and mechanism insight, J. Mater. Sci. 52 (2017) 11630–11642. https://doi.org/10.1007/S10853-017-1334-9/FIGURES/9.

[136] B. Bharti, S. Kumar, H.N. Lee, R. Kumar, Formation of oxygen vacancies and Ti3+ state in TiO2 thin film and enhanced optical properties by air plasma treatment, Sci. Reports 2016 61. 6 (2016) 1–12. https://doi.org/10.1038/srep32355.

[137] D. Himmel, V. Radtke, B. Butschke, I. Krossing, Basic Remarks on Acidity, Angew. Chemie Int. Ed. 57 (2018) 4386–4411. https://doi.org/10.1002/ANIE.201709057.

[138] T. Beutel, C. Bai, G. Woolery, S. McCarthy, J. McConnachie, C. Kliewer, K. Hajkowski, A. Thornburg, Acidity in Titania–Alumina Mixed Metal Oxides, Top. Catal. 60 (2017) 1565–1576. https://doi.org/10.1007/S11244-017-0839-4/FIGURES/15.

[139] T. Bezrodna, G. Puchkovska, V. Shimanovska, I. Chashechnikova, T. Khalyavka, J. Baran, Pyridine-TiO2 surface interaction as a probe for surface active centers analysis, Appl. Surf. Sci. 214 (2003) 222–231. https://doi.org/10.1016/S0169-4332(03)00346-5.

[140] C.H. Kline, J. Turkevich, The Vibrational Spectrum of Pyridine and the Thermodynamic Properties of Pyridine Vapors, JChPh. 12 (1944) 300–309. https://doi.org/10.1063/1.1723943.

[141] F. Partal Ureña, M.F. Gómez, J.J. López González, E. Martínez Torres, A new insight into the vibrational analysis of pyridine, Spectrochim. Acta Part A Mol. Biomol. Spectrosc. 59 (2003) 2815–2839. https://doi.org/10.1016/S1386-1425(03)00082-9.

[142] N. Zhang, Z. Yang, Z. Chen, Y. Li, Y. Liao, Y. Li, M. Gong, Y. Chen, Synthesis of Sulfur-Resistant TiO2-CeO2 Composite and Its Catalytic Performance in the Oxidation of a Soluble Organic Fraction from Diesel Exhaust, Catal. 2018, Vol. 8, Page 246. 8 (2018) 246. https://doi.org/10.3390/CATAL8060246.

[143] S. Watanabe, X. Ma, C. Song, Characterization of structural and surface properties of nanocrystalline TiO2-CeO2 mixed oxides by XRD, XPS, TPR, and TPD, J. Phys. Chem. C. 113 (2009) 14249–14257. https://doi.org/10.1021/JP8110309/SUPPL_FILE/JP8110309_SI_001.PDF.

[144] H. Zhu, Z. Qin, W. Shan, W. Shen, J. Wang, Pd/CeO2–TiO2 catalyst for CO oxidation at low temperature: a TPR study with H2 and CO as reducing agents, J. Catal. 225 (2004) 267–277. https://doi.org/10.1016/J.JCAT.2004.04.006.

[145] T. Otroshchenko, O. Bulavchenko, H. V. Thanh, J. Rabeah, U. Bentrup, A. Matvienko, U. Rodemerck, B. Paul, R. Kraehnert, D. Linke, E. V. Kondratenko, Controlling activity and selectivity of bare ZrO2 in non-oxidative propane dehydrogenation, Appl. Catal. A Gen. 585 (2019) 117189. https://doi.org/10.1016/j.apcata.2019.117189.

[146] T. Otroshchenko, E. V. Kondratenko, Effect of hydrogen and supported metal on selectivity and on-stream stability of ZrO2-based catalysts in non-oxidative propane dehydrogenation, Catal. Commun. 144 (2020) 106068. https://doi.org/10.1016/j.catcom.2020.106068.

APPENDICES

Appendix A

Crystallite size calculation

Herein, a sample calculation for determining the average crystallite size for the 6SCT titania sample is given. XRD data for the 6SCT sample is given in Table A.1 below:

Table A.1 XRD data for 6SCT

2θ(°)	FWHM(°)	hkl
25.50	0.72	101
38.08	0.64	004
48.26	0.72	200
54.22	0.76	105
55.30	0.72	211

Crystallite size(d) was calculated for each plane(hkl) using Scherrer equation as follows:

$$d = \frac{k\lambda}{\beta Cos\theta}$$

where,

k: Shape factor constant(0.9 for spherical particles)

λ: X-ray wavelength(0.15406nm for Cu- Kα irradiation source)

β: Full width at half maximum (FWHM)

θ: Bragg angle

For plane 101, crystallite size can be calculated as:

$$d = \frac{k\lambda}{\beta Cos\theta} = \frac{0.9 * 0.15406nm}{Radians(0.72°)Cos(Radians(25.5°/2))} = 11.3nm$$

Similarly, the crystallite size for other planes(hkl) could be calculated to yield an average crystallite size of 16.4nm.

Appendix B

Effect of pretreatment conditions under different atmospheres for non-oxidative propane dehydrogenation activity

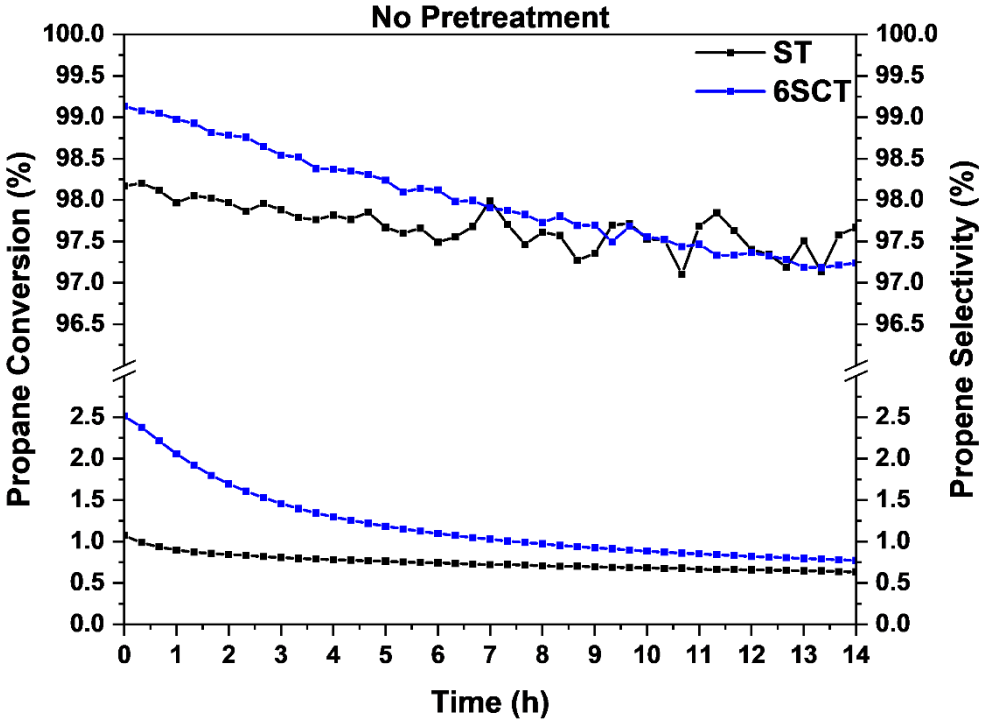

Figure B.1. Propane conversion and propene selectivity as a function of time on stream for ST and 6SCT titania. Test conditions: Temperature:550°C, Pressure:1bar, Catalyst mass: 200mg, Feed flow rate: 30sccm C_3H_8:Ar=7:93

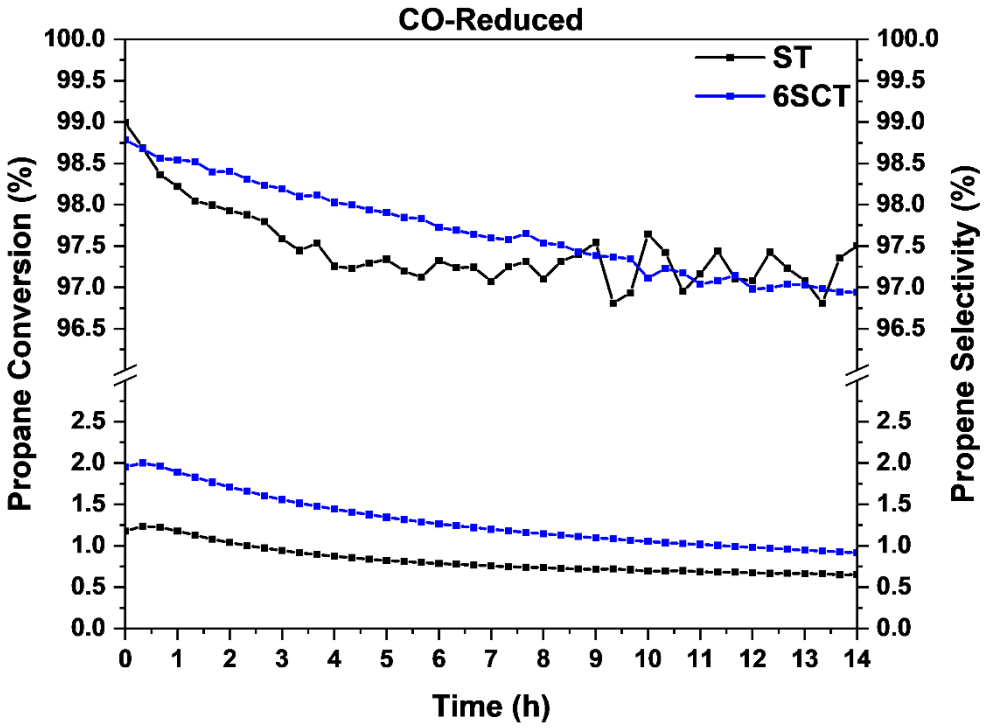

Figure B.2. Propane conversion and propene selectivity as a function of time on stream for ST and 6SCT titania. Test conditions: Temperature:550°C, Pressure:1bar, Catalyst mass: 200mg, Pretreatment: 30sccm 10vol% CO in Ar for 1h, Feed flow rate: 30sccm C_3H_8:Ar=7:93

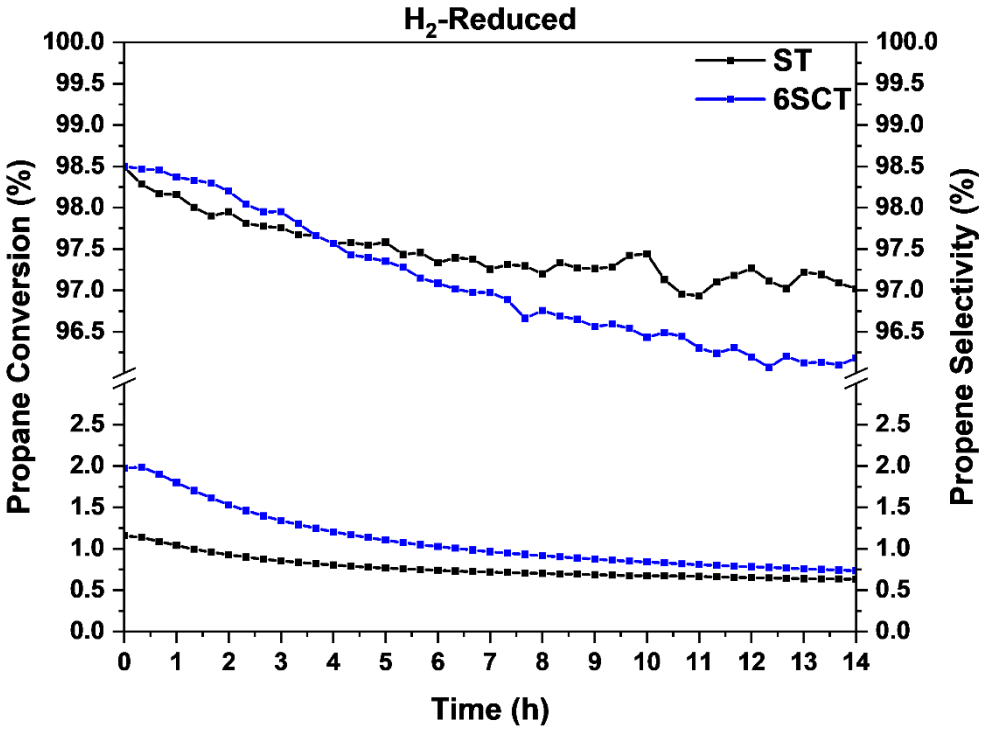

Figure B.3. Propane conversion and propene selectivity as a function of time on stream for ST and 6SCT titania. Test conditions: Temperature:550°C, Pressure:1bar, Catalyst mass: 200mg, Pretreatment: 30sccm 3vol% H_2 in Ar for 1h, Feed flow rate: 30sccm C_3H_8:Ar=7:93

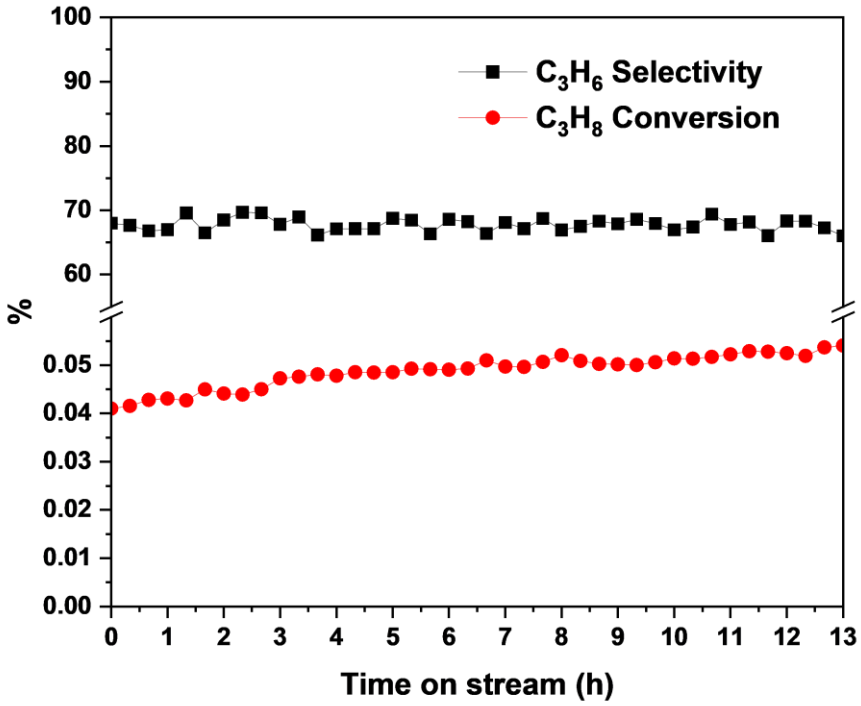

Figure B.4. Blank propane conversion and propene selectivity as a function of time on stream. Test conditions: Temperature:550°C, Pressure:1bar, Catalyst mass: blank, Feed flow rate: 30sccm C_3H_8:Ar=7:93

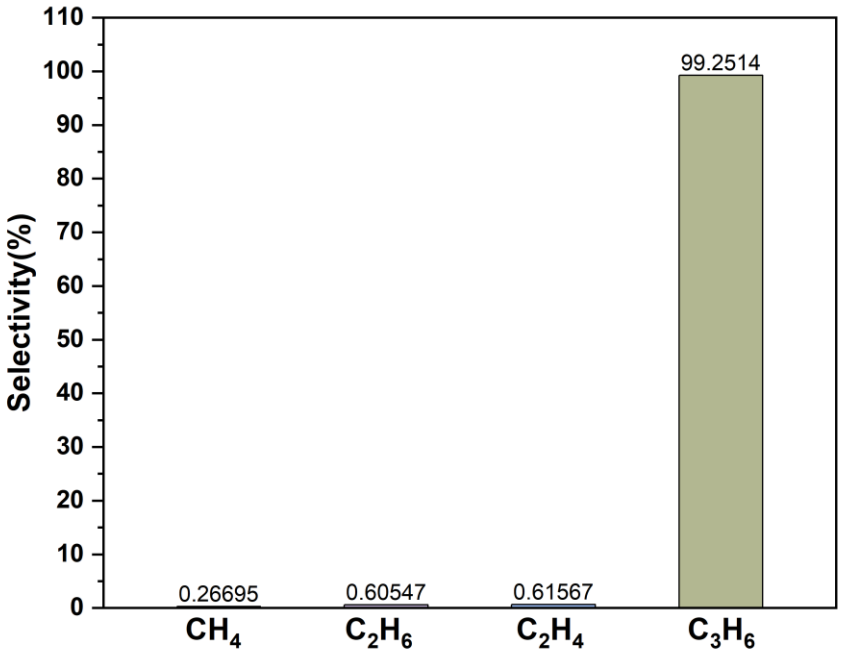

Figure B.5. Selectivity(%) to CH_4, C_2H_6, C_2H_4 and C_3H_6 over 6SCT titania samples during 12h non-oxidative propane dehydrogenation activity. Test conditions: Temperature:550°C, Pressure:1bar, Catalyst mass: 150mg 6SCT titania + 50mg Davisil 646 silica, 30sccm C_3H_8:Ar=6.9:93.

Appendix C

Response factor calculation

To determine the response factor for C_3H_8, 30sccm of 7vol% C_3H_8 in Ar is fed to the GC via bypass line(feed analysis). At least, 5 injections are given. Thereafter, FID data is obtained.

The results from the feed analysis show a trace amount of ethane in the feed. Thus, the ethane amount in the feed is subtracted and the calculation for conversion and selectivity is solely based on ethane-free feed.

FID data comprises retention time and peak area for each component for every injection. The amount of propane, $n_{C_3H_8}$ fed to the GC can be calculated as:

$$n_{C_3H_6} = \beta_{Propane} * \text{peak area} \qquad \textbf{C.1}$$

Where $\beta_{Propane}$ is the response factor for propane.

The propane feed used in this study comprises 7vol% C_3H_8 in Ar. Based on this information, the response factor for the propane can be calculated as:

$$\beta_{Propane} = \frac{7}{\text{Average FID area of propane from feed analysis}} \qquad \textbf{C.2}$$

Once the response factor for propane is calculated, the response factor for other hydrocarbons could be related according to the carbon number as:

$$\beta_{Methane} = \beta_{Propane} * 3$$

$$\beta_{Ethane} = \frac{\beta_{Methane}}{2}$$

$$\beta_{Ethene} = \frac{\beta_{Methane}}{2}$$

$$\beta\gamma_{\text{Propane}} = \beta_{\text{Propene}}$$

Propane conversion and propene selectivity calculation

Once the response factors are determined according to the discussion in the above section, the propane conversion and propene selectivity can be calculated as follows:

$$X_{C_3H_8}(\%) = \frac{\left(\sum_{i=1}^{3} \gamma_i \times n_i\right) - \left(3 \times n_{C_3H_8}\right)}{\sum_{i=1}^{3} \gamma_i \times n_i} \times 100\% \qquad \textbf{C.3}$$

$$S_{C_3H_6}(\%): \frac{3 \times n_{C_3H_6}}{\left(\sum_{i=1}^{k} \gamma_i \times n_i\right) - \left(3 \times n_{C_3H_8}\right)} \times 100\% \qquad \textbf{C.4}$$

Where, γ_i: number of carbon atoms in the hydrocarbon, i and n_i: amount/concentration of hydrocarbon, i present in the effluent to the GC.

The amount/concentration of hydrocarbon, n_i can be computed as:

$$n_i = \beta_i * \text{peak area}$$

Where, β_i is the response factor for hydrocarbon i.

Appendix D

Nitrogen Physisorption results

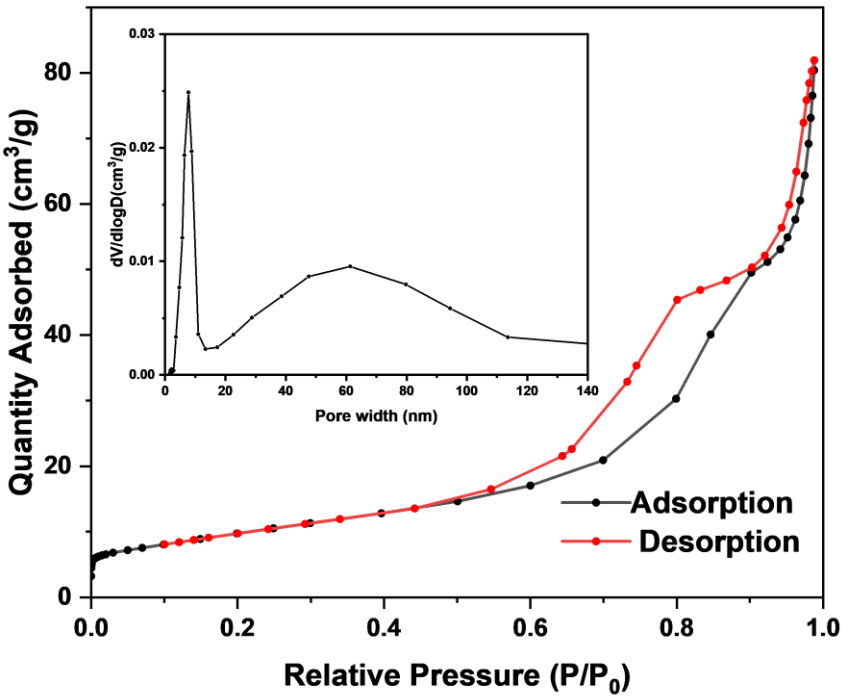

Figure D.6. N_2 adsorption-desorption isotherm and BJH plot(inset) of 8SCT sample

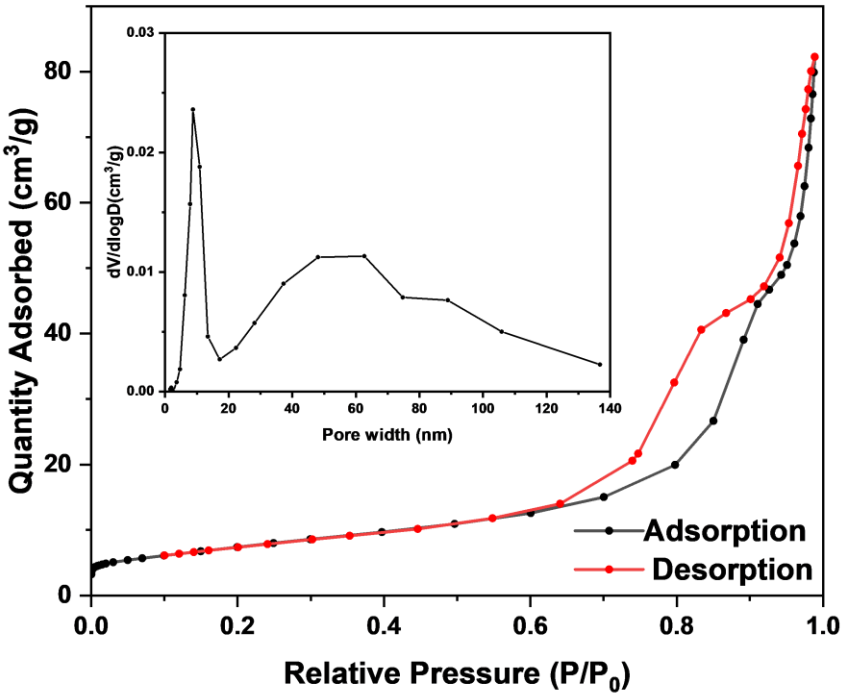

Figure D.7. N_2 adsorption-desorption isotherm and BJH plot(inset) of 10SCT sample

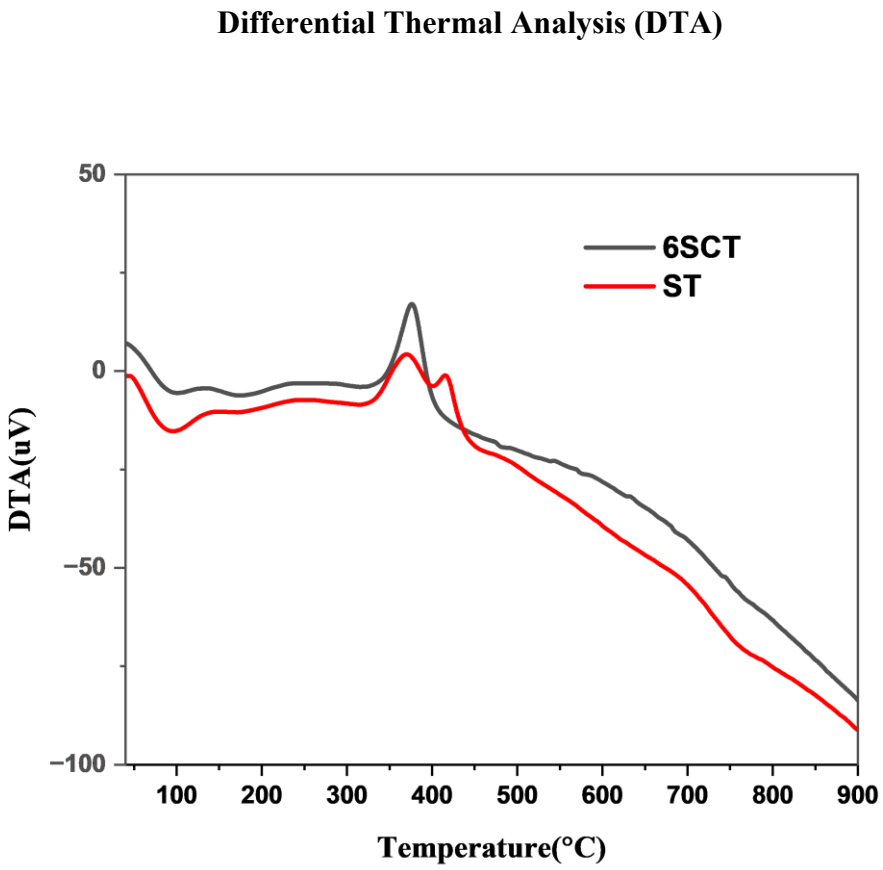

Figure D.8. Differential Thermal Analysis (DTA) plots for ST and 6SCT titania